COMMENTARIES AND REVIEWS

Fullerenes

M. S. Dresselhaus
Department of Electrical Engineering and Computer Science and Department of Physics, Massachusetts Institute of Technology, Cambridge, Massachusetts 02139

G. Dresselhaus
Francis Bitter National Magnet Laboratory, Massachusetts Institute of Technology, Cambridge, Massachusetts 02139

P. C. Eklund
Department of Physics and Astronomy and Center for Applied Energy Research, University of Kentucky, Lexington, Kentucky 40506

A review of the structure and properties of fullerenes is presented. Emphasis is given to their behavior as molecular solids. The structure and property modifications produced by alkali-metal doping are summarized, including modification to the electronic structure, lattice modes, transport, and optical properties. Particular emphasis is given to the alkali-metal-doped fullerenes because of their importance as superconductors. A review of the structure and properties of fullerene-based graphene tubules is also given, including a model for their one-dimensional electronic band structure. Potential applications for fullerene-based materials are suggested.

I. INTRODUCTION

C_{60} and related fullerenes have attracted a great deal of interest in recent years because of their unusual properties. Fullerenes are of broadly based interest to scientists in many fields: to physicists for their relatively high T_c superconductivity (33 K), the fivefold local symmetry of the icosahedral fullerenes and the quasi-1D behavior of fullerene-related nanotubules; to chemists for the large family of new compounds that can be prepared from fullerenes; to earth scientists because of the very old age of shungite, a mineral deposit that contains a high concentration of fullerenes; and to materials scientists as representing a source of monodisperse nanostructures that can be assembled in film and crystal form and whose properties can be controlled by doping and intercalation.

There are a number of theoretical suggestions for icosahedral molecules that predated their experimental identification by many decades, including the very early work of Tisza[1] who considered the point group symmetry for icosahedral molecules and Osawa[2] who suggested that an icosahedral C_{60} molecule (see Fig. 1) might be stable chemically. Early Russian workers showed by Hückel calculations that C_{60} should have a large electronic gap between the highest occupied molecular orbital (HOMO) and the lowest unoccupied molecular orbital (LUMO).[3,4] These early theoretical suggestions for icosahedral C_{60} were not widely appreciated, and

some of this literature was only rediscovered after the experimental work of Kroto and co-workers in the middle 1980's[5] established the stability of the C_{60} molecule in the gas phase. Concurrently, astrophysicists were trying to identify some unusual IR emissions of interstellar dust from carbon stars, and this work also suggested the possibility of larger carbon clusters.[6-8] Hare and Kroto have argued that carbon clusters similar to fullerenes play a role in the galactic carbon cycle.[9]

In early gas phase work, a molecule with 60 carbon atoms was established experimentally by mass spectrographic analysis,[5] and this molecule was later identified with icosahedral symmetry. The name of "fullerene" was given by Kroto and Smalley to the family of molecules observed in this gas phase work,[5] because of their resemblance to the geodesic domes designed and built by R. Buckminster Fuller.[10,11] The name "buckminsterfullerene" or simply "buckyball" was given specifically to the C_{60} molecule and the general name "fullerene" to C_n cage molecules built from a collection of hexagonal and pentagonal faces. In the early gas phase work, the molecular species were produced by the laser vaporization of carbon from a graphite target in a pulsed jet of helium.[5,12] In this gas phase work, mass spectroscopy was used as the main characterization tool for fullerenes (see Fig. 2). The first clear evidence that C_{60} exhibits icosahedral symmetry came from nuclear magnetic res-
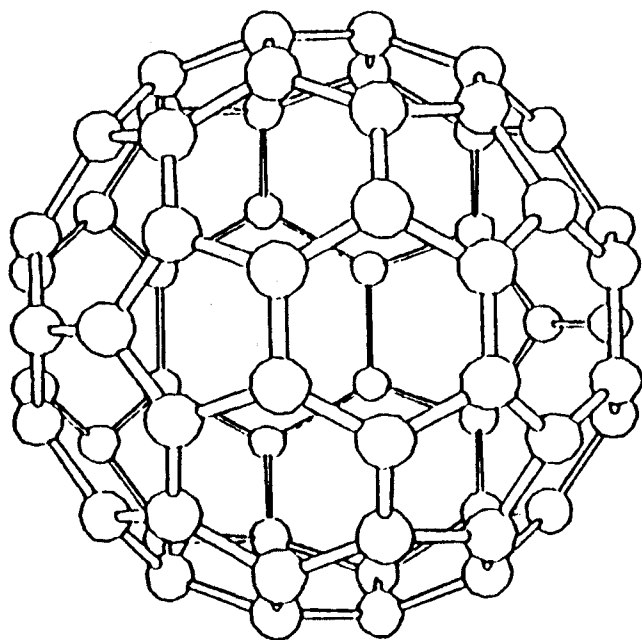
FIG. 1. In the C_{60} molecule each carbon atom is at an equivalent position on the corners of a regular truncated icosahedron.

onance experiments[13-16] where a single resonance line was observed, consistent with only one type of chemical site for carbon atoms in this molecule (see Fig. 1).

In the fall of 1990 a new type of condensed matter, based on C_{60}, was synthesized for the first time by Krätschmer and co-workers[17] who found a simple method for preparing gram quantities of C_{60} that had previously been available only in trace quantities in the gas phase.[5,18] The availability of large quantities of fullerenes provided a great stimulus to this research field.
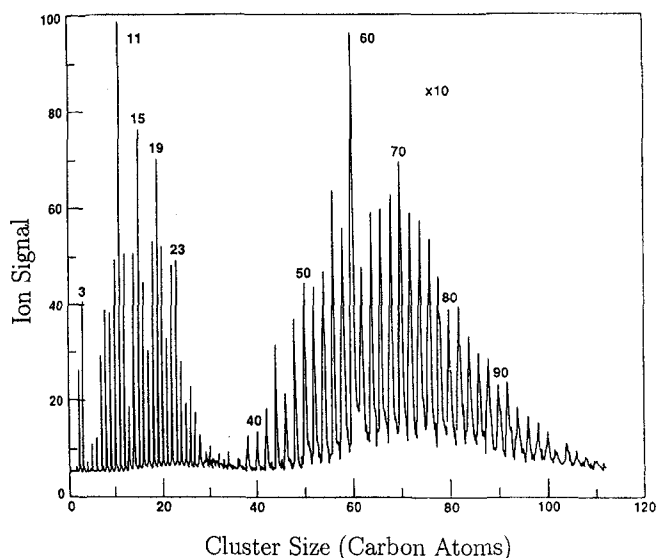

FIG. 2. Time of flight mass spectrum of carbon clusters produced in a supersonic beam by laser vaporization of graphite.[12]

It was soon found by Haddon and co-workers[19] that the intercalation of alkali metals into C_{60} to a stoichiometry M_3C_{60} (where M = K, Rb, and Cs) greatly modifies the electronic properties of the host fullerenes and yields relatively high transition temperature ($18 \leq T_c \leq 33$ K) superconductors.[20] The discovery of superconductivity[21] in these compounds further spurred research activity in C_{60}-related materials.

This review discusses the techniques of synthesis in Sec. II, the various doping techniques in Sec. III, the structure of fullerene molecules in Sec. IV, the crystalline structure of selected fullerenes in Sec. V, the spectra of vibrational modes in fullerenes in Sec. VI, the thermal properties in Sec. VII, the electronic structure in Sec. VIII, the optical properties in Sec. IX, the results of carrier transport experiments in Sec. X, nuclear magnetic resonance (NMR), scanning tunneling microscopy (STM), surface science, and electron spectroscopies in Sec. XI, the superconducting properties of doped fullerenes in Sec. XII, the magnetic properties of fullerene-related solids in Sec. XIII, while in Sec. XIV we review the structure and electronic properties of graphene tubules, and finally we discuss some possible applications of fullerenes in Sec. XV.

II. SYNTHESIS OF FULLERENE SOLIDS

Although C_{60} has been reported (at very low concentrations) in common carbon soot and in the carbon-rich mineral shungite,[22] experimental studies of fullerenes have been based on synthetic samples. Early synthesis was done using laser ablation of graphite targets in He gas to create fullerenes in the gas phase.[5] This remains a general synthesis technique that is particularly applicable to molecular beam studies of fullerenes.[5] However, most workers in the field today require large quantities of fullerenes. Krätschmer and Huffman were the first to develop an efficient method to produce large quantities of fullerenes.[17] Most workers today use a synthesis method based on an ac discharge between graphite electrodes in approximately 200 Torr of He. A later version of their arc method employed a "contact arc" (see Fig. 3), where gravity was used to maintain electrical contact of a smaller diameter vertical carbon rod against a fixed larger diameter carbon counter electrode. A low-cost, alternating-current arc welder can be used to drive the arc without the need for ballast resistors. The heat generated at the contact point between the electrodes evaporates carbon to form soot and fullerenes, which condense on the water-cooled walls of the reactor. Later designs employed a stainless steel (SS), rather than a Pyrex chamber wall, and a refractory metal, rather than a copper (Cu) sleeve, to guide the sliding motion of the upper electrode. The entire apparatus was submerged in water for cooling purposes. This apparatus is capable
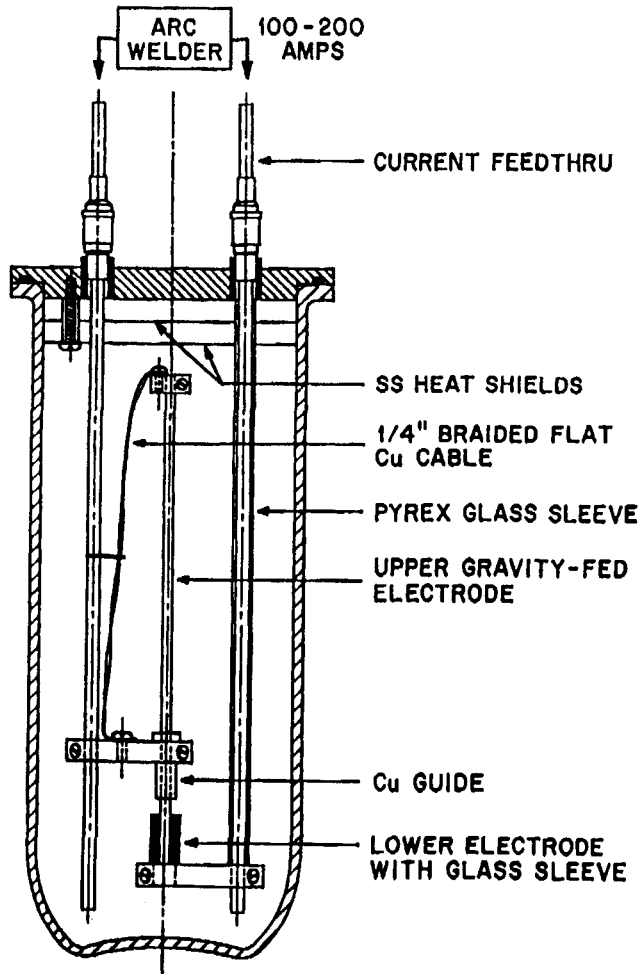
FIG. 3. Schematic view of a simple contact-arc apparatus for the production of fullerene-rich carbon soot. The apparatus is slightly altered from that given in Ref. 23.
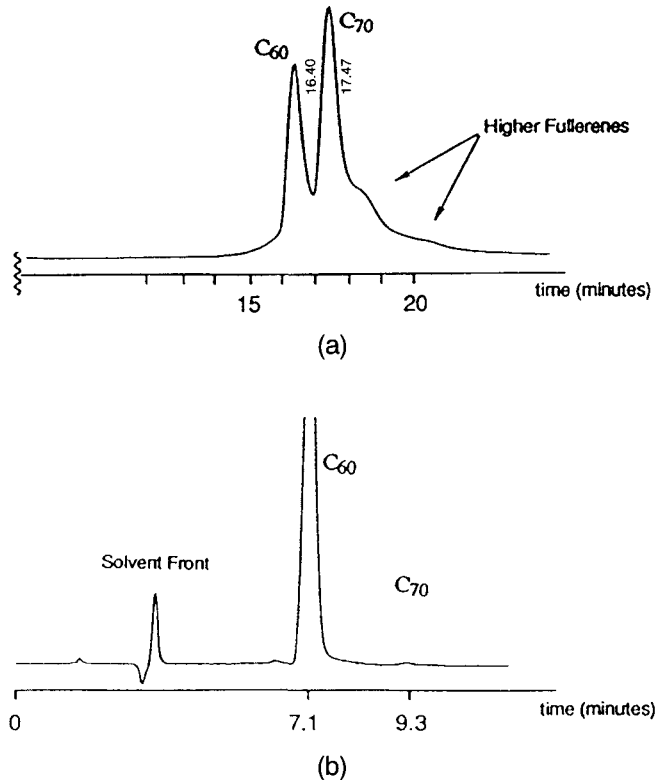

FIG. 4. (a) Gel permeation chromatogram of fullerenes obtained by a Soxhlet extraction with toluene (UV/vis detection is at 600 nm). (b) High performance liquid chromatography (HPLC) chromatogram using a Novapak C_{18}-silica column and 60% isopropanol/40% toluene as the mobile phase (UV/vis detection is at 590 nm).[25] In (a) the peak collection points for C_{60} and C_{70} are at 16.40 and 17.47 min, respectively.

of producing several grams of C_{60}/C_{70} per day. This discharge produces a carbon soot that can contain up to $\sim 15\%$ of the fullerenes C_{60} ($\sim 13\%$) and C_{70} ($\sim 2\%$). Smaller fullerenes ($n \leqslant 84$ in C_n) are separated from the soot using Soxhlet extraction with a toluene solvent. The separation of C_{60} from C_{70} and the higher molecular weight fullerenes is typically accomplished using liquid chromatography (LC)[23–25] (see Fig. 4). The identity of the separated fractions from the LC column is verified, for example, by the comparison of the observed optical spectra (see Sec. IX) and NMR data (see Sec. XI) with published results.[26] Spectroscopic characterization of the vibrational modes (see Sec. VI) allows an assessment to be made of the compositional purity of a fullerene sample. Liquid chromatography generally allows separation of the fullerenes according to their molecular weights, but this method can also separate isomers with the same molecular weight, but having different molecular shape, e.g., separating C_{78} with C_{2v} symmetry from C_{78} with D_3 symmetry.[23]

Two recent bench top LC schemes have been reported that use pure toluene as the elutant, and this apparatus can easily produce about 200–500 mg of C_{60} per day. In the first scheme, toluene is used in a closed loop system both to extract the fullerenes from the soot (Soxhlet extraction), as well as to serve as the elutant on a silica gel column. In the second scheme, fullerenes in toluene are passed through a high performance gel permeation chromatograph.[25] Recovery and purification of higher C_n fullerenes (i.e., $n > 70$) from the soot is more difficult because of the lower solubilities of these molecules. Soxhlet extractions in high boiling point solvents have been used, followed by separation in alumina columns.[27]

For experiments where rigid exclusion of solvent impurities is necessary, it is possible to separate C_{60} and C_{70} from the arc-derived soot without the use of solvents by heating the soot in vacuum and in a temperature gradient. The C_{60} and C_{70} both are sublimed from the soot that is placed in the hottest part of the furnace, and the fullerene molecules drift toward the cold end of a quartz tube connected to a vacuum line. The C_{60} and C_{70} molecules condense in separate bands

on the tube wall, and the positions of these bands are related to different sublimation temperatures for C_{60} and C_{70}. For C_{60} or C_{70} powders obtained from liquid chromatography, heat treatment in a dynamic vacuum of flowing inert gas (300 °C for 1/2 to 1 day) is used to reduce the solvent impurity. Furthermore, solid C_{60} has been shown to intercalate or accept oxygen quite easily at 1 atm, particularly in the presence of visible or UV light. Thus, degassed powders should be stored in vacuum or in an inert gas (preferably in the dark).

Actual property measurements of fullerenes are made either on powder samples, films, or single crystals. C_{60} powder is obtained from the solution that has passed through the LC column by vacuum evaporation of the solvent from the solution. Pristine C_{60} films can be deposited onto a substrate such as a clean silicon (100) surface by sublimation of the C_{60} powder in a vacuum of $\sim 10^{-6}$ Torr. Ellipsometry can be used to measure the thickness of the C_{60} films as they are deposited.[28] By variation of the substrate material and crystalline orientation, and by variation of the film growth temperature, the crystallite size and microstructure of the film can be varied. Single crystals can be grown either from solution using solvents such as CS_2, hexane and toluene, or by vacuum sublimation.[29] The solution growth method tends to yield larger single crystals, but such crystals tend to contain trapped solvent. The smaller crystals (~ 0.5 mm in size) grown by sublimation (in vacuum or in an inert gas such as argon) tend to be more pure chemically and more perfect structurally.

III. DOPING METHODS

Each carbon atom in a C_{60} molecule is identical, has four valence electrons, and bonds to each of the three nearest-neighbor carbon atoms. Two of the bonds are located at the fusion of a hexagon and a pentagon and are single bonds. The third bond is located at the fusion between two hexagons and is a double bond (see Fig. 1). Since all the bonding requirements of the carbon atoms are satisfied, it is expected that C_{60} is an insulator (semiconductor) with a band gap between the occupied and unoccupied states, consistent with the observed electronic structure (see Sec. VIII). To make C_{60} (and also other fullerenes) conducting, doping is necessary.

Since doping can greatly modify the properties of fullerenes in scientifically interesting and practically important ways, there is a large literature on the synthesis, structure, and properties of doped fullerenes. While doped C_{60} has been investigated in some depth, many gaps in our knowledge remain, and very little is known about the doping of higher mass fullerenes. For these reasons, the study of the synthesis, structure,

and properties of doped fullerenes is likely to remain an active field of study for some time.

In our discussion below we review several ways to introduce foreign atoms into a C_{60}-based solid.[30] This is followed by a very brief review of the doping of other fullerene-derived materials.

A. Endohedral doping

One doping method is the addition of a rare earth, an alkaline earth, or an alkali metal ion[30] into the interior of the C_{60} ball to form an endohedrally doped molecular unit. This configuration has, for example, been denoted by La @ C_{60} for one endohedral lanthanum in C_{60}, or Y_2 @ C_{82} for two Y atoms inside a C_{82} fullerene.[31] For the larger fullerenes, the addition of up to three metal ions endohedrally has been demonstrated by mass spectroscopy techniques, which measure the mass associated with the fullerene and its endohedrally doped species.[30] There seems to be no physical law preventing the introduction of even larger numbers of endohedral species in a large fullerene. It has been shown by ESR spectra (see Sec. XI.B) that when La is inside the fullerene ball it has a valence of $+3$,[30] indicating the presence of three delocalized electrons on the C_{60} ball in antibonding states which could be available for conduction in a solid of endohedrally doped C_{60}. Isoelectronic Y^{3+} and Sc^{3+} have also been introduced as endohedral dopants in C_{60}.

Thus far, only very small quantities of endohedrally doped fullerenes have been prepared, and their study has been limited to investigations of isolated endohedrally doped fullerenes. No studies of crystalline material composed of endohedrally doped constituents have yet been reported. The synthesis of new endohedrally doped molecules, the study of the structure and properties of these doped molecules, and the materials synthesized from endohedrally doped molecules are expected to be active research fields for at least the near future.

B. Substitutional doping

A second doping method is the substitution of an impurity atom with a different valence state for a carbon atom on the surface of a C_{60} ball. Since a carbon atom is so small, and since the average nearest neighbor C–C distance denoted by a_{C-C} on the C_{60} surface is only 1.44 Å,[5,32–35] the only species that can be expected to substitute for a carbon atom on the C_{60} ball surface is boron, making the charged ball p-type. Smalley and coworkers have demonstrated that it is possible to replace more than one carbon atom by boron on a given ball.[30] Also for graphite, the only substitutional dopant is boron, and for the same reasons as for C_{60}. However, for diamond, which has a C–C nearest neighbor distance

of $a_{C-C} = 1.544$ Å, both boron and nitrogen can enter the diamond lattice substitutionally.[36]

C. Radial exohedral doping

In a totally different approach, dopants to fullerenes have been added via radial bonds to the outside of C_{60} balls. Two examples of such radial exohedral doping have been observed for fluorine and hydrogen doping. In the case of radial exohedral fluorine doping, the attachment of a F atom converts a double bond in C_{60} into a single bond.[37] A report[38] has been given of adding up to 60 fluorine atoms per ball, to form $C_{60}F_{60}$. However, most authors report lower fluorine doping levels. Similar bonding arrangements of C_{60} to hydrogen have also been reported up to a maximum hydrogen concentration, $C_{60}H_{60}$.[39] However, it is not known whether in the case of $C_{60}H_{60}$ all the H-bonds are directed radially outward, or whether some may perhaps be directed radially inward and be endohedrally bonded.[31] A variety of bromine-doped fullerenes have also been prepared,[40] though the doping arrangement in the case of bromine may well be different from that for fluorine and hydrogen.

D. Exohedral donor doping

The most common method of doping fullerene solids is exohedral donor doping (also called intercalation). In this case, the dopant (e.g., an alkali metal or an alkaline earth, M) is introduced into the interstitial positions between adjacent balls (exohedral locations). Charge transfer can take place between the M atoms and the balls, so that the M atoms become positively charged ions and the balls become negatively charged with predominately delocalized electrons. This method of doping forms exohedral fullerene solids and closely parallels the process of intercalating alkali metal ions into layers that are sandwiched between carbon layers in graphite.[41] It has also been reported that it is possible to place a potassium atom endohedrally inside the C_{60} ball while at the same time substituting a boron for a carbon atom on the surface of the ball.[30]

Among the alkali metals, Li, Na, K, Rb, and Cs[42] have all been used as exohedral dopants for C_{60}, as well as intermetallic mixtures of these alkali metals such as Na_2K[43,44] and Rb_xCs_y.[45] The doping of the C_{60} with alkali metals can be achieved in a two-temperature oven, similar to the apparatus used to prepare alkali-metal graphite intercalation compounds.[46] This approach works well with powdered samples, and the stoichiometry is controlled by the number of moles of alkali-metal introduced into the sealed ampoule (quartz or Pyrex) relative to the number of moles of C_{60}, the temperatures of the reagents, and the duration of the reactions. Alkali metal doping of thin (~ 1000 Å) C_{60} films can be carried out similarly, using a sealed quartz or Pyrex tube (with approximate dimensions 25 cm long $\times$ 1 cm diameter) that contains the C_{60} film/substrate sample and the alkali metal at opposite ends. The films are maintained at a higher temperature (200 °C) than the alkali metal (M) (80–150 °C) to avoid condensation of the alkali metal on the film surface. The in situ progress of the reactions can be monitored qualitatively by the color change observed in the films and more quantitatively by the doping-induced downshift of the strongest C_{60} Raman line (the A_g mode at 1469 cm^{-1}, see Sec. VI. B) or by changes in the electrical conductivity (see Sec. X). The doping reaction in C_{60} single crystals is carried out in a two-zone furnace for longer times (~ 1 to 2 weeks), because of the larger distances that the dopant must travel.[47-49] The structure of the alkali-metal-doped fullerenes is reviewed in Sec. V. C.

Successful exohedral doping has also been achieved with the intercalation of alkaline earth dopants, such as Ca and Ba.[50,51] In the case of the alkaline earth dopants, two electrons per metal atom M are transferred to the C_{60} balls for low concentrations of metal atoms, while for high concentrations of metal atoms the charge transfer is less than two electrons per alkaline earth ion. In general, the alkaline earth ions are smaller than the corresponding alkali metals in the same row of the periodic table. The crystal structures formed with alkaline earth doping are often different from those for the alkali metal dopants (see Sec. V. C). Doping fullerenes with acceptors has been more difficult than with donors because of the high electron affinity of C_{60} (see Table I). A stable crystal structure has nevertheless been identified upon doping C_{60} with iodine, where the iodine is reported to form a sheet between layers of C_{60} balls; no measurable conductivity has, however, been observed in the case of iodine doping of fullerenes.[68,69]

E. Fullerene chemistry

Fullerene chemistry has become a very active research field, largely because of the uniqueness of the C_{60} molecule and the variety of chemical reactions that appear to be possible. Since many of the fullerene reactions appear to be reversible and the amount of the fullerene material available to most chemists is small, research in this field is one of the most challenging areas at the cutting edge of chemistry. Some of the simplest of the fullerene compounds, such as $C_{60}H_x$, $C_{60}F_x$, and $C_{60}Br_x$, have already been mentioned. More complex compounds have also been synthesized, and many of these are based on forming bonds to the two carbon atoms joining two hexagons on the C_{60} ball (see Fig. 1). The reason why these sites are more reactive is related to the fact that these sites are connected by a double bond in the C_{60} molecule, giving rise to a higher electron

2058

J. Mater. Res., Vol. 8, No. 8, Aug 1993

TABLE I. Physical constants for C_{60} materials.

Quantity	Value	Reference
Average C–C	1.44 Å	32
FCC lattice constant	14.17 Å	50
C_{60} mean ball diameter	6.83 Å	50
C_{60} ball outer diameter[a]	10.18 Å	50
Tetrahedral site radius	1.12 Å	52
Octahedral site radius	2.07 Å	52
Mass density	1.72 g/cm^3	52
Molecular density	1.44×10^{21}/cm^3	52
Compressibility $(-d \ln V/dP)$	6.9×10^{-12} cm^2/dyn	33
Bulk modulus	14 GPa	53
Structural phase transitions	255 K, 165 K	54
Binding energy per atom	7.40 eV	55
Electron affinity (pristine C_{60})	2.65 eV	56
Ionization potential (1st)	7.58 eV	57
Ionization potential (2nd)	11.5 eV	58
Vol. coeff. of thermal expansion	6.2×10^{-5}/K	59
Band gap (HOMO–LUMO)	1.7 eV	60
Spin-orbit splitting of C($2p$)	0.00022 eV	61
Velocity of sound v_t	2.1×10^5 cm/s	62
Velocity of sound v_l	3.6×10^5 cm/s	62
Debye temperature	185 K	63–65
Thermal conductivity (300 K)	0.4 W/mK	66
Phonon mean free path	50 Å	66
Static dielectric constant	4.0–4.5	28, 67

[a]The outer diameter of the C_{60} molecule is estimated from 6.83 + 3.35 Å. The diameter 6.83 Å is obtained geometrically from the C–C bond distance.

density than is present elsewhere on the surface of the molecule. As various moieties bond to these two carbons, the carbon atoms are pulled out of their equilibrium positions, the local structure of the fullerene is modified, and the high degree of symmetry is reduced, thereby activating many new Raman and infrared vibrational modes (see Sec. VI).

One of the simplest compounds that distorts carbon bonds on the C_{60} molecule is the epoxide $C_{60}O^{70}$ which crystallizes in the same structure as pristine C_{60} and with a similar lattice constant[59] (see Sec. V. D). The oxygen atoms in this case bond to one of the electron-rich double bonds of the C_{60} ball, bridging two carbon atoms.[59]

The joining of fullerenes by the addition of various moieties through a carbon bridge atom has formed the basis of a large number of fullerene-derived compounds.[71] In other cases the bonding is done through a metal atom, such as Pt, to which other organic groups are attached.[72] For example, to a metal atom, such as Pt, might be attached phosphorus and three phenyl groups or three alkyl groups or a variety of other species.[72] Other examples of metal atom attachments followed by organic "arms" are Os[73,74] and Ir.[75] In preparing many of these compounds, specific functional groups are added for special chemical reasons, while other chemical species are used to achieve a chemically stable compound.

One especially interesting direction that this synthesis work has taken is the preparation of an organic ferromagnet based on the reaction of the organic donor TDAE [tetrakis(dimethylamino)ethylene] complex to C_{60}.[76] The magnetic properties of this compound are briefly reviewed in Sec. XIII.

IV. STRUCTURE OF FULLERENES

Many independent experiments reported in this review show that the crystalline materials formed from the fullerenes are molecular solids. Therefore, the structure and properties of these solids are strongly dependent on the structure and properties of the constituent fullerene molecules. In this section we address the structure of the molecules, while in Sec. V the structure of the molecular solid is reviewed.

A. Structure of C_{60}

The 60 carbon atoms in C_{60} are now known to be located at the vertices of a regular truncated icosahedron where every site is equivalent to every other site (see Fig. 1), consistent with a single sharp line in the NMR spectrum[13,14] (see Sec. XI. A). Since (1) the average nearest neighbor carbon-carbon (C–C) distance a_{C-C} in C_{60} (1.44 Å) is almost identical to that in graphite (1.42 Å), (2) each carbon atom in graphite and in C_{60} is trigonally bonded to three other carbon atoms, and (3) most of the faces on the regular truncated icosahedron are hexagons, we can to a first approximation think of the C_{60} molecule as a "rolled-up" graphene sheet (a single layer of crystalline graphite). The regular truncated icosahedron has 20 hexagonal faces and 12 additional pentagonal faces to form a closed shell, in keeping with Euler's theorem discussed below.

The symmetry operations of the icosahedron consist of the identity operation, 12 fivefold axes through the centers of the pentagonal faces, 20 threefold axes through the centers of the hexagonal faces, and 15 twofold axes through centers of the edges joining two hexagons. Each of the 60 rotational symmetry operations can be compounded with the inversion operation, resulting in 120 symmetry operations in the icosahedral point group I_h[77] (see Fig. 1). Molecules with I_h symmetry of which C_{60} is the most prominent molecule have the highest degree of symmetry of any known molecule. The diameter of the C_{60} molecule is 6.83 Å, treating the carbon atoms as points.[5,52] When taking account of the size of the π-electron cloud associated with the carbon atoms, the outer diameter of the C_{60} molecule becomes 10.18 Å (see Table I).

All of the closed cage structures in fullerenes with only hexagonal and pentagonal faces contain 12 pentagonal faces and h hexagonal faces, and follow Euler's

theorem for polyhedra:

$$f + v = e + 2 \qquad (1)$$

where f, v, and e are, respectively, the number of faces, vertices, and edges, of the polyhedra. If we consider polyhedra formed by h hexagonal faces and p pentagonal faces, then

$$f = p + h$$
$$2e = 5p + 6h$$
$$3v = 5p + 6h \qquad (2)$$

so that

$$6(f + v - e) = p = 12 \qquad (3)$$

from which we conclude that all fullerenes with only hexagonal and pentagonal faces must have 12 pentagonal faces, and the number of hexagonal faces is arbitrary. These arguments further show that the smallest possible fullerene is C_{20} which would form a regular dodecahedron with 12 pentagonal faces. It is, however, considered energetically unfavorable for two pentagons to be adjacent to each other (referred to as the isolated pentagon rule) since this would lead to higher local curvature on the fullerene ball, and hence more strain. For this reason fullerenes with much fewer than 60 carbon atoms are not very stable (see Fig. 2). Furthermore, since the addition of a single hexagon adds two carbon atoms, all fullerenes must have an even number of carbon atoms, in agreement with the observed mass spectra for fullerenes, as illustrated in Fig. 2.[12]

Although each carbon atom in C_{60} is equivalent to every other carbon atom, the three bonds emanating from each atom are not equivalent, two being electron-poor single bonds, and one being an electron-rich double bond. Consistent with the x-ray diffraction evidence, the structure of C_{60} is further stabilized by introducing a small distortion of the bond lengths to form the Kekulé structure of alternating single and double bonds around the hexagonal face. We note that the icosahedral I_h symmetry is preserved under these distortions. The single bonds that define the pentagonal faces are increased from the average bond length of 1.44 Å to 1.46 Å, while the double bonds are decreased to 1.40 Å.[5,32,33,52,78] Since each carbon atom has its valence requirements fully satisfied, the C_{60} molecules are expected to form a van der Waals bonded molecular solid which is an insulator (or a semiconductor). The semiconducting behavior is further stabilized by the above-mentioned distortions in the intramolecular bond lengths.

B. Structure of C_{70} and higher fullerenes

In the synthesis of C_{60}, larger molecular weight fullerenes C_n ($n > 60$) are also formed. By far the most abundant higher molecular weight fullerene produced in the arc discharge method is C_{70} [Fig. 5(a)]. However, significant quantities of C_{76}, C_{78}, and C_{84} have also been isolated and studied in some detail.[26,79] Bands of carbon clusters as large as C_{240}, C_{330}, and clusters in the range C_{600}–C_{700} have been observed in mass spectra,[31,80–83] but these larger clusters have not yet been proven to be fullerenes, nor have they been isolated or studied in detail.

C_{70} has been found to exhibit a rugby ball shape,[26] and its form can be envisioned either by adding a ring of 10 carbon atoms or a belt of five hexagons around the equatorial plane of the C_{60} molecule normal to one of the fivefold axes [see Fig. 5(a)]. In contrast to the C_{60} molecule with I_h symmetry, the C_{70} molecule has the lower symmetry D_{5h} and lacks inversion symmetry. Fullerenes often form isomers, since a given number n of carbon atoms C_n can correspond to molecules with different geometrical structures.[26,84] For example, C_{80} might be formed in the shape of an elongated rugby ball prepared by adding two rows of five hexagons normal to a fivefold axis of C_{60} at the equator [see Fig. 5(b)]; an icosahedral form of C_{80} can also be specified as shown in Fig. 5(c).

It is, in fact, easy to specify all possible icosahedral fullerenes using the projection method described in Sec. IV. C, where it is shown that an icosahedron consists of 20 equilateral triangles, each specified by a pair of integers (n, m) such that N in C_N is given by

$$N = 20(n^2 + nm + m^2). \qquad (4)$$

As another example of fullerene isomers, C_{78} has been shown to have five distinct isomers, one with D_3 symmetry, two with C_{2v} symmetry, and two with D_{3h} symmetry.[85] In addition, isomers giving rise to right- and left-handed optical activity are expected to occur in molecules belonging to group I (rather than I_h) and not having inversion symmetry.

C. The projection method for specifying fullerenes

A useful construction for specifying the geometry of fullerene molecules is the planar projection[86] shown in Fig. 6, where the structure of the fullerene is shown in relation to the honeycomb lattice of a single graphene sheet. In this projection the 12 pentagons needed to provide the curvature for the formation of closed polyhedral structures are treated as defects in the 2D planar honeycomb lattice, and the 12 pentagonal locations are indicated by the numbers $1, \ldots, 12$. By superimposing the numbered hexagons in Fig. 6 (which become pentagonal defects in the fullerene) with the same numbers,
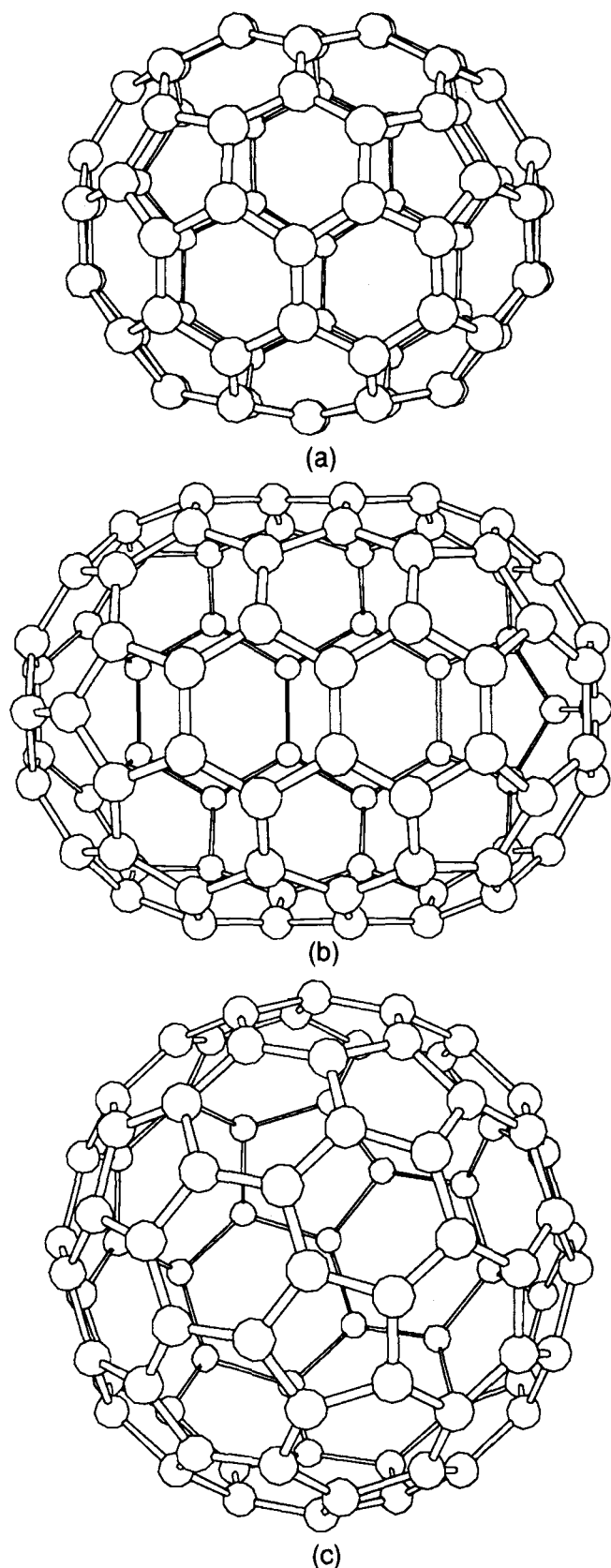
(a)

(b)

(c)

FIG. 5. (a) The C_{70} molecule as a rugby ball. (b) The C_{80} molecule as an extended rugby ball. (c) The C_{80} molecule as an icosahedron.
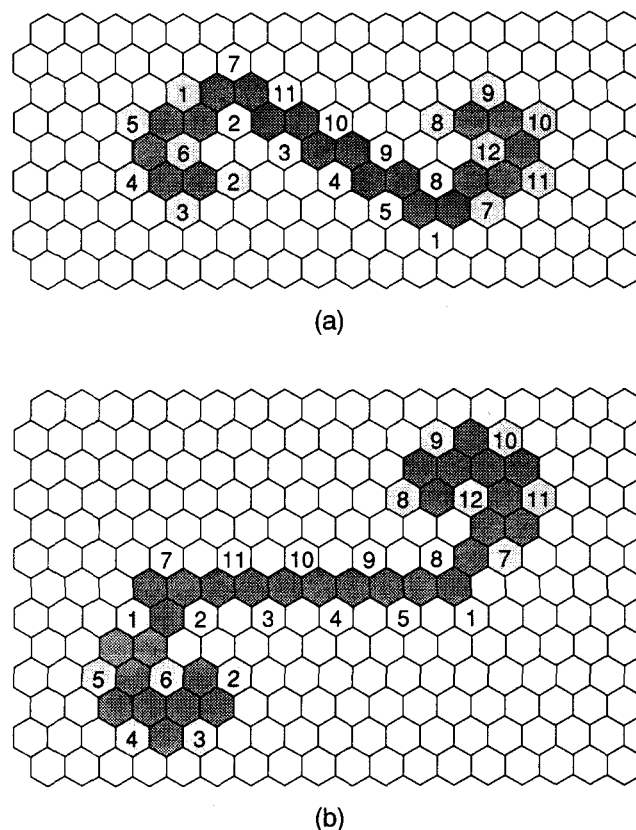

(a)

(b)

FIG. 6. The projection of two icosahedral fullerenes on a 2D honeycomb hexagonal lattice (a) for the C_{60} molecule and (b) the C_{80} molecule.

closed cage fullerenes are easily constructed. For illustrative purposes, the projections for the icosahedral C_{60} and C_{80} molecules are shown in Fig. 6.[86] If the lattice vector between two nearest neighbor pentagonal defects is $n\mathbf{a}_1 + m\mathbf{a}_2$, where $\mathbf{a}_1 = (a_0/2)(\sqrt{3}\,\hat{i} + \hat{j})$ and $\mathbf{a}_2 = (a_0/2)(\sqrt{3}\,\hat{i} - \hat{j})$ are basis vectors of the honeycomb lattice, a_0 is the lattice constant of the 2D lattice ($a_0 = 2.46$ Å, and (n, m) are both integers, then a regular truncated icosahedron contains exactly 20 equilateral triangles, each having an area proportional to $(n^2 + nm + m^2)$. This result can be used to specify all possible icosahedral fullerenes (see Sec. IV. B). Although shown here only for icosahedral fullerenes, the projection method can be used equally well to construct polyhedra that do not have an icosahedral shape. The projection method is also valuable for specifying the structure of the end caps of graphene tubules (see Sec. XIV).

V. CRYSTALLINE STRUCTURE

In this section we discuss the crystalline structure of C_{60} and the various phases that have been identified as a function of temperature. Though less is known about the crystalline structure of C_{70}, a picture of the temperature dependence of the various phases has already

emerged.[87,88] Little is known about the crystal structure of higher fullerenes. With regard to the doped fullerenes, the most complete information is available for alkali metal intercalated C_{60}. Some structural information on other doped fullerene solids (e.g., alkaline earth-doped fullerene solids) is also presently available. Knowledge of the structure is, of course, necessary to gain a microscopic understanding of the physical properties that are observed.

A. Crystalline C_{60}

In the solid state, the C_{60} molecules crystallize into a cubic structure with a lattice constant of 14.17 Å, a nearest neighbor $C_{60}-C_{60}$ distance of 10.02 Å,[52] and a density of 1.72 g/cm³ (corresponding to 1.44×10^{21} C_{60} balls/cm³). At room temperature, the balls are rotating rapidly with three degrees of rotational freedom, and the ball centers are arranged on a face-centered cubic (fcc) lattice with one C_{60} ball per primitive fcc unit cell, or four balls per simple cubic unit cell [see

Fig. 7(a)]. The pertinent space group is O_h^5 or $Fm\overline{3}m$. This structure is established directly by x-ray and neutron diffraction.[59,90,91] Relative to the other allotropic forms of carbon, solid C_{60} is relatively compressible, with an isothermal volume compressibility (see Table I) of 6.9×10^{-12} cm²/dyn,[33] approximately three times larger than graphite because the van der Waals charge cloud around the C_{60} balls can be compressed easily in three dimensions, rather than in one dimension as is the case of graphite.

Below about 255 K, the C_{60} balls completely lose two of their three degrees of rotational freedom. The residual rotational motion occurs only along the four $\langle 111 \rangle$ axes and is a hindered rotation.[35,59,91] The structure of solid C_{60} below ~255 K thus becomes simple cubic (space group T_h^6 or $Pa\overline{3}$) with a lattice constant, $a_0 = 14.17$ Å, and four C_{60} molecules per unit cell, as the four balls within the fcc structure become inequivalent as discussed below [see Fig. 7(a)].[59,91] From a physical standpoint, the lowering of the symmetry is caused by the assignment of a specific $\langle 111 \rangle$ direction (vector) to
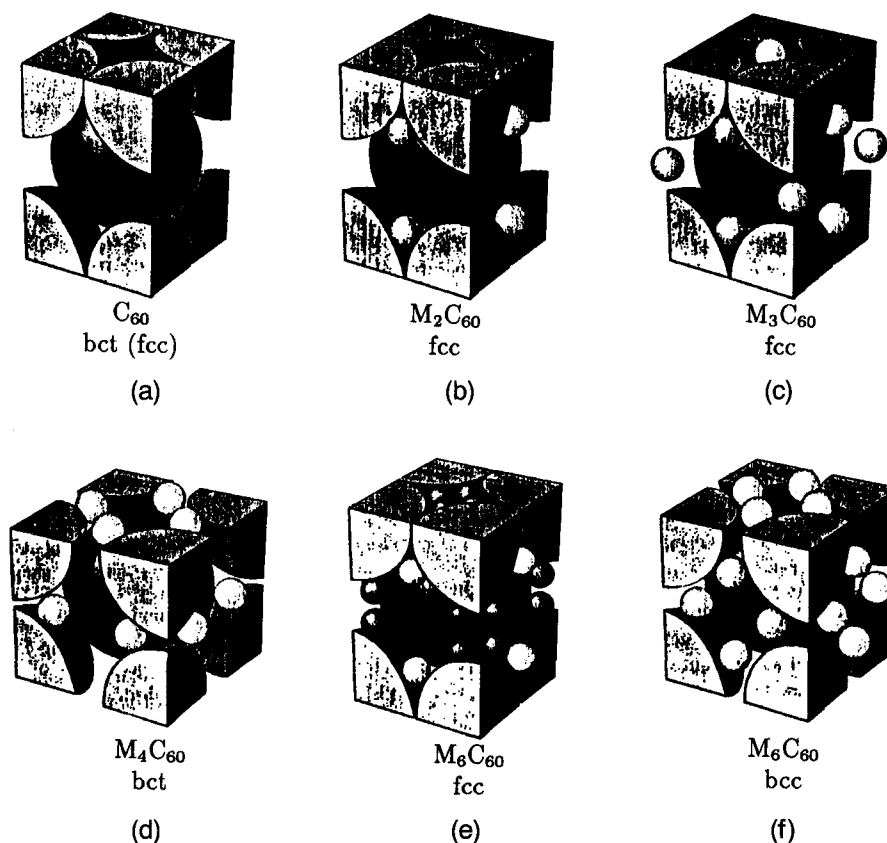

FIG. 7. Structures for the solid (a) C_{60}, (b) M_2C_{60}, (c) M_3C_{60}, (d) M_4C_{60}, and two structures for M_6C_{60}: (e) M_6C_{60} (fcc) which is appropriate for M = Na and (f) M_6C_{60} (bcc) for (M = K, Rb, and Cs), using the notation of Ref. 89. The large balls denote C_{60} molecules and the small balls are alkali metal ions. For fcc M_3C_{60}, which has four C_{60} balls per cubic unit cell, the M atoms can either be on octahedral or tetrahedral sites. Undoped solid C_{60} also exhibits this crystal structure, but in this case all tetrahedral and octahedral sites are unoccupied. For (f) bcc M_6C_{60} all the M atoms are on distorted tetrahedral sites. For (d) bct M_4C_{60}, the dopant is also found on distorted tetrahedral sites. For (b) pertaining to small alkali metal ions such as Na, only the tetrahedral sites are occupied. For (e) we see four Na ions occupying an octahedral site of this fcc lattice. For (a) the actual crystal structure is fcc but a bct cell is selected to show nearest neighbor molecules.

each of the four balls. Supporting evidence for the 255 K phase transition is provided by almost all property measurements, such as differential scanning calorimetry,[92] specific heat,[63,93,94] resistivity,[83] NMR,[15,16,78,92,95,96] ultrasonic attenuation,[62] Raman spectroscopy,[97] thermal conductivity,[66] and the thermal coefficient of the lattice expansion.[59] As the temperature is lowered below 255 K, further ordering of the C_{60} balls occurs as the rotations become hindered, whereby adjacent C_{60} molecules develop correlated orientations. The crystal structure of the ordered phase can be understood by referring to Fig. 8(a) where the standard orientation of a C_{60} molecule is shown with respect to a cubic coordinate system.[98] Here the [100] axes pass through three mutually orthogonal twofold molecular axes (the centers of the electron-rich hexagon-hexagon edges), and four $\langle 111 \rangle$ axes pass through the centers of the hexagonal faces. The alternate standard orientation is shown in Fig. 8(b) which is obtained from Fig. 8(a) through rotation by $\pi/2$ about the [100] axes. In the low temperature ordered phase, the centers of four C_{60} molecules are located at coordinate locations $(0,0,0)$, $(1/2,0,1/2)$, $(1/2,1/2,0)$, and $(0,1/2,1/2)$, and each molecule, respectively, is rotated by 22° from the standard orientation shown in Fig. 8(a) about the threefold $\langle 1,1,1 \rangle$, $\langle \overline{1},\overline{1},1 \rangle$, $\langle \overline{1},1,\overline{1} \rangle$, and $\langle 1,\overline{1},\overline{1} \rangle$ axes.[59] In the idealized ordered structure, the relative orientation of adjacent balls is stabilized by aligning an electron-rich double bond on one ball opposite the electron-poor pentagonal face of an adjacent C_{60} ball [see Fig. 9(a)].

Another structure with only slightly higher energy places the electron-rich double bond of one C_{60} molecule opposite an electron-poor hexagonal face [see Fig. 9(b)]. This orientation can be achieved from the

FIG. 9. Electron-rich double bond on one C_{60} molecule (shaded) opposite an electron-poor (a) pentagonal face and (b) hexagonal face on the adjacent molecule (not shaded).

lower energy orientation described above by rotation of the C_{60} ball by 60° around a $\langle 111 \rangle$ axis.[35] As the temperature T is lowered below 255 K, the probability of occupying the lower energy configuration increases.[35] Evidence for residual structural disorder in the low temperature molecular alignment is found from neutron scattering experiments,[35] heat,[63,93,94,99] NMR motional narrowing studies,[15,16,78,92,95,96] and thermal conductivity measurements.[66] The mechanism by which some degree of orientational alignment is achieved is by the ratcheting motion of the C_{60} molecules around the $\langle 111 \rangle$ axes as they execute a hindered rotation motion. The ratcheting motion begins below the 255 K phase transition and continues down to low temperatures.

Evidence for a second phase transition at 165 K is provided by ultrasonic attenuation studies,[62] specific heat measurements,[99] dielectric relaxation studies,[100] electron microscopy observations,[101] neutron scattering measurements,[35] dynamic NMR processes,[102] and Raman scattering studies.[97] In contrast to the structural phase transition near 255 K which is sensitively studied by static diffraction techniques, the phase transition occurring near 165 K is most sensitive to dynamic processes. Despite these property measurements, no clear picture has yet emerged regarding the structural changes associated with this phase transition. This is largely due to insensitivity of the x-ray and neutron scattering experiments thus far to structural changes that might accompany this phase transition. One suggestion for a low-temperature phase that has been made calls for a superlattice structure with a structural unit cell of $2a_0$[101] (rather than the a_0) for the simple cubic structure that sets in below $\sim$255 K.

The ratcheting motion described above allows a greater fraction of the C_{60} molecules to align so that the electron-rich double bonds are opposite the electron-poor pentagons as the temperature is decreased. By $T = 90$ K, $\sim$83% of the intermolecular alignments are reported to be in the lower energy state, leaving $\sim$17% in the higher energy state where the double bond of one molecule is opposite a hexagonal face on the adjacent molecule.[35] Below 90 K, the ratcheting motion continues, but in this temperature regime the same fraction ($\sim$83% and $\sim$17%) of the relative intermolecular orientations shown in Fig. 9 is maintained, and
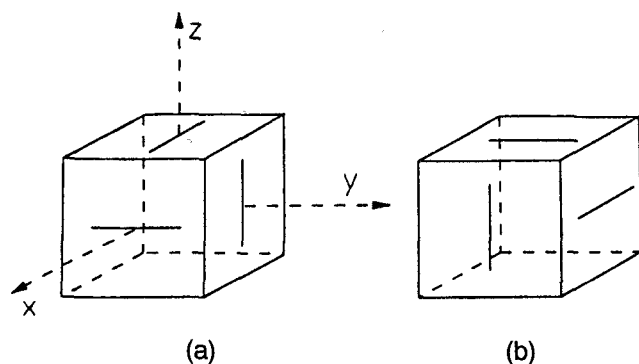

FIG. 8. (a) One "standard" orientation for the Cartesian axes in a cubic crystal so that these axes pass through three orthogonal twofold axes. (b) The other "standard" orientation, related to that in (a) by a 90° rotation about any of the Cartesian axes. An inscribed icosahedron (not shown) has mirror planes perpendicular to the three $\langle 100 \rangle$ directions. In this orientation, six of the icosahedral 2-fold axes lie in planes parallel to the mirror planes, so that when the icosahedron is circumscribed by a minimal cube, these edges lie in the cube faces, as shown.[98]
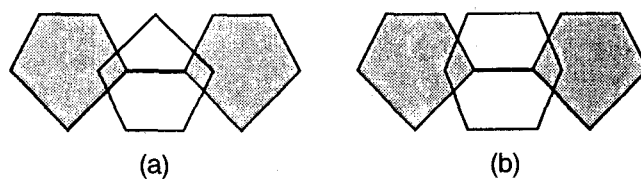
the ratcheting motion is from one orientation to an equivalent orientation. The random occurrence of the higher energy alignment state gives rise to a disordered two-state tunneling system that has been studied by both specific heat and thermal conductivity[66] measurements.

B. Crystalline C_{70} and higher fullerenes

The crystal structure of C_{70} is more complex than that of C_{60},[87,88,101] evolving through five distinct crystal structures as a function of temperature (see Fig. 10). At high temperature ($T \gg 340$ K), the fcc phase ($a = 15.01$ Å) with freely rotating molecules is most stable, but since the ideal hexagonal close packed (HCP) phase with $c/a = 1.63$ is almost equally stable, fcc crystals of C_{70} tend to be severely twinned and show many stacking faults. As the temperature is lowered, the fcc structure is continuously transformed by deformation into a rhombohedral structure with the long diagonal threefold axis aligned parallel to the $\langle 111 \rangle$ direction of the fcc structure (see Fig. 10).[88] At lower temperatures a hexagonal HCP-2 phase (space group $P6_3/mmc$) with lattice constants $a = b = 10.56$ Å and $c = 17.18$ Å and a nearly ideal c/a ratio of 1.63 is most stable. A transition to another HCP-1 phase occurs at ~337 K, but with $a = b = 10.11$ Å and a larger c/a ratio of 1.82. This larger c/a ratio is associated with the orientation of the C_{70} molecules along their long axis, as the free molecular rotation (full rotational symmetry) that is prevalent in the higher temperature HCP-2 phase freezes into a rotation about the fivefold axis of the C_{70} molecule is the HCP-1 phase (see Fig. 10).[88] The HCP-1 phase is the stable phase at room temperature (300 K). As the temperature is further lowered to ~270 K, the free

rotation about the c-axis also becomes frozen, resulting in a monoclinic structure with the unique axis along the c-axis of the HCP structure, and the monoclinic angle β close to 120°. The stacking arrangement of the C_{70} molecules in the monoclinic phase is shown in Fig. 11 where it is noted that one of the hexagonal a-axes of the HCP phase is doubled. The former hexagonal plane now consists of alternating rows of fixed C_{70} molecules that are oriented with their main symmetry axes along the unique axis of the monoclinic structure and the cross sections are arranged within rows as shown in Fig. 11, so that the high electron density hexagon-hexagon edges are opposite low electron density hexagonal face centers. The stacking perpendicular to this plane can be arranged in either of two ways: one where the A and B rows of the C_{70} molecules are directly over one another, and the other where the C_{70} molecules in the next layer are shifted to locations $b_m/2 + c_m/2$, in which the monoclinic c_m axis is related to the hexagonal a_h axis by $c_m = 2a_h$, as shown in Fig. 11. TEM diffraction patterns for both stacking arrangements have been reported.[101]

At the present time there appears to be no structural information on the crystalline form of solids based on higher molecular weight fullerenes $C_n (n > 70)$.

C. Doped C_{60} crystals

Several stable crystalline phases for exohedrally doped or intercalated C_{60} have been identified. At present there is no structural information available for crystalline phases based on endohedrally doped fullerenes or for fullerenes with substitutional doping on the ball, as for example with boron atoms. Most widely studied are the crystalline phases formed by intercalation of alkali
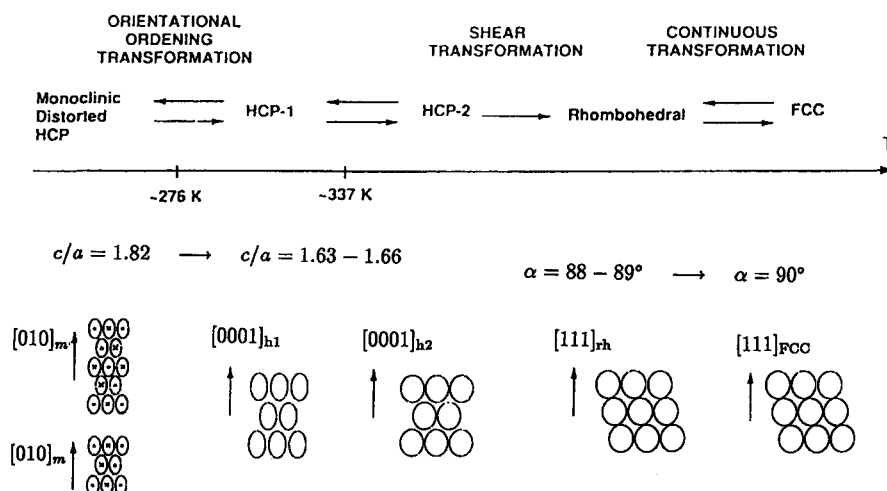

FIG. 10. Phase diagram shows the various phases of C_{70}, the possible phase transitions, and the stacking of the C_{70} molecules. The fcc phase is most stable at high temperatures which is continuously transformed to a similar rhombohedral phase. The HCP-2 phase that is close to the ideal c/a ratio lies close in energy to the fcc phase. Well-defined phase transitions to the hexagonal HCP-1 phase and to the monoclinically distorted HCP phase are observed.[88]
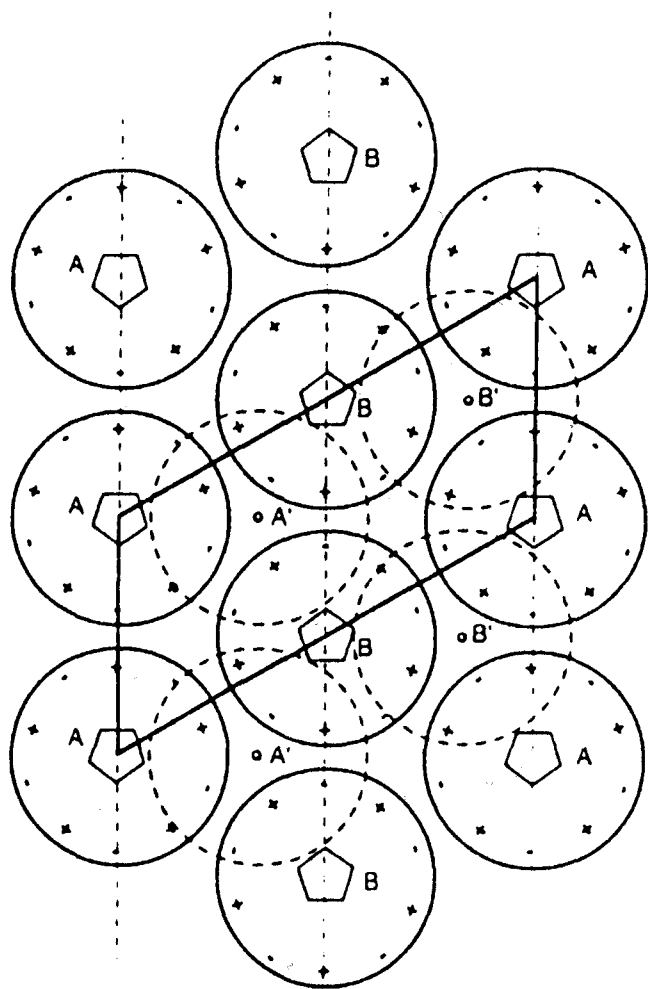
FIG. 11. Model for the stacking of orientationally ordered C_{70} molecules in the close-packed planes in the monoclinic phase. A and B (near the center of full circles) represent the two different orientations of molecules within a close-packed layer. The molecules A' and B' (near the center of dashed circles) are positioned in the next layer. Electron-rich and electron-poor regions are indicated with $+$ and $-$, respectively.[88]
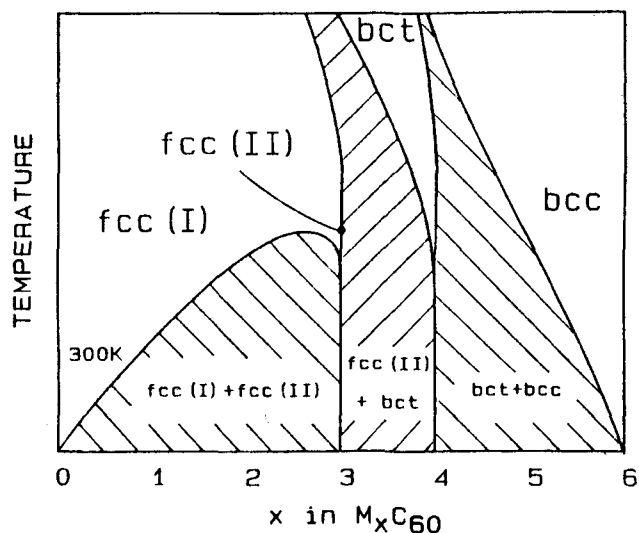

FIG. 12. Provisional binary phase diagram for M_xC_{60}. Shaded regions denote two-phase coexistence. The (linear) temperature scale is indicated approximately by the 300 K label in the lower left corner. The M_1C_{60} and the low temperature simple cubic C_{60} phases are not shown in this figure.[103]

metals, though some structural reports have been given for fullerene-derived crystals with alkaline earth[50] and iodine intercalants.[68]

When C_{60} is doped with the alkali metals (M $=$ K, Rb, and Cs), stable crystalline phases are formed for the compositions M_3C_{60}, M_4C_{60}, and M_6C_{60}.[89] These stable phases are illustrated in Fig. 12 which was experimentally determined for Rb-doped C_{60}, but is believed to be broadly applicable to the other heavy alkali metal M_xC_{60} compounds (M $=$ K, Cs).[103] In Fig. 12 fcc(I) refers to the C_{60} structure discussed in Sec. V. A, while fcc(II) refers to the fcc structure appropriate for M_3C_{60} discussed below. Thus, for $0 < x < 3$, phase separation between C_{60} and M_3C_{60} occurs; likewise, for $3 < x < 4$, the fcc(II) phase (stable at M_3C_{60}) coexists with the body-centered tetragonal (bct) phase (stable at M_4C_{60})

as discussed below. Finally, for $4 < x < 6$, the bct and bcc phases coexist, with the bcc phase stable at M_6C_{60}. The stability regions for each of the phases is shown schematically in Fig. 12.

Charge transfer of one electron per M atom to the C_{60} ball occurs, resulting in M^+ ions at the tetrahedral and/or octahedral interstices of the cubic C_{60} host structure. For the composition M_3C_{60}, the resulting metallic crystal has basically the fcc structure [see Fig. 7(c)]. Within this structure the alkali metal ions can sit on either tetragonal $(1/4, 1/4, 1/4)$ sites, which are twice as numerous as the octahedral $(1/2, 0, 0)$ sites (referenced to a simple cubic coordinate system). The electron-poor alkali metal ion tends to lie adjacent to a C$=$C double bond, thereby orienting the C_{60} molecules somewhat and restraining their rotational degrees of freedom.[34] From the standpoint of the near neighbors, the K guest species in K_3C_{60} sit between two C_{60} balls, on any one of four tetrahedral sites or two octahedral sites. For the tetrahedral sites, the radius of the cavity available to a K^+ ion is 1.12 Å, while for an octahedral site it is 2.07 Å,[52] as compared with 1.33 Å for the K^+ ion radius in ionic salts and 1.03 Å in the stage 1 graphite intercalation compound C_8K.[41] The shortest distance between a K^+ ion at a tetrahedral site and a carbon atom on a freely rotating C_{60} ball is 2.66 Å.[52] It is of interest to note that the Cs^+ ion is too large to form a stable Cs_3C_{60} compound with the $Fm\overline{3}m$ structure,[90] and this may be the reason why Cs_3C_{60} (which crystallizes in a bcc structure) is not superconducting (see Sec. XII).

Two other stable phases for M_xC_{60} (namely, M_4C_{60} for M $=$ K, Rb, and Cs and M_6C_{60} for M $=$ K, Rb, and

Cs) each have different crystalline structures. The M_4C_{60} phase [see Fig. 7(d)], which is more difficult to prepare than M_3C_{60} or M_6C_{60}, has a body-centered tetragonal structure (bct) with a tentatively assigned space group $I4/mmm$.[89] The compound M_6C_{60} has a body-centered cubic structure (bcc), as shown in Fig. 7(f) and corresponds to the space group T_h^5 or $(Im3)$. For M = K, Rb, and Cs, M_6C_{60} forms the alkali-metal-saturated compound, which is a semiconductor[43] (see Sec. VIII). A list of lattice constants for the various stable C_{60}-related structures is given in Table II for pristine and alkali-metal-doped M_xC_{60}.

Since the ionic radii of the alkali-metal ions Na^+ and Li^+ are both much smaller than the K^+, Rb^+, and Cs^+ ions, a number of unusual structural phenomena might be expected. Firstly, it is possible to fit more than one Na^+ in an octahedral site,[42,105] so that the cubic $Fm3m$ structure can be preserved upon adding six Na atoms with one Na ion in each of the two tetrahedral sites [see Fig. 7(b)] and up to four Na ions on octahedral sites [see Fig. 7(e)] to form Na_6C_{60}. The maximum stability for the four Na atoms on an octahedral site is at the corners of a regular tetrahedron with respect to the center of the octahedral sites.[42] Thus, there is no stable Na_3C_{60} crystal, and materials prepared with this stoichiometry tend to phase separate (disproportionate) into Na_2C_{60} [Fig. 7(b)] and Na_6C_{60} [Fig. 7(e)].[42] Also, because of the small ionic radius of sodium, the Na^+ ions tend to fill the smaller tetrahedral sites when alloys of Na with heavier alkali-metals are made, while the larger alkali metals tend to be on octahedral sites. One unusual effect is that alkali metal doping with Na_2Cs, Na_2Rb, Na_2K, and Li_2Cs results in a crystal with a closer $C_{60}-C_{60}$ separation than is present in undoped C_{60} (see Table II), presumably due to the attractive interaction between the metal ions and the fullerenes balls.[106]

The structure of the alkaline-earth metal compound Ca_yC_{60} (for $y \leqslant 5$) follows the same space group $Fm3m$ as for the heavy alkali metal M_xC_{60} compounds ($x \leqslant 3$),[50] and the Ca atoms occupy both tetrahedral and octahedral sites. Because of the smaller size of the calcium ion (as also noted above for the Na^+ ion[42]), the octahedral sites can accommodate multiple Ca ions, and it is believed that up to three Ca ions can be accommodated in a single octahedral site.[50] Also for Ca_5C_{60} the lattice constant $a_0 = 14.01$ Å is smaller than that for C_{60} prior to doping (see Table II). The structure of Ba_6C_{60} has also been investigated by x-ray powder diffraction techniques, showing the A15 structure typical of several BCS superconductors with T_c values above 10 K.[107] Unlike alkali-metal-doped C_{60}, where each M atom transfers one electron to C_{60}, the alkaline-earth metal dopants have been reported to transfer two electrons per metal dopant for low metal concentrations, but lower charge transfer values for high calcium concentrations.[50] The charge state of the metal ions in these intercalation compounds as a function of metal concentration is not as yet well established.

TABLE II. Lattice constants and superconducting T_c values for stable C_{60}-related materials.[89,104]

M_xC_{60}	Phase	Site symmetries[a]	Lattice constants (Å)	T_c (K)
Na_2RbC_{60}	fcc	O and T	14.091	$\cdots$
C_{60}	fcc	$\cdots$	14.110	$\cdots$
Na_2KC_{60}	fcc	O and T	14.120	$\cdots$
Na_2CsC_{60}	fcc	O and T	14.132	10.5
Na_3C_{60}	fcc	O and T	14.183	$\cdots$
Na_2C_{60}	fcc	T	14.189	$\cdots$
K_3C_{60}	fcc	O and T	14.253	19.3
K_2RbC_{60}	fcc	O and T	14.299	21.8
Rb_2KC_{60}	fcc	O and T	14.336	24.4
Na_6C_{60}	fcc	O and T	14.380	$\cdots$
Rb_3C_{60}	fcc	O and T	14.436	29.4
Rb_2CsC_{60}	fcc	O and T	14.493	31.3
K_4C_{60}	bct	T[b]	11.886(a), 10.774(c)	$\cdots$
Rb_4C_{60}	bct	T[b]	11.962(a), 11.022(c)	$\cdots$
Cs_4C_{60}	bct	T[b]	12.057(a), 11.443(c)	$\cdots$
Ca_5C_{60}	fcc	O and T	14.01	8.4
K_6C_{60}	bcc	T	11.385[c]	$\cdots$
Rb_6C_{60}	bcc	T	11.548[c]	$\cdots$

[a]The octahedral and tetrahedral site symmetries are denoted by O and T, respectively.

[b]Distorted tetragonal site. For the body-centered tetragonal structure (bct), the in-plane and c-axis lattice constants are denoted by a and c, respectively.

[c]To compare a_{fcc} with a_{bcc}, use the relation $a_{bcc} = a_{fcc}/\sqrt{2}$.

D. Other crystalline fullerene-related phases

The high electronegativity of pristine C_{60} hinders acceptor doping.[108] Consequently, relatively few C_{60} based acceptor compounds have been synthesized. Thus, few structural studies have thus far been made with acceptor compounds. Solid-state structures consisting of C_{60} and iodine species with a composition $C_{60}I_4$ have been reported for which the iodine molecules lie in planes between layers of C_{60} balls.[68] Several bromine-doped fullerene phases have been prepared and characterized.[109] Calculations of the electronic structure of other proposed halogenated C_{60} systems[108,110] suggest that several halogenated phases may be thermodynamically stable.

The acceptor compound that has thus far been studied in most detail is $C_{60}O$. NMR studies provide a sensitive technique for the presence of $C_{60}O$ through the appearance of additional NMR lines as inequivalent carbon sites appear in accordance with the various C–O distances that are possible. Structural studies show that $C_{60}O$ crystallizes in the same crystal structure as C_{60} (i.e., $Pa3$) and that $C_{60}O$ undergoes a first-order phase

transition at ~280 K. For the high temperature phase, the balls have three degrees of rotational motion, while the low T phase has only one degree of rotational motion or ratcheting. The transition temperature is about 25 K higher than for the similar phase transition in C_{60} because of the hindered rotational motion arising from the bonding to the oxygen.[59]

VI. VIBRATIONAL MODES

The normal modes for solid C_{60} can be clearly subdivided into two main categories: "intramolecular" and "intermolecular" modes, because of the apparent weak coupling between molecules. The former are often simply called "molecular" modes, since their frequencies and eigenvectors closely resemble those of an isolated molecule. The latter are also called lattice modes, and can be further subdivided into librational, acoustic, and optic modes. All of these modes, except the acoustic lattice modes, appear schematically in Fig. 13[21] where (a) and (b) refer, respectively, to the librational and optical lattice modes. The schematic density of states shown for these modes represents a true continuum, which is found throughout the entire Brillouin zone. The frequencies for these modes are low, reflecting the weak van der Waals bonds between fullerene molecules. In the limit that the molecule is treated as a "point", the molecular moment of inertia I approaches zero, and the librational modes are lost from the spectrum. The optic modes [Fig. 13(b)]

between adjacent C_{60} balls remain in this limit, and have been calculated by Wang and co-workers[111] using an appropriate van der Waals potential. The optic modes [Fig. 13(c)] between a C_{60}^- ion and an alkali metal ion are, of course, associated with metal-doped C_{60}, where electrons are transferred from the metal atom sublattice (e.g., Na, K, Rb, or Cs) to the C_{60} sublattice. Finally, Figs. 13(d) and 13(e) refer, respectively, to particular molecular modes (with H_g symmetry) that are Raman-active. The arrows indicate the C-atom displacements in each mode. The schematic density of states for all the molecular vibrations exhibits two broad peaks, with the lower and upper peaks associated, respectively, with the modes having predominantly radial and tangential molecular displacements, as discussed below. It should be noted that the overall schematic density of vibrational states in Fig. 13 is generally applicable to any fullerene solid. In considering other fullerene solids, it is necessary to consider the effect of the change in shape, mass, and moment of inertia for each fullerene species (i.e., C_{70}, C_{76}, C_{84}, C_{520}, etc.) for each type of contribution to the density of states in the fullerene solid.

Because of the high symmetry of the C_{60} molecule (point group I_h), there are only 46 distinct molecular mode frequencies corresponding to the $180 - 6 = 174$ degrees of freedom for the isolated C_{60} molecule, and of these only 4 are infrared-active (all with T_{1u} symmetry) and 10 are Raman-active (2 with A_g symmetry and 8 with H_g symmetry). The remaining 32 eigenfrequencies
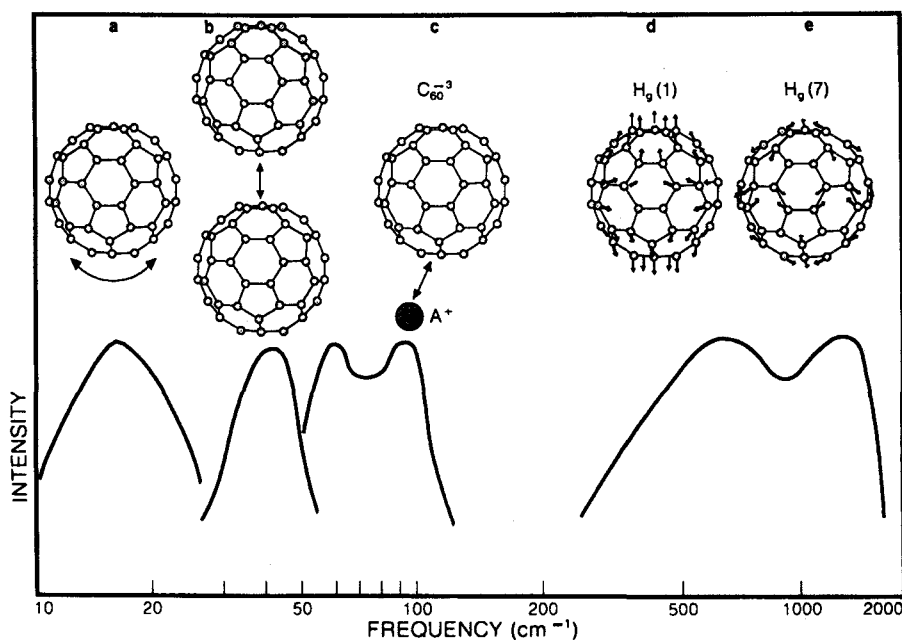

FIG. 13. Various librations and vibrations in the M_3C_{60} compounds. At lower frequencies, the compounds exhibit librational modes of individual C_{60} molecules (a), intermolecular modes (b), and optic modes (c). At higher frequencies, the intramolecular modes dominate; these "on-ball" modes have a radial character (d) at lower frequencies [for example the $H_g(1)$ mode] and a tangential character (e) at higher frequencies [for example, the $H_g(7)$ mode].[21]

correspond to silent modes. Raman and infrared spectroscopy provide sensitive methods for distinguishing C_{60} from higher molecular weight fullerenes with lower symmetry (e.g., C_{70} has D_{5h} symmetry). Since most of the higher molecular weight fullerenes have lower symmetry as well as more degrees of freedom, they have many more infrared- and Raman-active modes.

A. Infrared-active modes in C_{60}

The simplicity of the infrared spectrum of solid C_{60} [see Fig. 14(a)], which shows four prominent lines at 527, 576, 1183, 1428 cm^{-1},[17] provides a convenient method for characterizing the compositional purity of C_{60} samples, especially with regard to their contamination with C_{70} that has 53 Raman-active and 31 infrared-active modes (see Fig. 14).[17,112] The IR spectrum of solid C_{60} remains almost unchanged relative to the isolated C_{60} molecule, with the most prominent addition

being the weak feature at 1539 cm^{-1}.[113–115] The strong correspondence between the solution and/or gas phase IR spectrum and the solid-state IR spectrum is indicative of the highly molecular nature of solid C_{60}. The infrared spectra shown in Fig. 14 are for thin C_{60} and C_{70} films on alkali halide substrates. Figure 14 also shows the positions of the toluene bands, indicating how IR spectroscopy might be used to monitor the presence of residual solvent in fullerene-based solid-state samples at the 1–2% level.

B. Raman-active modes in C_{60}

Likewise, Raman spectroscopy (see Fig. 15)[116,117] provides valuable information about the intramolecular and intermolecular bonding in solid C_{60} and C_{60}-related compounds.[19,97,116–120] The Raman spectrum in Fig. 15 for solid C_{60} shows 10 strong Raman lines, the number of Raman-allowed modes expected for the free molecule. These lines are therefore assigned to intramolecular modes. As first calculated by Stanton and Newton,[121] the normal modes in molecular C_{60} above about 1000 cm^{-1} involve carbon atom displacements that are predomi-
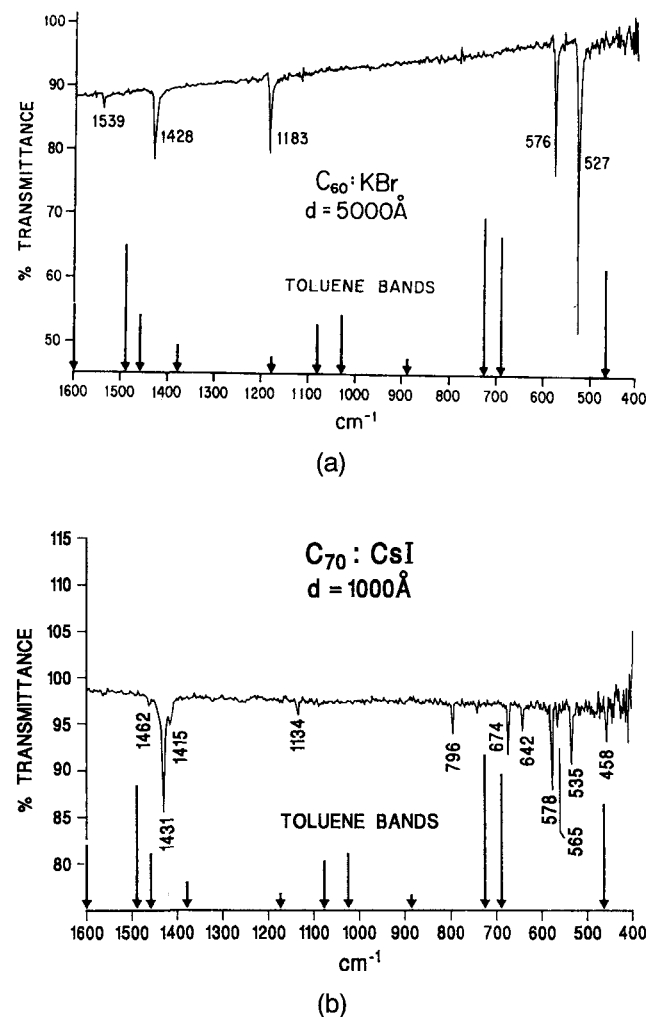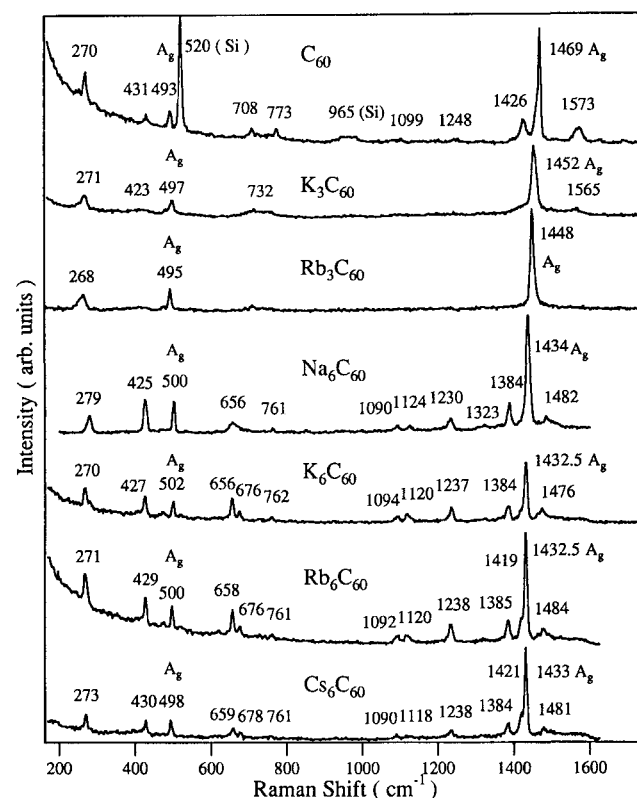

FIG. 14. The infrared spectra of (a) C_{60} and (b) C_{70}. Also shown schematically are the IR bands for toluene, a common solvent for fullerenes.[113] The spectra show no evidence for toluene contamination.

FIG. 15. Unpolarized Raman spectra ($T = 300$ K) for solid C_{60}, K_3C_{60}, Rb_3C_{60}, Na_6C_{60}, K_6C_{60}, Rb_6C_{60}, and Cs_6C_{60}.[116,117] The tangential and radial modes of A_g symmetry are identified, as are the features associated with the Si substrate (for the C_{60} trace). From these spectra it is concluded that the ball-ball interactions between the C_{60} molecules are weak, as are also the interactions between the balls and the alkali metal ions.

nantly tangential to the C_{60} ball surface, while the modes below ~ 800 cm^{-1} involve predominantly radial motion. Numerous calculations of the vibrational spectra for C_{60} have been carried out,[121–130] and from these calculations the symmetries and eigenvectors for the normal mode displacements for all the vibrational modes are available. Good agreement between the calculated and the experimentally measured mode frequencies has been obtained for some of these models.[122,130] The low frequency acoustic and rotational-librational modes associated with the displacements and rotations of the C_{60} balls in a cubic lattice have also been calculated,[111] and experimental low frequency Raman measurements on single crystals of C_{60} have also been made.[97] The displacements of adjacent atoms in the 493 cm^{-1} A_g radial breathing mode are in the radial direction and are of equal magnitude.

The A_g breathing mode at 1469 cm^{-1} corresponds to tangential displacements of the 5 carbon atoms around each of the 12 pentagons[113,131] and, therefore, is also called the "pentagonal pinch" mode. Under high laser flux from an Ar ion laser, this mode frequency downshifts to 1458 cm^{-1}, which has been interpreted as a signature of a photoinduced structural transformation.[131] The effect of phototransformation on the vibrational spectra of solid C_{60} is shown in Fig. 16,[60] where the infrared transmission and Raman spectra of solid C_{60} films can be compared for the pristine fcc phase (upper panel) and the phototransformed phase (lower panel). Phototransformation has been observed to occur at moderate optical flux >5 W/cm^2 in the visible and UV when applied to thin solid C_{60} films.[60] The effects observed in Fig. 16 have been interpreted by Rao et al.[60] as due to a photopolymerization of the lattice in which the C_{60} molecules become cross-linked by covalent, rather than van der Waals bonds. Numerous additional radial and tangential molecular modes are activated (Fig. 16) by the apparent breaking of the icosahedral symmetry resulting from bonds that cross-link adjacent molecules. A new Raman-active mode is also observed[60] at 116 cm^{-1} which is identified with a stretching of the cross-linking bonds between C_{60} molecules. This frequency falls in the gap between the lattice and molecular modes of pristine C_{60} (see Fig. 13).

Because of the metastability of the lowest lying triplet electronic state above the Fermi level (see Sec. VIII), it is possible to observe the Raman spectrum for C_{60} in this excited triplet state, and the frequency of the pentagonal pinch mode is found to be downshifted by ~ 11 cm^{-1} relative to that for the vibration in the electronic ground state.[97] In the solid phase, cubic crystal field interactions are expected to lower the symmetry of the lattice modes and to cause a splitting of the fivefold degenerate H_g-derived molecular modes, into threefold (T_g) and twofold (E_g) lattice modes. The study
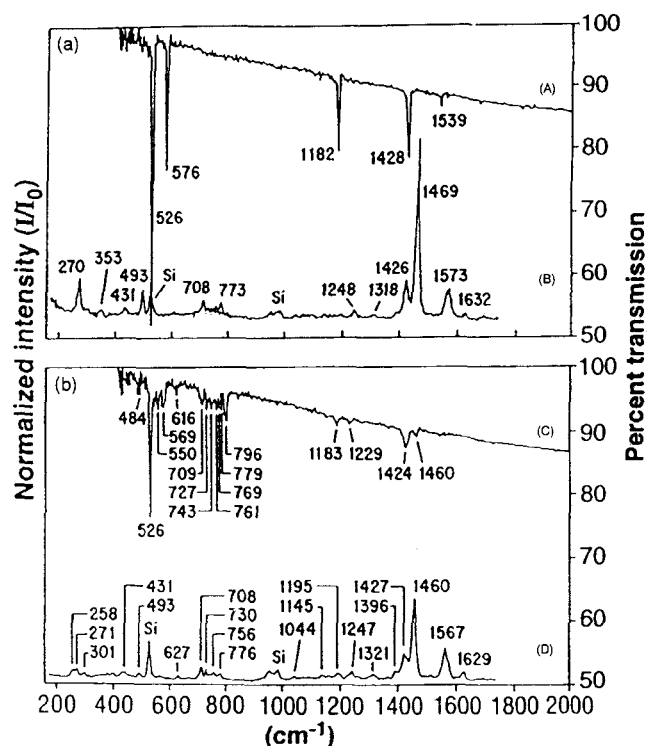

FIG. 16. Photoinduced dimerization and polymerization of C_{60}, as observed in the infrared and Raman spectra. The upper panel (a) shows infrared (A) and Raman (B) spectra for C_{60} taken with low incident optical power levels (<50 mW/mm^2). The lower panel (b) shows the corresponding infrared (C) and Raman (D) spectra taken after exposure of the C_{60} film to intense optical power levels for several hours, until the Raman line at 1469 cm^{-1} disappeared. After the intense optical irradiation, many more infrared and Raman lines appear in these spectra, due to a lowering of the symmetry caused by the photoinduced covalent bonding between the fullerene molecules.[60]

of line splittings and their symmetry in solid C_{60} requires the use of single crystals and polarization studies.[77,113] Studies of the temperature dependence of the Raman spectra have been used to monitor the effect of the 255 K phase transition on the line shifts, linewidths, line splittings, and their symmetries.[97] The splittings observed in Ref. 97 have subsequently been reinterpreted in terms of higher order Raman processes.[132]

C. Silent modes in C_{60}

Singlet oxygen photoluminescence (PL) has been shown to provide a powerful probe of all the intramolecular vibrational modes of C_{60} (see Fig. 17).[133] Other techniques providing detailed information on all vibrational modes include inelastic neutron scattering[134] and electron energy loss spectroscopy. The applicability of the photoluminescence technique to probe fundamental vibrational excitations of C_{60} is based on the weak vibronic coupling of the intercalated O_2 molecules to the C_{60} lattice (see Sec. IX). Raman scattering studies had shown previously that this coupling is indeed weak, as
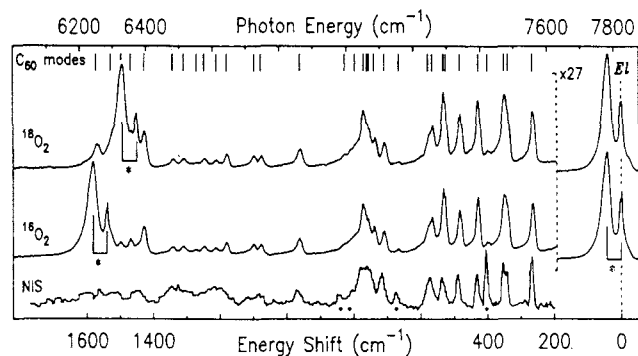
FIG. 17. Photoluminescence (PL) spectra of C_{60} films exposed to $^{18}O_2$, top, and $^{16}O_2$, middle, at $T = 4.2$ K, with 720 nm optical excitation.[133] The photon energy scale for the PL is shown on the top, and directly below is a vibrational mode energy scale measured from the purely electronic principal transition, labeled El. The asterisks indicate the O_2 vibrational mode replica of the strong doublet. The bottom curve is the inelastic neutron scattering data of Ref. 134.

no shifts in the Raman-active C_{60} mode frequencies were detected upon oxygen intercalation.[131] This Raman study further inferred the presence of oxygen as O_2, rather than as atomic oxygen bonded to the C_{60} molecule, which is directly confirmed by the singlet oxygen PL spectra. More importantly, the vibronic coupling between the O_2 and C_{60} allows the molecular vibrational frequencies of C_{60} to appear as sidebands on the $T = 4.2$ K luminescence emission spectra as dioxygen returns to the triplet ground state (^3A_g) from the first excited singlet state (^1D_g), as shown in Fig. 17. The upper two PL spectra in the figure are from $^{18}O_2$ and $^{16}O_2$, respectively, whereas the bottom vibrational spectrum is obtained from inelastic neutron scattering studies of microcrystalline C_{60} powders.[133] As can be seen from the figure, remarkably good agreement is obtained between the PL vibrational sidebands and the more conventional inelastic neutron scattering probe. Furthermore, the higher energy mode structure (>700 cm^{-1}) is much sharper in the PL data than in the inelastic neutron scattering data, thereby yielding more reliable values for the mode frequencies. Thirty-two of the 46 vibrational modes for C_{60} are seen in the PL spectra, many of which are unobservable in the first-order Raman or IR spectra due to symmetry considerations. However, higher-order Raman and infrared spectra allow a determination of all silent modes for C_{60} to be made.[132]

D. Vibrational spectra for C_{70}

The Raman and infrared spectra for C_{70} are much more complicated than for C_{60} because of the lower symmetry and the large number of Raman-active modes (53) and infrared-active modes (31) out of a total of 122 possible vibrational mode frequencies. Nevertheless, well-resolved infrared spectra[112,135] and Raman spectra

have been observed.[118,135,136] Using polarization studies and a force constant model calculation,[135,137] the mode symmetries have been identified. Making use of a force constant model based on C_{60} and a small perturbation to account for the weakening of the force constants for the belt atoms, good agreement between the model calculation and the experimentally determined lattice mode frequencies[135,137] has been achieved.

E. Vibrational modes in doped fullerene solids

The addition of alkali metal dopants to form the superconducting M_3C_{60} (M = K, Rb) compounds and the alkali-metal-saturated compounds M_6C_{60} (M = Na, K, Rb, and Cs) perturbs the observed Raman spectra only slightly[138–140] relative to the solution molecular spectra and the spectra in the undoped solid C_{60}, as shown in Fig. 15 where the Raman spectra for solid C_{60} are presented in comparison to various M_3C_{60} and M_6C_{60} spectra.[116,117] One can, in fact, identify each of the lines in the M_6C_{60} spectra with those of pristine C_{60}, and very little change is found from one alkali metal dopant to another.[117] The small magnitude of the perturbation of the Raman spectrum by alkali metal doping and the insensitivity of the M_6C_{60} spectra to the specific alkali metal species indicate a very weak coupling between the C_{60} balls and the M^+ ions. In the case of the superconducting M_3C_{60} phase (M = K, Rb), the Raman spectra (see Fig. 15) are again quite similar to that of C_{60}, except for the apparent absence in the M_3C_{60} spectra of several of the Raman lines derived from the H_g modes in C_{60}. This is particularly true in the spectrum of Rb_3C_{60} for which the same sample was shown resistively to exhibit a $T_c \sim 28$ K.[138] For the case of K_3C_{60} (see Fig. 18)[116] and Rb_3C_{60},[141] the coupling between the phonons and a low energy continuum strongly broadens the H_g-derived modes[116,120] and gives rise to modifications in the Raman lineshape. For example, in both K_3C_{60} and Rb_3C_{60}, the 270 cm^{-1} line shows a distinct Breit–Wigner–Fano lineshape.[141] As discussed in Sec. VIII, the electronic structure for K_3C_{60} and Rb_3C_{60} is described in terms of a band model while that for the M_6C_{60} compounds is best described by levels for a molecular solid. Furthermore, the molecular ions in the M_3C_{60} compounds experience a Jahn–Teller distortion while the M_6C_{60} compounds do not (see Sec. VIII). The symmetry lowering resulting from the Jahn–Teller distortion or the electron-phonon interaction may be possible causes for the broadening (or splitting) of some of the degenerate vibrational modes in the M_3C_{60} spectra.

As a result of alkali metal doping, electrons are transferred to the π-electron orbitals on the surface of the C_{60} molecules, elongating the C–C bonds and down-shifting the intramolecular tangential modes. A similar effect was noted in alkali-metal-intercalated graphite
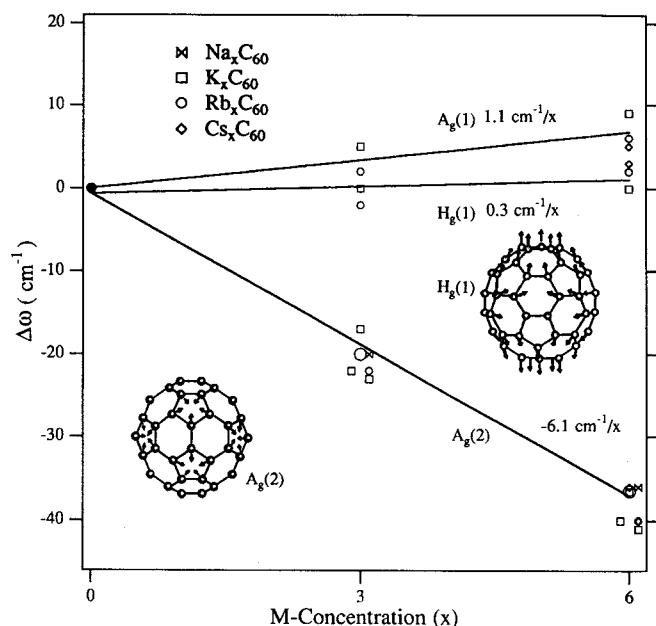
2070

J. Mater. Res., Vol. 8, No. 8, Aug 1993

FIG. 18. Dependence of the frequencies of the $A_g(1)$, $A_g(2)$, and $H_g(1)$ modes on alkali metal concentration x in M_xC_{60}, where M = Na, K, Rb, and Cs. The frequency shifts of these Raman modes are plotted relative to the C_{60} frequencies $\omega[A_g(1)] = 493$ cm^{-1}, $\omega[A_g(2)] = 1469$ cm^{-1}, and $\omega[H_g(1)] = 270$ cm^{-1} at $T = 300$ K. A schematic of the displacements for the eigenvectors for the $A_g(2)$ "pentagonal pinch" and $H_g(1)$ modes are shown. All the C atom displacements for the $A_g(1)$ mode are radial and of equal magnitude. Data from Ref. 139 and Ref. 140 are artificially displaced to the left, and right, respectively. The centered data are from Ref. 113.

where electrons are transferred from the alkali-metal M layers to the graphene layers.[142] The magnitude of the mode softening in alkali-metal-doped C_{60} is comparable (~60% of that for alkali metal-doped GIC's) and can be explained semiquantitatively by a charge transfer model.[143] Referring to Fig. 18, the dependence of the Raman frequencies on M concentration x for three dominant modes in M_xC_{60} (M = K, Rb, and Cs) is presented. The data in Fig. 18 come from several publications of the Kentucky, Vienna, and AT&T research groups.[113,139,140] Two of the three mode eigenvectors [$A_g(2)$, tangential: 1469 cm^{-1}] [$H_g(1)$, radial: 270 cm^{-1}] are also shown in the figure. The third eigenvector is the radial breathing mode [$A_g(1)$ at 493 cm^{-1}] and is not shown because it is easy to visualize the symmetric radial displacements for this particular eigenmode.

The softening of the 1469 cm^{-1} tangential $A_g(2)$ mode by alkali metal doping has been used as a convenient method to characterize the stoichiometry x of stable K_xC_{60} samples. This mode in M_xC_{60} is downshifted by ~6 cm^{-1}/M atom, based on direct measurements on the stable compounds K_3C_{60} and K_6C_{60}.[113] Furthermore, since all end-point M_6C_{60} compounds (M = K, Rb, and Cs) exhibit approximately the same value for the $A_g(2)$ mode frequency (1432 cm^{-1}), it is reasonable to expect

that a downshift of ~6 cm^{-1}/M atom is approximately applicable also for Rb and Cs. The radial $A_g(1)$ mode, on the other hand, stiffens slightly due to competing effects associated with a mode softening arising from the charge transfer effect (similar to the situation for the tangential modes) and a larger mode stiffening effect due to electrostatic interactions between the charged C_{60} ball and the surrounding charged alkali atoms as their atomic separations change during a normal mode displacement.[143]

The introduction of alkali metal dopants into the lattice is expected to give rise to low frequency vibrational modes whereby the alkali metal ions vibrate relative to the larger fullerene balls. Such modes should be accessible for investigation by Raman and infrared spectroscopy, as well as other techniques.

VII. THERMAL PROPERTIES

Thermal properties normally include properties such as the specific heat, the temperature coefficient of lattice expansion, and thermal transport properties, such as the thermal conductivity and the thermoelectric power. In this section we review the thermal properties for fullerenes, as well as the lattice contribution to the thermal conductivity, which is the dominant contribution to the thermal conductivity for fullerenes. The electronic contribution to the thermal conductivity and the thermo-electric power are both reviewed in the discussion of transport properties (see Sec. X).

A. Specific heat

Measurement of the temperature dependence of the specific heat $C_p(T)$ provides the most direct method for the study of the temperature evolution of the degrees of freedom of phase transitions, the enthalpy change and the entropy change associated with these phase transitions if they are first order, the identification of higher order phase transitions, and the other thermal consequences of structural rearrangements. Because of the different structures of the various fullerene molecules, and the different crystal structures possible in the solid state, the various fullerenes experience different phase transitions and, hence, distinct $C_p(T)$ curves. Thus far, reliable specific heat data are available only for undoped C_{60} and C_{70}.

If the specific heat anomalies associated with phase transitions are removed from the $C_p(T)$ data, then the temperature dependence of the residual specific heat contribution for C_{60} is in good agreement with that of graphite[144,145] for $T \geqslant 250$ K. This similarity with graphite has been noted by various authors[63,64,93] and indicates similarities in the degrees of freedom of the carbon atoms in these two allotropic forms of carbon over this temperature range. The corresponding residual

specific heat for C_{70} is higher than that for graphite, and the reason for this difference is not presently understood.

The dominant feature in the temperature dependence of the specific heat for C_{60} is the large specific heat anomaly that is observed near 260 K (see Fig. 19).[63,64,93,94,99] The most accurate measurement of this specific heat anomaly was done at a 10 K/min heating rate, yielding a transition temperature $T_c = 257.6$ K, with an associated enthalpy change for a highly crystalline sample of $\Delta H = 7.54$ kJ/mole and an entropy change of 30.0 J/K mole.[94] This specific heat anomaly is associated with a first order transition in the solid phase, corresponding to the transition from the fcc space group $Fm\overline{3}m$ for the higher temperature phase where all the C_{60} balls are freely rotating, to the low temperature $Pa\overline{3}$ structure where each of the four C_{60} molecules within the cubic unit cell ratchets about a different $\langle 111 \rangle$ axis (see Sec. V.A). Confirmation for this structural phase transition is provided by many independent experimental techniques (see Sec. V.A).

Upon further cooling of crystalline C_{60}, a second anomaly in $C_p(T)$ is observed, with a peak in the specific heat at 165 K. Other evidence for a phase transition near 165 K comes from measurements of the temperature dependence of the dielectric relaxation,[100] of the ultrasonic velocity and attenuation,[62] and structural studies,[35] though it has been difficult to obtain direct information by x-ray diffraction techniques regarding the structural changes associated with this phase transition. An activation energy of ~290 meV may be associated with the potential energy barrier that must be overcome to make a transition between the orientation of adjacent C_{60} balls, such that the electron-rich double bond on one ball faces an electron-poor pentagonal face on the adjacent ball (lower energy state) on one hand, or faces an electron-poor hexagonal face (higher energy state) on

the other hand.[35,100] The hysteresis in the $C_p(T)$ data suggests that on heating from below 165 K, the C_{60} crystal remains in the low T phase (stable below 165 K) until a temperature of ~260 K is reached, where the transition to the fcc structural phase occurs.[65]

When cooling below 260 K, the free rotation of the molecule is replaced by a ratcheting motion that quickly rotates the C_{60} balls by 60° around a $\langle 111 \rangle$ axis, so that the electron-rich double-bond on one ball is adjacent to an electron-poor pentagonal (or hexagonal) face. As T is reduced, the fraction of C_{60} balls with double bonds opposite pentagonal faces grows relative to those with double bonds opposite hexagonal faces until about 90 K, where about 83% of the molecules are in the lower energy configuration.[35,94] The molecules in the higher energy structural state are randomly distributed in space with respect to the molecules in the lower energy state. Thus, at low temperatures, C_{60} is in a structurally disordered state with ~1/8 of the C_{60} molecules randomly oriented in the higher energy state, consistent with detailed low temperature specific heat measurements that provide strong evidence for a glassy phase below 20 K,[94,99] yielding an enthalpy change of 22.2 kJ/mole, a change in the heat capacity of 7 J/K mole, and a relaxation time of 4×10^{-11} s. Several workers have given evidence for another phase transition through a spatial ordering of molecules in each of the potential minima, yielding an enlargement (doubling) of the unit cell.[101] Others have found a change in slope of the $C_p(T)$ curve at 50 K,[65,93,94] with an excess specific heat that has an activation energy of 40 meV. At very low T (below 8 K), a T^3 dependence of $C_p(T)$ is observed, yielding a Debye temperature of 185 K.[65]

For C_{70}, two specific heat anomalies are observed at 337 K and 280 K, corresponding to enthalpy changes of 2.2 J/g and 3.2 J/g, respectively.[64] Structural studies[88] show a phase transition from a hexagonal close-packed HCP-2 structure with freely rotating C_{70} molecules and $c/a = 1.63$ to a second HCP-1 structure at 337 K where the fivefold axes of the C_{70} molecule are aligned (see Sec. IV.B). At ~276 K, structural studies indicate that rotations about the fivefold axes cease, as the molecules align in a monoclinic structure corresponding to a distorted HCP structure with $c/a = 1.82$. Whereas the background $C_p(T)$ for C_{60} at high T is essentially the same as that for graphite, the background $C_p(T)$ for C_{70}, after the specific heat anomalies at 337 K and 280 K are subtracted, is significantly higher than that for C_{60}.[64]

An anomaly in the specific heat for C_{70} is observed at 50 K, similar to that observed for C_{60}.[64] The low temperature measurements (<8 K) show a T^3 law from which a Debye temperature of 145 K is estimated; the high value for the low temperature $C_p(T)$ is attributed[64] to librational intermolecular modes.[134,146]
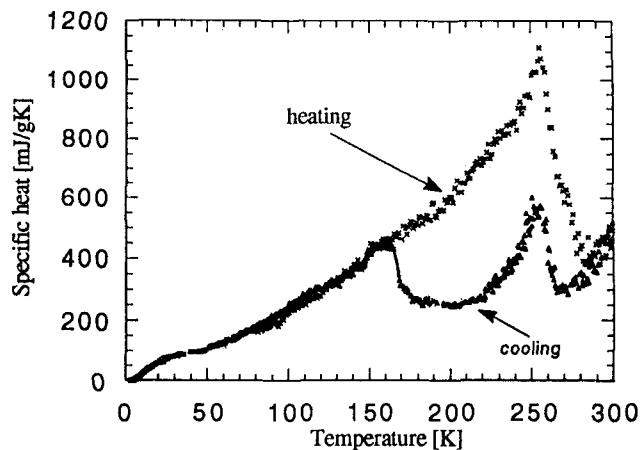

FIG. 19. Comparison between the temperature dependence of the specific heat for C_{60} on cooling ($\triangle$) and heating ($\times$).[63]

2072

J. Mater. Res., Vol. 8, No. 8, Aug 1993

B. Temperature coefficient of thermal expansion

The temperature dependence of the lattice constant a_0 for C_{60} (see Fig. 20) shows a large discontinuity in a_0 at the 255 K structural phase transition[35,59] (see Secs. V. A and V. B). The change in a_0 was found to be 0.044 ± 0.004 Å on heating,[59] indicative of a first-order phase transition, and consistent with other experiments, especially the heat capacity (see Sec. VII. A). From the Clausius–Clapeyron equation, measurements of the latent heat at the 255 K phase transition yield a value for the fractional change in the volume of the unit cell of $\Delta V/V = 7.5 \times 10^{-3}$,[147] which is in reasonable agreement with the direct structural measurement of $9.3 \pm 0.8 \times 10^{-3}$.[59] The average isobaric volume coefficient of thermal expansion both below and above the 255 K transition is $6.2 \pm 0.2 \times 10^{-5}$/K. A change in the slope of $a_0(T)$ is also found at $\sim$90 K as seen in the inset for Fig. 20.[35]

C. Lattice contribution to the thermal conductivity

Because of the low carrier concentration in C_{60} and related compounds, the dominant contribution to the thermal conductivity is due to the lattice vibrations. Thus far, the available published data for the temperature dependence of the thermal conductivity $\kappa(T)$ are limited and relate to single crystal C_{60}, with $\kappa(T)$ given over a limited temperature range (from 30 K to 300 K).[66] These results show an anomaly in $\kappa(T)$ near 260 K associated with a first-order structural phase transition (see Sec. V. A). The $\kappa(T)$ results further show the magnitude of the maximum thermal conductivity κ_{max} to be more than three orders of magnitude less than for graphite (in-plane)[148,149] and diamond.[150] The authors attribute their low value of the thermal conductivity κ_{max} to both a high density of defect states and a low Debye temperature in C_{60} (compared to graphite). To model the observed

FIG. 20. Temperature variation of the cubic lattice constant a_0 for solid C_{60}. The inset shows the low temperature data for a_0 on an expanded scale.[59]

temperature dependence of $\kappa(T)$, two nearly degenerate molecular orientations are considered (differing by $\sim$12 meV in energy), and separated by an energy barrier of $\sim$260 meV. One interpretation of this result, consistent with specific heat measurements (see Sec. VII. A) and structural measurements (see Sec. V. A), suggests that the lower energy of $\sim$12 meV may relate to the energy difference between the orientation of the double bonds opposite pentagonal faces relative to hexagonal faces, and the larger energy of $\sim$260 meV may correspond to the energy barrier that must be overcome in making the transition from the higher-lying hexagonal face orientation to the lower energy pentagonal face orientation opposite the double bond in the adjacent C_{60} ball (see Sec. V. A and Sec. VII. A). We can expect future research on $\kappa(T)$ for C_{60} to yield important information on the vibrational mode scattering mechanisms and on the vibrational excitation spectrum. Thermal conductivity measurements for doped C_{60} or for higher mass fullerenes are not yet available.

VIII. ELECTRONIC STRUCTURE

On the basis of the spectroscopic studies discussed in Sec. VI, it is concluded that fullerenes form molecular solids. Thus, their electronic structures are expected to be closely related to the electronic levels of the isolated molecules. Each carbon atom in C_{60} has two single bonds along adjacent sides of a pentagon and one double bond between two adjoining hexagons. If these bonds were coplanar, they would be very similar to the sp^2 trigonal bonding in graphite. The curvature of the C_{60} surface causes the planar-derived trigonal orbitals to hybridize, thereby admixing some sp^3 character to the sp^2 bonding. The shortening of the double bonds and lengthening of the single bonds in the Kekulé arrangement of the C_{60} molecule also strongly influence the electronic structure.

The most extensive calculations of the electronic structure of fullerenes have been done for C_{60}. To obtain the molecular orbitals for C_{60}, the multielectron problem for the free molecule must first be solved.[151,152] Representative results for the free C_{60} molecule are shown in Fig. 21(a). Because of the molecular nature of solid C_{60}, the electronic structure for the solid phase would be expected to be closely related to that of the free molecule, and some authors have followed this approach.[153] As is shown in Sec. IX, where the optical properties of fullerenes are discussed, a molecular approach can more easily explain a large body of experimental observations pertinent to the optical properties of C_{60}, which are difficult to explain on the basis of a one-electron energy band picture.

Nevertheless, more attention has, until recently, been given to a band structure approach. An example of a band structure model for C_{60} is given in Fig. 21(b)
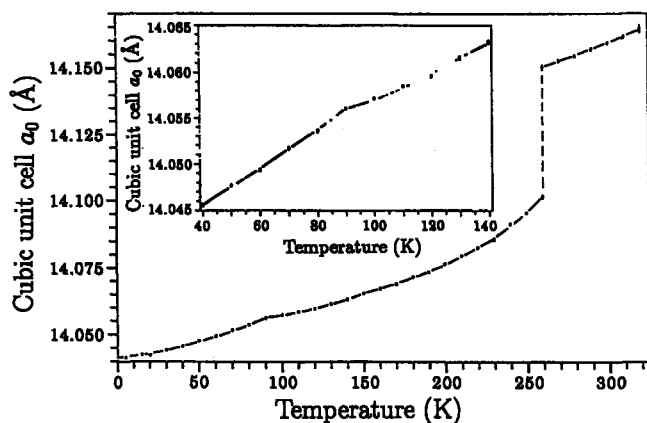
where we see results for the fcc solid, based on total energy calculations using norm-conserving pseudo-potentials, a local density approximation in density functional theory, and a Gaussian orbital basis set.[152] The various band calculations for C_{60}[108,152] yield a narrow band ($\sim$0.4–0.6 eV bandwidth) solid, with a HOMO–LUMO-derived direct band gap of $\sim$1.5 eV at the X point of the fcc Brillouin zone. Since the HOMO and LUMO levels have the same odd parity, electric dipole transitions between these levels are symmetry forbidden in the free C_{60} molecule. (See Sec. IX for a discussion of the optical properties of C_{60}.) In the solid, transitions between the direct bandgap states at the Γ and X points in the cubic Brillouin zone are also symmetry forbidden, but are allowed at the lower symmetry points in the Brillouin zone. The allowed electric dipole transitions for the free C_{60} molecule are indicated by arrows in Fig. 21(a).

A molecular model for the electronic states of C_{60} might provide a better starting point than does the band model for discussing the following optical properties of C_{60}: (1) a difference in energy between the observed HOMO–LUMO absorption and luminescence bands, (2) the optical limiting effect (see Sec. XV), (3) a down-shift in the frequency of the Raman-active pentagonal pinch mode in the excited state relative to the ground state, (4) a strong effect of the presence of oxygen on the optical spectra of C_{60}, and (5) a large optically induced chemical reactivity. In Sec. IX we present an explanation of these optical phenomena in terms of a molecular approach to the electronic structure of excited states. In

this section, we present a brief review of the molecular approach to the electronic structure in the absence of optical excitations.

According to the molecular approach, many-electron-orbitals for the "valence" and "conduction" electron states are constructed for the π-electrons on the C_{60} molecule. The lower-lying σ orbitals are filled and are not generally probed by optical experiments. The number of π-electrons on the C_{60} molecule is 60 (i.e., one state per carbon atom), which is exactly the correct number to fully occupy the h_u (HOMO) level, specifying its symmetry in terms of the icosahedral group I_h. In relating the icosahedral levels to those of full rotational symmetry, we note that 50 π-electrons fully occupy the angular momentum states through $l = 4$, and the remaining 10 electrons are available to start filling the $l = 5$ state.

In full spherical symmetry, the $l = 5$ state can accommodate 22 electrons, and the splitting of the $l = 5$ rotational state in icosahedral symmetry is into the $H_u + F_{1u} + F_{2u}$ irreducible representations. The level of lowest energy by Hund's rule is the fivefold H_u level which is completely filled by the 10 available electrons. The h_u^{10} ground state configuration by Hund's rule is nondegenerate and has quantum numbers $L = 0$, $S = 0$, $J = 0$, and A_g symmetry within the point group I_h. Neglecting any thermal excitation, the two threefold F_{1u} and F_{2u} (some authors refer to these levels as T_{1u} and T_{2u}) levels in icosahedral symmetry are empty. Whether C_{60} is considered in terms of a spherical approximation or from its icosahedral symmetry, the ground state is
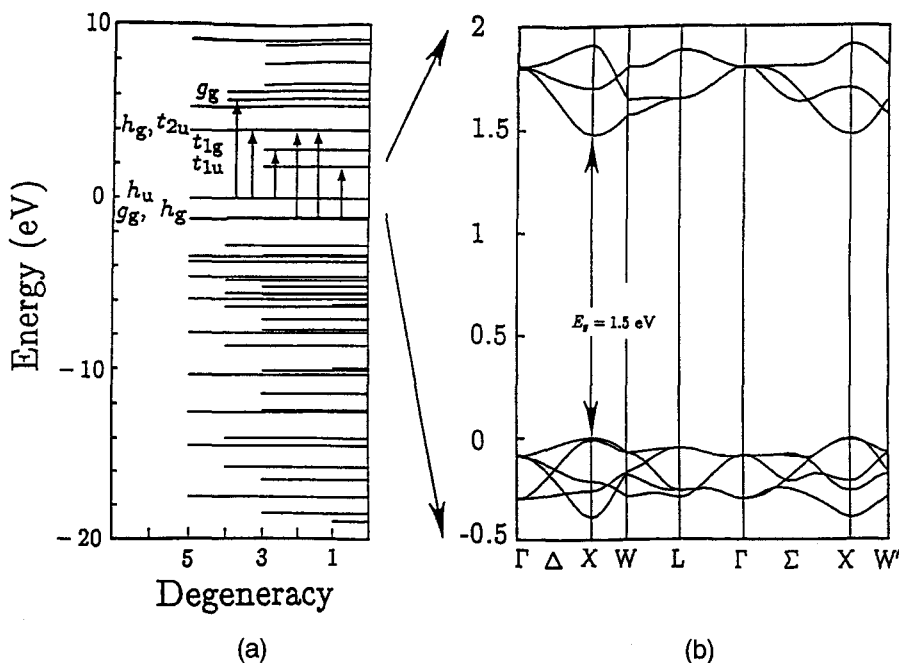

FIG. 21. Calculated electronic structure of (a) an isolated C_{60} molecule and (b) fcc solid C_{60} where the direct band gap at the X-point is calculated to be 1.5 eV.[152]

nondegenerate with a total angular momentum of $J = 0$, and this special circumstance has been suggested as being in part responsible for the high stability of the C_{60} molecule.[154]

To treat some of the physical properties of C_{60}, it is necessary to consider the electronic levels for fullerene-derived ions, which we denote by $C_{60}^{n\pm}$. We can further denote the electronic configurations forming the many-electron states by $h_u^{10} f_{1u}^n$ for an excess charge of n electrons or by h_u^{10-p} for p holes. The symmetries for these many-body π-electron states for C_{60} have been investigated,[154] and more detailed calculations of the actual energy levels have also been carried out[155,156] in some cases.

Photoemission and inverse photoemission experiments on $M_x C_{60}$ for M = K, Rb, and Na (and their alloys)[42,43,157] show direct evidence for the filling of the LUMO levels upon alkali metal doping, consistent with optical and transport measurements, but the implied energy gap in the density of states for these experiments is sensitive to screening and correlation effects. Calculations to explain the photoemission and inverse photoemission spectra[126,152,158–161] have been based on band models for the electronic states. Photoemission experiments are of particular interest to theoreticians because excitonic effects and vibronic processes, which must be considered for optical phenomena, do not affect photoemission processes.

Total energy calculations on $K_x C_{60}$ show that the tetrahedral sites fill up before the octahedral sites.[152] Doping C_{60} with an alkali metal transfers electrons to the LUMO levels, which because of their F_{1u} (T_{1u}) symmetry (Fig. 21) can accommodate three spin up and three spin down electrons. Assuming one electron to be transferred to the C_{60} ball per alkali-metal atom dopant, the LUMO levels are expected to be half occupied at the alkali metal stoichiometry $M_3 C_{60}$ and totally full at $M_6 C_{60}$, leading to a filled shell configuration with A_g symmetry. Thus, $M_6 C_{60}$ would be expected to be semiconducting with a band gap between the F_{1u} and F_{2g} (T_{1u} and T_{2g}) levels (see Fig. 21), while $M_3 C_{60}$ should be metallic provided that no bandgap is introduced at the Fermi level by a Peierls distortion. Since the C_{60}^{3-} ion has a fourfold degenerate ground state (double group Γ_8^- irreducible representation[154]) in icosahedral symmetry, a Jahn–Teller distortion would be expected, so that a nondegenerate ground state could be achieved. A large increase in optical absorptivity in $M_x C_{60}$ with alkali metal doping is observed as $x \rightarrow 3$, and this observation supports the metallic nature of $M_3 C_{60}$ (see Sec. IX), in agreement with the transport properties of $M_x C_{60}$ discussed in Sec. X. Below ~ 0.5 eV, the free electron contribution to the optical properties is dominant, and above ~ 0.5 eV, interband transitions

from the partially occupied F_{1u} level to the higher lying F_{1g} level take place. It should be emphasized that the level-filling arguments for $M_x C_{60}$ pertain to the free molecule as well as to the levels in the solid state.

Using a local density approximation, calculations of the energy levels of C_{60} endohedrally doped with K, O, and Cl (at the center of the C_{60} ball) show that the $4s$ level of K lies high above the Fermi level and that the valence electron originally on the K atom is transferred to the C_{60}-derived F_{1u} (T_{1u}) LUMO level.[70] In contrast, the O- and Cl-derived levels are found to lie at E_F, and these levels are partly filled with 4 and 5 electrons, respectively, showing little interaction between the F_{1u}-derived dopant levels and the F_{1u} (T_{1u}) levels of C_{60}.[70] Total energy calculations for exohedrally placed bromine[110] suggested that $C_{60}Br$ should be successfully synthesized, and subsequent to these calculations $C_{60}Br_x$ compounds have been successfully synthesized.[40] However, because of the high electronegativity of C_{60}, it is not likely that holes would be created in the H_u-derived C_{60} HOMO level, also in agreement with experiment.[54]

Fermi surface calculations for $K_3 C_{60}$ indicate a hole Fermi surface around the Γ-point that contributes about 12% to the density of states at the Fermi surface.[162] These calculations also indicate a larger and more complicated Fermi surface consisting of both electron and hole orbits that contribute the remaining 88% to the density of states. The total density of states at E_F is estimated to be between 20 and 25/eV/C_{60} molecule.[108,163,164] No direct measurements of the Fermi surface topology for any of the $M_3 C_{60}$ materials are yet available. Indeed, the molecular approach suggested by the optical data would preclude such experiments for $M_x C_{60}$, $x \neq 3$. Furthermore, Fermi surface measurements in $M_3 C_{60}$ may be difficult to carry out because of the heavy effective masses m^* of the carriers. Calculated values for m^* based on a band model yield $1.3 m_e$ (where m_e is the free electron mass) for the conduction band of C_{60} and $1.5 m_e$ and $3.4 m_e$ for the valence bands (see Table III).[108]

Because of the weak interaction of the balls with each other and with the alkali metal dopants, solid $M_3 C_{60}$, though showing transport properties consistent with a one-electron band model, is close to being a molecular solid, having energy levels with little dispersion, thus giving rise to a very high density of states near the Fermi level. This property may be important in understanding superconductivity in $M_3 C_{60}$, discussed in Sec. XII. Because of the importance of the $K_3 C_{60}$ and $Rb_3 C_{60}$ compounds for understanding the superconductivity in fullerene-derived materials, some values of the physical constants for $K_3 C_{60}$ and $Rb_3 C_{60}$ in the normal state are listed in Table III.

IX. OPTICAL PROPERTIES

Since the optical transitions near the HOMO–LUMO gap are symmetry-forbidden (see Sec. VIII), and their absorption strengths are consequently very low, study of the absorption edge in C_{60} is difficult from both an experimental and theoretical standpoint. To compound this difficulty experimentally, C_{60} is strongly photosensitive, so that unless measurements are made under low light intensities, photoinduced chemical reactions take place, in some cases giving rise to irreversible structural changes and polymerization.[60] Therefore, it has taken more time to clarify the optical properties of fullerenes, relative to some of their other physical properties.

One of the important and striking features of the optical properties of C_{60} is the large difference between the lowest energy absorption band[79] and the lowest energy luminescence band.[94,165,166] In the following, we present the experimental basis for this phenomenon and then offer an explanation for its occurrence, based on an excitonic model for optical transitions that follows directly from the electronic structure presented in Sec. VIII.

Early research on the separation of C_{60} from impurities and higher fullerenes using liquid chromatography (LC) demonstrated[79] that fullerenes in solution (organic solvents) exhibited characteristic colors that would be useful for identifying and purifying these fullerenes. For example, C_{60} and C_{70} appear magenta and reddish-orange, respectively, in toluene and benzene. This visual characterization of the undoped fullerenes is the most common utilization of the optical properties of fullerenes for sample characterization.

The most sensitive measurement of the optical absorption spectra is to probe the spectral properties of the optical density (or absorbance) which is defined as $\log_{10}(1/\text{transmittance})$. Results for the optical absorbance shown as the optical density versus wavelength in the ultraviolet (UV)-visible range (200–700 nm) for C_{60} and C_{70} in hexane[79] are depicted in Figs. 22(a) and 22(b), respectively. The strong absorption bands in the
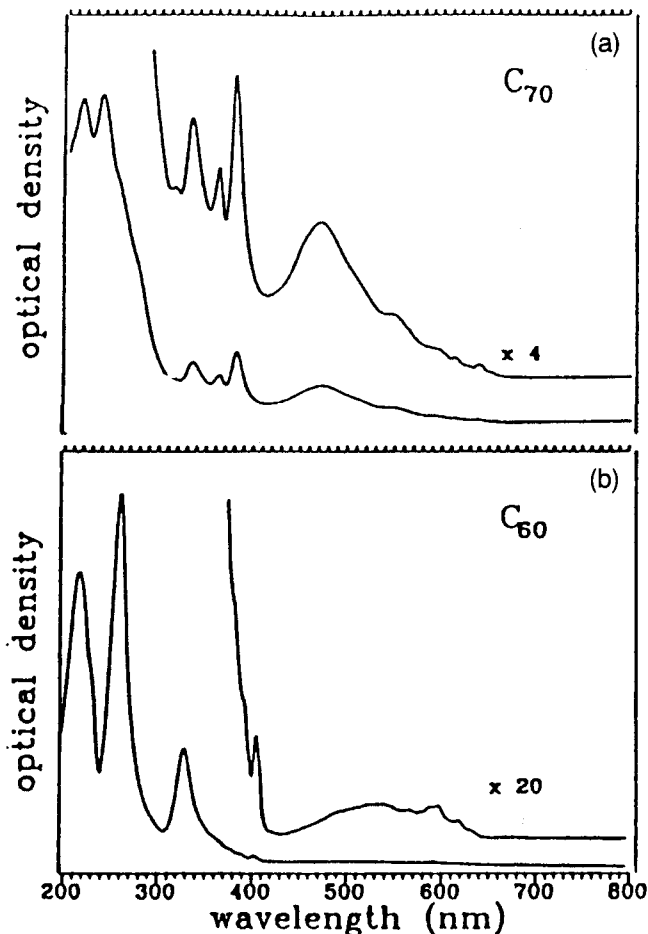

FIG. 22. Optical density versus wavelength for (a) C_{60} and (b) C_{70} in hexane solutions, and the characteristic absorption bands are identified.[79]

TABLE III. Physical constants for M_3C_{60} (M = K, Rb).

Quantity	K_3C_{60}	Rb_3C_{60}	Ref.
fcc lattice constant (Å)	14.253	14.436	50
$(-d \ln a/dP)$ (GPa^{-1})	1.20×10^{-2}	1.52×10^{-2}	131
Bulk modulus (GPa)	28	22	108
Cohesive energy (eV)	24.2	⋯	108
Heat of formation (eV)	4.9	⋯	108
Density of states [states/(eV/C_{60})]	25	35	164
Electron effective mass (m_e)	1.3	⋯	108
Hole effective mass (m_e)	1.5, 3.4	⋯	108

figure (below ~400 nm in wavelength or above ~2.9 eV in energy) are identified with electric dipole-allowed transitions between occupied (bonding) and empty (antibonding) molecular orbitals denoted in Fig. 21 by either the $h_u \rightarrow t_{1g}$ (or f_{1g}) transition or the $h_g \rightarrow t_{1u}$ (or f_{1u}) transition. At longer wavelengths $490 < \lambda < 640$ nm (or $1.9 < E < 2.5$ eV), weak absorption takes place and is associated with electric dipole-forbidden transitions between the one-electron HOMO level with H_u symmetry and the one-electron LUMO level with F_{1u} (T_{1u}) symmetry (see Sec. VIII). Using many-electron molecular states,[151] the fully occupied HOMO ground state is identified with a single S_0 state (having quantum numbers $L = 0$, $S = 0$, and $J = 0$) with A_g symmetry which we also write as ^1A_g.

Since the many-electron molecular approach is expected to be more successful for describing the optical properties of C_{60}, especially for the low photon energy range where the optical transitions are parity forbidden, we review briefly the formation of optically excited states near the HOMO–LUMO gap using this formalism.

2076

J. Mater. Res., Vol. 8, No. 8, Aug 1993

As stated above, the lowest parity-forbidden optical transition is from the H_u HOMO level to the F_{1u} (T_{1u}) LUMO level, which we write in terms of the configurational transition $h_u^{10} \rightarrow h_u^9 f_{1u}^1$. (In this notation we use capital letters to denote the irreducible representation of the symmetry group and lower case letters to denote electronic configurations.) The ground state is a filled H_u multiplet that can accommodate 10 electrons. The ground state has A_g symmetry which is denoted by ^1A_g. In the excited state, we have one electron (f_{1u}) and one hole (h_u^9), each with spin 1/2, so that the interacting electron and hole can either form a singlet S_i state $(S = 0)$ or a triplet T_i state $(S = 1)$. Since the perturbation Hamiltonian for the electric dipole matrix element for optical transitions, $\mathcal{H}'_{em} = (\mathbf{p} \cdot \mathbf{A})/(mc)$, does not depend on spin, there is a strong spin selection rule $(\Delta S = 0)$ for optical electric dipole transitions. This strong selection rule arises from the very weak spin-orbit interaction for carbon, which has a low atomic number $(Z = 6)$. Having satisfied the spin selection rule, the orbital selection rule must now be considered. To satisfy the electric dipole selection rule, appropriate odd-parity vibrational modes must be admixed with the initial and (or) final electronic states for the optical transition (see Fig. 23). Thus, the weak absorption below 2.9 eV involves optical transitions between appropriate vibronic levels. In group theoretical language, the symmetries for the various states in the $h_u^9 f_{1u}^1$ excitonic state configuration are found by taking the direct product of $H_u \otimes F_{1u}$ for the hole and the electron which requires the final excited state to have one of the following symmetries: F_{1g}, F_{2g}, G_g, or H_g. Each of these four excited state configurations must be combined with appropriate odd-parity vibrations (see Sec. VI) to satisfy the electric dipole selection rule and allow coupling to the A_g ground state. The direct product of the initial (vibronic) state with the electric dipole operator F_{1u} yields the symmetry types contained in the final (vibronic) state. Optical transitions between the HOMO and LUMO levels can thus occur through the excitation of a vibronic state with the appropriate odd-parity vibrational mode.[165–168] A schematic diagram of the vibronic manifolds associated with the various levels constituting the $h_u^9 f_{1u}^1$ excitonic configuration is presented in Fig. 23.[169]

Using these molecular states (see Fig. 23), the weak absorption observed between 490 and 640 nm for C_{60} in solution [Fig. 22(a)][79] is assigned to transitions between the singlet ground state S_0 (also denoted as ^1A_g) and the lowest excited singlet state S_1 (denoted in Fig. 23 as $^1F_{2g}$ and associated with the f_{1u} orbital and activated by vibronic coupling as described above and illustrated in Fig. 23). From the long wavelength limit (~ 640 nm) of this weak optical absorption in solution, the energy of the S_1 excitonic state rela-
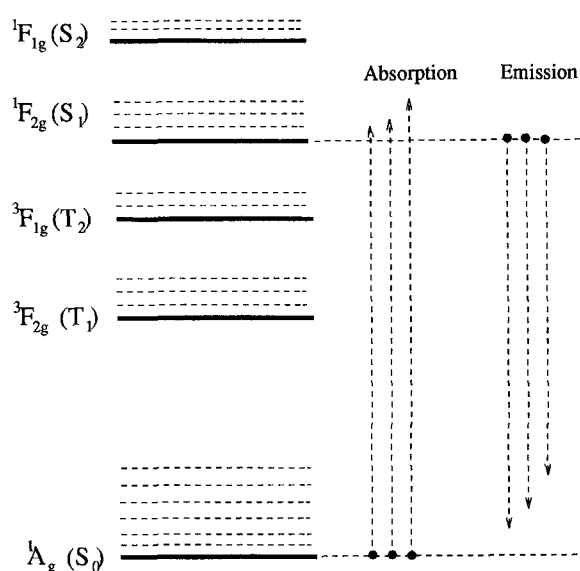

FIG. 23. Schematic diagram of the excitonic vibronic transitions in C_{60}^0 between an h_u^{10} ground state with ^1A_g symmetry and an $h_u^9 f_{1u}^1$ excited state on absorption and on emission.[169] The solid horizontal lines refer to singlet or triplet excitonic levels and the dashed horizontal lines to their related vibronic levels. The higher-lying excitonic G_g and H_g manifolds are not shown.

tive to the HOMO ground state can be estimated to be ~ 1.9 eV. Molecular orbital calculations for C_{60} have predicted optical transitions between the various π-derived levels in the UV-visible range,[152,170–172] and values calculated for the HOMO–LUMO gap (E_{HL}) lie in the range $E_{HL} = 1.8–1.9$ eV, in agreement with solution spectra.[79]

For C_{70}, molecular orbital calculations[152] reveal a large number of closely spaced orbitals both above and below the HOMO–LUMO gap, $E_{HL} = 1.65$ eV.[152] The large number of orbitals makes it difficult to assign particular groups of transitions to structures observed in the solution spectra of C_{70}. UV-visible solution spectra for higher fullerenes (C_n; $n = 76, 78, 82, 84, 90,$ and 96) have also been reported,[23,26,84] and molar extinction coefficients for C_{60} and C_{70} have been obtained at several wavelengths.[76] The availability of reliable molar extinction data is essential for *quantitative* high performance liquid chromatography (HPLC) analysis of C_{60}/C_{70} mixtures.

Further insight into the electronic structure is provided by pulsed laser studies of C_{60} and C_{70}. Such time-resolved studies of fullerenes in solution have been used to probe the photodynamics of the optical excitation/luminescence spectra. The importance of these dynamic studies is to show that photoexcitation in the long-wavelength portion of the UV-visible spectrum leads to the promotion of C_{60} from the singlet S_0 ground state (^1A_g) into a singlet S_1 excited state, which

decays quickly with a nearly 100% efficiency[173,174] via an intersystem crossing to the lowest excited triplet state T_1. As shown in Fig. 23, the excited triplet T_1 state (also denoted in Fig. 23 as $^3F_{2g}$) has the same orbital quantum numbers as the excited S_1 state. This rapid singlet-triplet decay (~33 ps[174]) is fostered by the overlap in energy between the vibronic manifold of electronic states associated with the lowest singlet S_1 state and the corresponding vibronic manifold for the triplet T_1 state.

Once in the T_1 triplet excitonic manifold, a very rapid transition to the lowest level of the T_1 triplet manifold occurs. It is significant that the lowest energy level of the triplet manifold has been found experimentally to lie about 0.4 eV lower in energy than the lowest energy level of the singlet S_1 manifold.[174] Also of significance is the long life of the lowest triplet state ($>2.8 \times 10^{-4}$ s) relative to the lowest singlet state (1.2 ns) in the room temperature solution absorption spectra.[175] The value of the T_1 triplet lifetime varies widely from one study to another, presumably because of the great sensitivity of this lifetime to the presence of oxygen, which has been shown for different solutions to reduce the triplet lifetime from <40 μs to ~300 ps.[174,176] Despite the difference in the values of the reported triplet T_1 lifetimes, it is clear that in the absence of oxygen, the triplet T_1 lifetime is much longer than the singlet S_1 lifetime, so that a metastable T_1 state can be established. The significant population of a metastable T_1 level that can be achieved in C_{60} by optical pumping leads to interesting nonlinear optical properties as discussed below.

The emission spectra for fullerenes have been especially interesting because the emission band generally occurs at lower energies (by ~0.4 eV) than the absorption band. We first discuss results for solution spectra, followed by spectra in the solid state. Optical emission, supposedly fluorescence, has been observed from the S_1 level for C_{60} in methylcyclohexane at $T = 77$ K (where the frozen solvent forms an organic glass). Here the peak (maximum emission) is at ~740 nm (~1.7 eV), and the emission spectra exhibit clear vibronic structure.[67] For C_{60}, the occupation of the triplet T_1 state has been shown to be quenched with nearly 100% efficiency by dioxygen, leading to a very short lifetime for C_{60} in the excited T_1 state and a fast nonradiative relaxation to the ground state in the presence of oxygen.[132,174,176] However, in the organic glass solvent, the effect of oxygen on the triplet state lifetime is less important because of the lower oxygen diffusion and reduced collision rate. Using photoacoustic calorimetry,[174] the triplet energy $E_T = 36$ kcal/mole or 1.56 eV has been obtained in C_{60}. The small singlet-triplet splitting ($\Delta E_{S,T} \sim 9$ kcal/mole or 0.4 eV) is consistent with the relatively large diameter of a C_{60} molecule. For C_{70} in toluene/10% poly(α-methylstyrene), phosphorescence at $T = 300$ K with a

lifetime $\simeq53$ ms from the T_1 level has been reported at 810 nm, suggesting that $E_T = 1.53$ eV for C_{70}.[177] Using pico- and nanosecond flash photolysis, the excited-state optical properties of C_{60} in toluene have been studied to determine the S_1-S_n[175] and T_1-T_n[175,176] absorption spectra. For studying the $T_1 \rightarrow T_n$ spectrum, the intersystem crossing (discussed above) is used to populate the T_1 level. The $T_1 \rightarrow T_n$ absorption has been reported to be stronger than the $S_0 \rightarrow S_n$ absorption, and this could provide a mechanism[178] to account for the observed nonlinear absorption leading to "optical limiting" of transmitted, transient, visible light in both C_{60} and C_{70} (7 ns pulses at 532 nm) (see Sec. XV).

The luminescence spectrum for a solid C_{60} film on a quartz substrate is presented in Fig. 24 in comparison with the absorption spectra shown for the same spot on the same film.[167] The results show a luminescence band between 1.4 and 1.75 eV. The two peaks in the luminescence spectra in Fig. 24 are at 1.5 and 1.7 eV, and are identified with an emission from vibronic states associated with the S_1 band, consistent with the solution luminescence spectra. The emission spectra in solid C_{60} are closely identified with the corresponding solution spectra because of the similarities of the two spectra regarding spectral width and shape. The broadening of the emission spectra in solid C_{60} is attributed to the dispersion of the electronic levels in the solid state. The 46 vibrational levels of C_{60} consist of a band of low frequency modes ($\omega_{ph} < 800$ cm^{-1}) associated with predominantly radial displacements and a band of high frequency modes ($\omega_{ph} > 800$ cm^{-1}) associated with

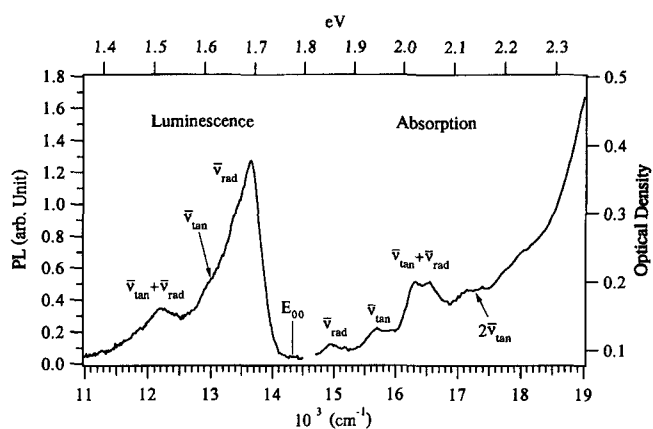FIG. 24. Experimental optical emission ($1.35 < \hbar\omega < 1.80$ eV) and optical absorption ($\hbar\omega > 1.7$ eV) spectra associated with the excited singlet S_1 state $h_u^9 f_{1u}$ and the singlet S_0 ground state h_u^{10} of C_{60}. The data were taken at $T = 80$ K on the same spot of a thin film (thickness $d \sim 600$ Å) deposited on a Suprasil substrate. The emission is the luminescence from the S_1 excited state to vibronic states associated with S_0, whereas the absorption involves transitions from S_0 to vibronic states in the S_1 manifold (see Fig. 23). ν_{rad} and ν_{tan} are characteristic radial and tangential intramolecular mode frequencies. E_{00} denotes the excitonic S_1 level.

predominantly tangential displacements on the C_{60} balls (see Sec. VI). The absorption spectra involve vibronic final states associated with the S_1 singlet manifold, while the emission spectra involve vibronic final states associated with the S_0 singlet manifold. This gives rise to similar absorption and emission spectra but shifted from each other by $\sim 2\omega_{ph}$, where ω_{ph} denote the odd parity vibrations that satisfy the selection rules between the vibronic states discussed above. No phosphorescent emission from the triplet (T_1) vibronic manifold has been observed in either the solution or solid phase emission spectra, presumably because of efficient nonradiative relaxation from the metastable T_1 state to the S_0 ground state.

Further evidence for the existence of a metastable T_1 excited state comes from observations of a downshifted A_{1g} Raman-active pentagonal pinch mode at 1458 cm^{-1} identified as from a C_{60} molecule in the excited T_1 state[97] (see Sec. VI). The quenching of the T_1 state by the presence of oxygen can be explained by spin-orbit coupling induced by the dioxygen (which has a triplet ground state), allowing a rapid nonradiative decay of the T_1 excited state for C_{60} to its ground state[132] coupled to the excitation of dioxygen to the excited singlet state.

To date, most of the optical studies on pristine fullerene solids have been carried out in transmission on thin solid films deposited on various substrates (such as quartz, Si, and KBr). As mentioned above, the UV-visible transmission spectra for C_{60} and C_{70} solid films are observed to be remarkably similar to the respective solution spectra, thus providing further evidence for the molecular nature of fullerene solids. This is shown, for example, in Fig. 25 in which the transmittance for solid C_{60} is compared with that for C_{60} dissolved in decalin.[28]

The optical properties of solid C_{60} and C_{70} have been studied over a wide frequency range using the variable angle spectroscopic ellipsometry (VASE) technique.[28,179] From the VASE measurements, the complex refractive index, $\tilde{n}(\omega) = n(\omega) + ik(\omega)$, is determined, which is related to the complex optical dielectric function $\epsilon(\omega) = \epsilon_1(\omega) + i\epsilon_2(\omega) = \tilde{n}^2(\omega)$. In Fig. 26 the results are shown for $\epsilon_1(\omega)$ and $\epsilon_2(\omega)$ obtained from VASE and transmission-FTIR studies on thin solid films of C_{60} at $T = 300$ K.[180] The strong, sharp structure at low energy is identified with infrared-active optic phonons and at higher energies the structure is due to electronic transitions, as discussed below.

The optical functions $n(\omega)$ and $k(\omega)$ obtained from VASE studies for C_{60}[28] and C_{70}[179] are shown in Figs. 27(a) and 27(b), together with data on other solid forms of carbon (diamond, graphite, and glassy carbon). Graphite and glassy carbon are semimetals, in contrast to the insulating behavior of the other forms of carbon in the figure. The various materials thus exhibit a noticeably different low energy response arising from
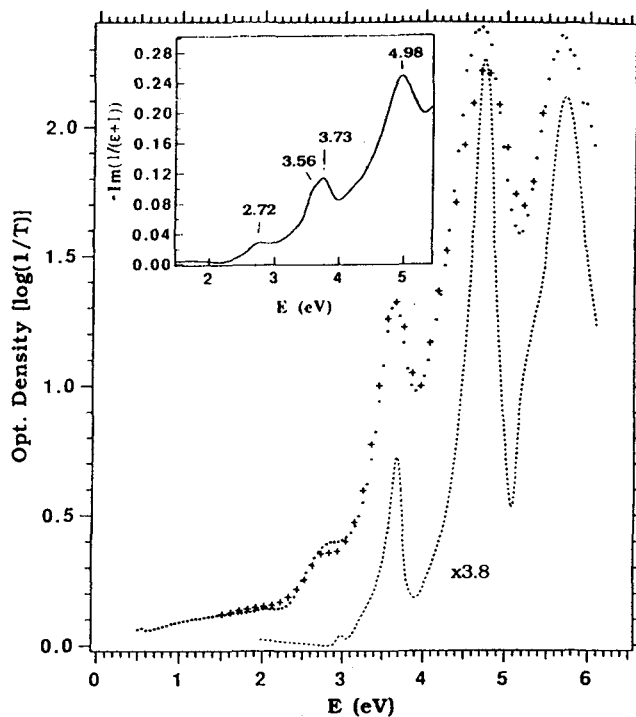

FIG. 25. Optical density of solid C_{60} on Suprasil derived from ellipsometry measurements (+) and that measured directly for C_{60} on Suprasil by normal incidence transmission spectroscopy (•). For comparison, the solution spectrum for C_{60} dissolved in decalin (−) is shown below the spectra for the films. The inset is a plot of $-\ln[(1 + \epsilon)]^{-1}$ vs E for comparison of the peaks in the optical data with the peaks in the high resolution electron energy loss spectra (HREELS).[28]

large differences in their free carrier contributions to the optical constants. Above ~ 2 eV, interesting differences in the structure in the absorptive part of the complex refractive index $k(\omega)$ are observed for the various forms of solid carbon, and these structures are identified with transitions between bonding and antibonding π-derived electronic states. The differences in the optical spectra for the various forms of carbon arise from the large differences in the crystal structure between these forms of carbon, and these differences in structure affect the nature of the C(2s) and C(2p) orbital hybridization. From the VASE studies of C_{60} and C_{70}, similar values for the static dielectric function $\epsilon_1(0) = [n(0)]^2$ have been obtained: $\epsilon_1(0) = 3.61$ (for C_{60})[28] and $\epsilon_1(0) = 3.94$ (for C_{70}).[179] For the case of C_{60}, this value for $\epsilon_1(0)$ can be compared with the value $\epsilon_1(0) = 4.4 \pm 0.2$ obtained from capacitance measurements.[181] Fringe structure in the transmission data of C_{60} solid films has been used[67] to obtain a value $\epsilon_1(0) = 4.1$ in better agreement with the capacitance measurements.[181]

Near-normal incidence, transmission/reflection studies on C_{60} and M_6C_{60} (M = K, Rb, and Cs)[67] have been carried out in the range 0.5–6 eV to determine
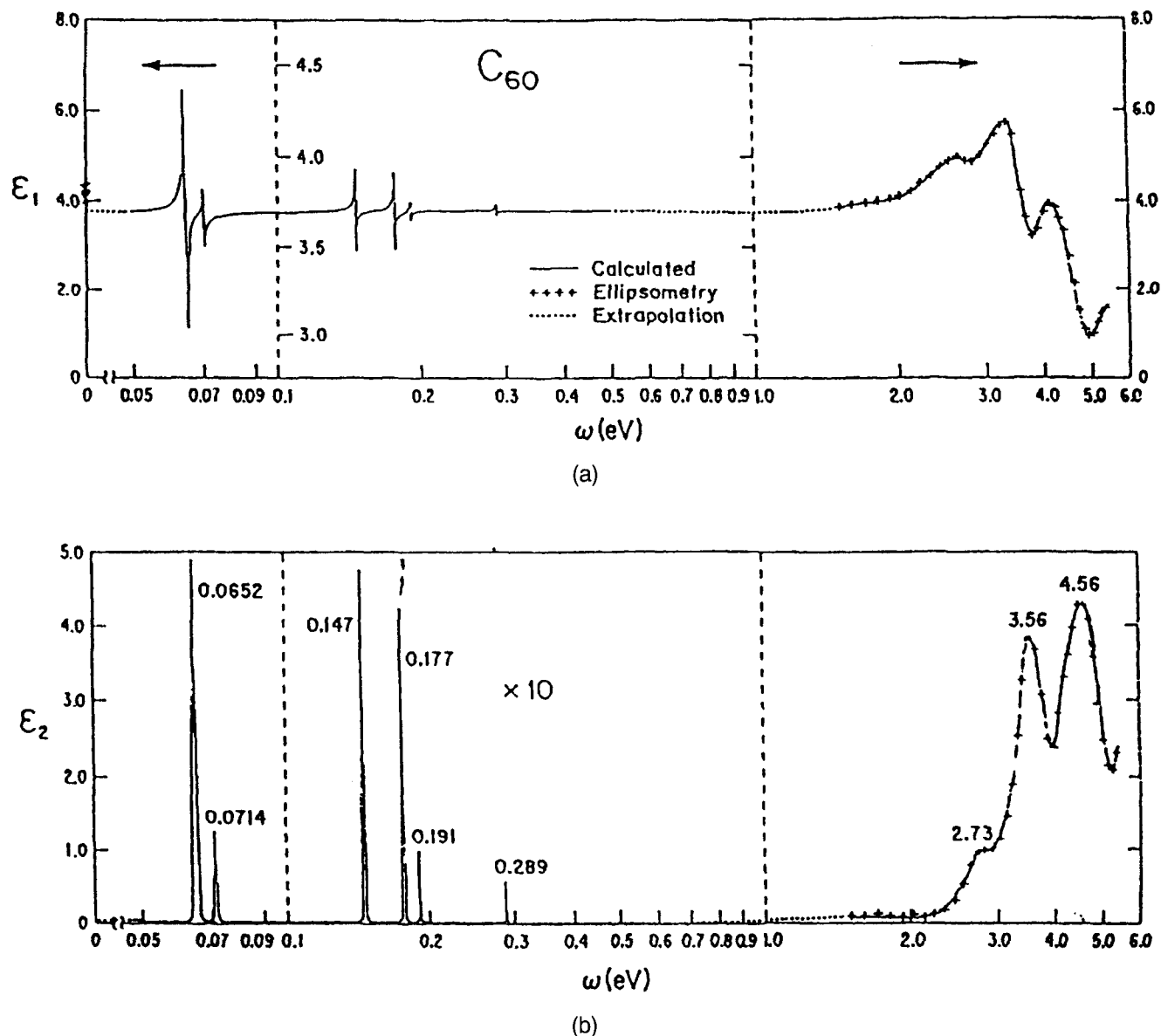
FIG. 26. Optical dielectric constants (a) $\epsilon_1(\omega)$ and (b) $\epsilon_2(\omega)$ from variable angle spectroscopic ellipsometry (VASE) and Fourier transform infrared (FTIR) spectroscopy for C_{60}.[180]

the optical dielectric function $\epsilon(\omega)$.[28] For C_{60}, these studies[67] have assigned absorption structure to transitions between specific, narrow (0.3–0.5 eV) energy bands, using a band model to describe the electronic states. Using a band model, good agreement was found between the calculated energy band spacing[152,170] and the experimental peak positions in the absorptive part of $\epsilon(\omega)$, namely $\epsilon_2(\omega)$, for energy bands within ~1 eV of the solid-state-derived HOMO–LUMO gap. Although electric dipole transitions are forbidden between these bands at the X-point, the optical matrix element increases as k^2, where k is the radial wave vector measured relative to the X-point. Thus, on the basis of a band picture, some absorption between the HOMO- and LUMO-

derived bands should be observed.[182] Furthermore, as discussed above, vibronic coupling to the LUMO states also provides a mechanism within a molecular model by which optical absorption across the HOMO–LUMO gap can be observed. By writing the film absorbance as $A = 1 - (R + T)$, where R and T are the fractional normal-incidence reflection and transmission intensities, a threshold for optical absorption at 300 K in a C_{60} film (on Suprasil or fused silica) was detected at 1.7 eV.[67] This value can be compared to the value of 1.79 eV obtained from optical transmission at $T = 20$ K from a C_{60} film (on CaF_2)[183] and the value 1.7 eV in Fig. 24.[167] Both of these experimental values are in reasonable agreement with theoretical predictions for the direct gap
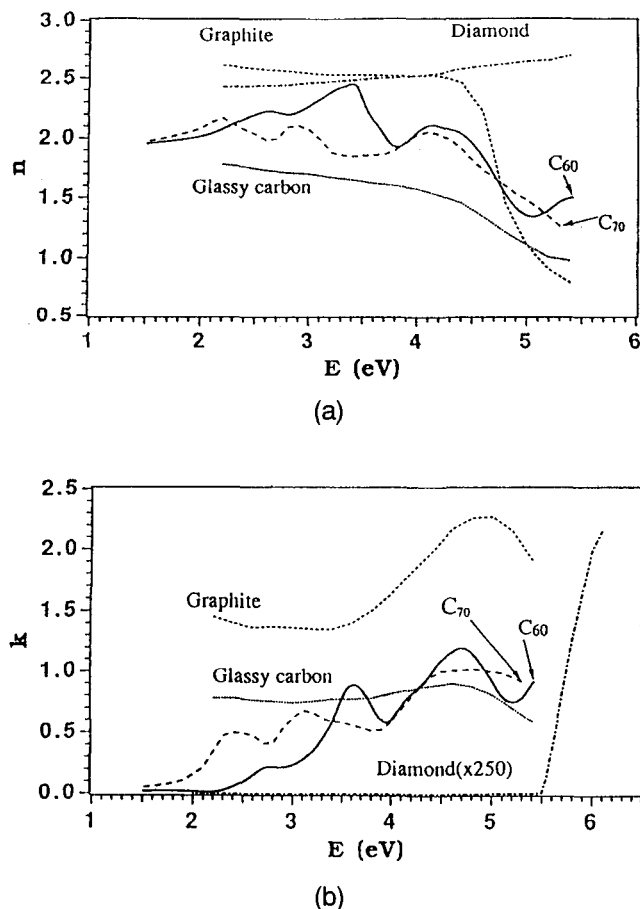
FIG. 27. Variable angle ellipsometric measurements of the optical constants $n(\omega)$ (a) and $k(\omega)$ (b) in the 1–5 eV range for C_{60} (Ref. 28) and C_{70} (Ref. 179) with comparisons made to other carbon-based materials.

of 1.4 eV[170] and 1.5 eV,[152] after the frequency shifts associated with the vibronic levels are taken into account.

For alkali-metal-saturated C_{60} solid films (e.g., M_6C_{60}: M = K, Rb, and Cs), similar transmission and reflection spectra are obtained, largely insensitive to the dopant or intercalate species (M).[67] These results give strong evidence for only weak hybridization between M and C_{60} states. The optical spectra are thus consistent with a molecular picture in which complete charge transfer of the alkali metal s-electrons takes place to fill a lower lying, sixfold degenerate C_{60} band (F_{1u} symmetry). When the effect of spin-orbit interaction is considered for the M_6C_{60} compounds, the sixfold F_{1u} level splits into a twofold $f_{1u}^{1/2}$ (double group representation Γ_6^-) and a fourfold $f_{1u}^{3/2}$ (double group representation Γ_8^-) level. However, this splitting is expected to be small (see Table I). The narrow spectral features in M_6C_{60} observed in $\epsilon_2(\omega)$ for $\omega < 3$ eV have been assigned to transitions between narrow energy bands or broadened molecular states whose spacing was found to be in good agreement with theory.[162,170] No

absorption threshold was detected down to 0.5 eV in the M_6C_{60} materials, establishing an experimental upper-bound for the energy gap between the F_{1u}-derived and F_{1g}-derived states.

Using a pulsed Nd:YAG laser, nonlinear optical behavior has been observed in solid C_{60} films at $T = 300$ K.[184,185] Using time-resolved four-wave mixing,[184] a fast (<35 ps) nonlinear response (including third- and fifth-order contributions) was observed leading to a substantial third-order optical susceptibility $\chi_{xxxx}(3) = 7 \times 10^{-12}$ esu, 60 times greater than that of benzene. The origin of the optical nonlinearity is probably connected to the high efficiency (~100%) in transferring electrons from the excited singlet state manifold S_1 to the T_1 triplet excited states and also the larger optical matrix elements for triplet-triplet transitions (which are important for high power levels for the incident light) relative to the singlet-singlet transitions that dominate the optical absorption spectrum at low light power levels. In addition, highly delocalized π-conjugated electron systems are known to exhibit strong nonlinear behavior.[186]

X. ELECTRICAL AND THERMAL TRANSPORT

Because of the high resistivity of undoped C_{60}, the doping of C_{60} with alkali metals creates carriers at the Fermi level and decreases the electrical resistivity ρ of C_{60} by several orders of magnitude. As x in M_xC_{60} (M = K, Rb) increases, the resistivity ρ approaches a minimum at $x = 3.0 \pm 0.05$,[187,188] corresponding to a half-filled F_{1u}-derived (T_{1u}-derived) conduction band. Then, upon further increase in x from 3 to 6, ρ again increases, as is shown in Fig. 28 for K_3C_{60}.[188] It should be noted that stable M_xC_{60} compounds (for M =K, Rb) occur only for $x = 0, 3, 4,$ and 6 (under some circumstances M_1C_{60} and M_2C_{60} compounds are stable) (see Sec. V.C). The compounds corresponding to filled molecular levels (C_{60} and M_6C_{60}) are the most stable structurally and exhibit maxima in the resistivity. Furthermore, even at the minimum resistivity in M_xC_{60}, the value of ρ found for K_3C_{60} (2.5 × 10^{-3} Ω-cm) is high, typical of a high resistivity metal.[188] Furthermore, no structure is observed (Fig. 28) in the $\rho(x)$ data near $x = 4$, indicating that K_4C_{60} may not be a metallic phase or that no K_4C_{60} was formed under the experimental conditions of this experiment.[188]

Studies of the temperature dependence of the resistivity of polycrystalline M_xC_{60} samples in the normal state show that conduction is by a thermally activated hopping process except for a small range of x near 3 where the conduction is metallic.[49,187] The magnitude of the arrows in Fig. 28, corresponding to the magnitude of the activation energy E_a, indicates that E_a increases as x deviates further and further from
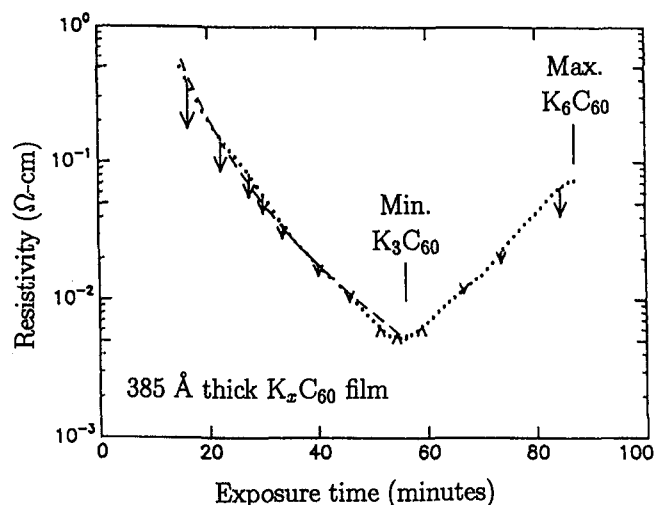
FIG. 28. Dependence of the resistivity of a K_xC_{60} film on exposure time to K vapor at ambient temperature near 74 °C. The end-point stoichiometry was determined for this particular sample; the stoichiometry at the minimum was determined from other similarly prepared samples. The lengths of the arrows show schematically changes in the resistivity of a similar sample as it was heated from 60° to 134 °C. The dashed curve is a model fit.[188]

FIG. 29. Temperature dependence of the resistivity ρ of single crystal K_3C_{60} showing a nearly linear increase in ρ above T_c.[83]

the resistivity minimum at $x = 3$, and E_a has, for example, a magnitude of 0.12 eV for $x = 1$.[188] In the metallic regime, results for $\rho(T)$ for a superconducting single crystal K_3C_{60} sample (see Fig. 29)[83] show a linear T dependence of $\rho(T)$ above T_c,[49,83] although the linear T dependence is much weaker than that for the high T_c cuprates.[189] The single crystal studies of the temperature dependence of $\rho(T)$[49,83] show no more than a factor of two increase in resistivity between T_c and 300 K, although microwave determinations of $\rho(T)$ on pressed powder samples[190] show a lower value of $\rho(T_c^+) \sim 0.5 \times 10^{-3}$ Ω-cm, a different functional form for $\rho(T)$ and a much larger difference between $\rho(T_c^+)$ and $\rho(300 \text{ K})$ in comparison with the static transport measurements. The reason for this difference in behavior is not understood at present.

Also, a number of studies have shown that the temperature dependence of the resistivity $\rho(T)$ is strongly dependent on whether the sample is a single crystal or a film.[49,83,191] Film samples tend to exhibit a negative temperature coefficient of $\rho(T)$ just above T_c while single crystal samples exhibit a positive $\partial\rho(T)/\partial T$ just above T_c (see Fig. 29). The observed temperature dependence of the resistivity of films of M_xC_{60} (for $0 < x \leq 6$) has been interpreted by some authors in terms of a granular conductor with grain sizes in the 60–80 Å range.[192] This granularity strongly affects the superconductivity properties of the M_3C_{60} films, as well as their properties in the normal state.[192] Other authors[193] have attributed the negative slope $\partial\rho/\partial T$ of $\rho(T)$ in M_3C_{60} films to weak localization and superconducting fluctuations near
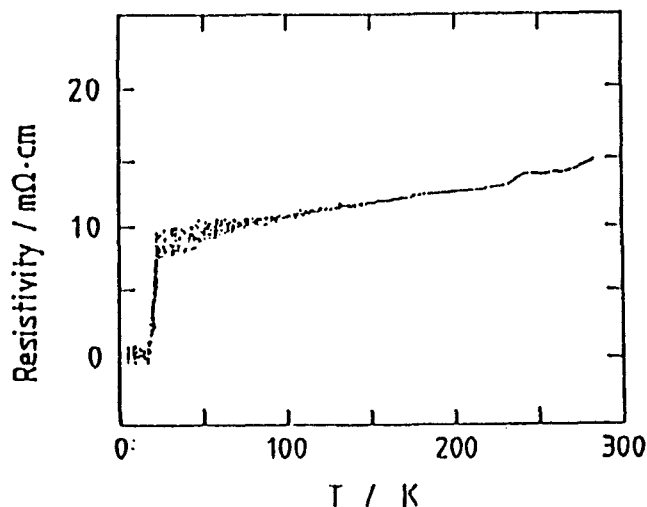
T_c. In general, transport measurements on M_xC_{60} films by different groups are likely to show differences due to small deviations in average stoichiometry and sample homogeneity, leading to differences in the coexisting phases (see Fig. 12).

Temperature-dependent Hall effect measurements have also been carried out in the temperature range 30 to 260 K on a K_3C_{60} thin film.[192] For three electrons per C_{60}, the expected Hall coefficient R_H based on a one carrier model would be about one order of magnitude smaller than the experimentally observed value.[192] The small value of the observed Hall coefficient suggests multiple carrier types including both electrons and holes. This interpretation is corroborated by the observed sign change in R_H from negative below 220 K to positive above 220 K. Multiple carrier types are consistent with the Fermi surface calculations by Erwin and Pederson[162] and by Oshiyama et al.[108] which also suggest both electron and hole orbits on the Fermi surface.

The high electrical resistivity and the magnitude of the optical bandgap of C_{60} can be reduced by the application of high pressure, with decreases in resistivity of about one order of magnitude observed per 10 GPa pressure.[194] However, at a pressure of ~20 GPa, an irreversible phase transition to a more insulating phase has been reported.[194] As the intermolecular C–C distance decreases upon application of pressure and becomes comparable to the intramolecular C–C distance, an electronic transition might be expected to occur.

The temperature dependence of the thermopower $S(T)$ of single crystal K_3C_{60} and Rb_3C_{60} (prepared from CS_2 solution) has been measured from 300 K down to low T.[195] The results show that $S(T)$ is negative (consistent with conduction by electrons) and nearly

linear in T. Using the relation,

$$S(T) = \frac{\pi^2 k_B^2 T}{3eE_F}\left[\frac{\partial \ln \sigma(E)}{\partial \ln E}\right]_{E=E_F}, \qquad (5)$$

a value of the Fermi energy was obtained, $E_F = 0.20 \pm 0.02$ eV for K_3C_{60}, from which the authors concluded that the ratio of the density of states in Rb_3C_{60} to that in K_3C_{60},

$$\frac{N^{K_3C_{60}}(E_F)}{N^{Rb_3C_{60}}(E_F)} = \frac{E_F^{K_3C_{60}}}{E_F^{Rb_3C_{60}}} \sim 1.5\text{--}1.8, \qquad (6)$$

is in good agreement with their measured ratio of the corresponding superconducting transition temperatures of 1.55.[195] These authors further found a small deviation from linear behavior in their $S(T)$ measurements which they attributed to phonon drag effects.

Thermal conductivity measurements from 30 K to 300 K on single crystal C_{60} by Yu et al.[66] show that the thermal conductivity $\kappa(T)$ is dominated by lattice contributions (see Sec. VII. C). No thermal conductivity measurements are presently available regarding the electronic contribution to the thermal conductivity for any fullerene or fullerene-derived material.

XI. NMR, EPR, AND ELECTRON SPECTROSCOPIES

A variety of spectroscopies and surface science techniques have contributed importantly to our understanding of fullerenes. Thus far, the most widely used techniques have been nuclear magnetic resonance (NMR), electron paramagnetic resonance (EPR), scanning tunneling spectroscopy (STM), and photoemission spectroscopies.

A. Nuclear magnetic resonance

NMR was one of the earliest spectroscopies used to show conclusively that the icosahedral structure for the C_{60} molecule was correct. The 60 carbon atoms in C_{60} are now known to be located at the vertices of a regular truncated icosahedron where every site is equivalent to every other site (see Fig. 1), consistent with a single sharp line in the NMR spectrum.[13,14] In contrast, C_{70} shows five lines, indicative of the five different site symmetries on the C_{70} rugby ball structure.[13] NMR has also been useful for identifying the C_{76} molecule with a chiral structure to explain the complicated NMR spectrum with 19 lines.[196] The temperature dependence of the NMR line in C_{60} gives information about the molecular dynamics of the molecules. At high temperatures, the molecules tend to rotate freely, giving rise to very narrow NMR linewidths through the motional narrowing effect.[197] As T decreases, the molecular rotations become hindered (see Sec. VII), and the NMR lines broaden. Of particular interest is the anisotropy of the NMR line in C_{70} that indicates rapid

motion about the high symmetry axis of the molecule.[15] Measurement of the temperature dependence of the spin-lattice relaxation time provides a sensitive probe of the lattice, and this technique has been used to monitor the first-order structural phase transition occurring in C_{60} near 255 K (see Sec. VII. A).[95,198] By determining the magnetic dipolar coupling in the NMR experiment, the C–C bond distances have been measured.[78] NMR experiments on alkali-metal-doped C_{60} show that K_3C_{60} forms a stable phase, while $K_{1.5}C_{60}$ and K_2C_{60} do not.[164] Also, the observation of a Knight shift in K_3C_{60} confirms the metallic nature of this compound.[164]

B. Electron paramagnetic resonance

Electron paramagnetic resonance (EPR) and electron spin resonance techniques have also yielded valuable information about the structure and electronic properties of fullerenes. Particularly noteworthy are the EPR experiments on the endohedrally doped fullerenes discussed in Sec. V. C.[16] For example, the EPR spectrum of La @ C_{82} shows the characteristic 8-line hyperfine spectrum for the ^{139}La nucleus with spin 7/2. The sharp lines in this spectrum suggest a weak coupling between the La nucleus and the s-electrons on the C_{82} fullerene, and indicate that the La is in a 3+ ionization state; the EPR results also support the endohedral location of the La^{3+} ion inside the C_{82} shell. Both NMR and EPR techniques are expected to provide many important insights into the structure and properties of fullerenes and variously doped fullerenes.

C. Scanning tunneling microscopy

Scanning tunneling microscopy (STM) has provided an excellent technique for studying the epitaxial growth of C_{60} films on various substrates, for identifying the surface crystal structures, crystalline domain sizes, and the common defect structures that occur.[199] The STM tip has also been used to manipulate individual C_{60} molecules on the surface. The imaging of individual carbon atoms on the C_{60} balls has been difficult to achieve because of the rotational degrees of freedom of fullerenes near 300 K; such imaging may be possible at low temperatures. In addition STM has been used to carry out tunneling experiments on K_3C_{60} and Rb_3C_{60} to measure the temperature dependence of the superconducting energy gap,[200,201] and these results are summarized in Sec. XII.

D. Photoemission

Photoemission and inverse photoemission experiments have been especially useful[161] in providing information on the density of states within a few eV of the Fermi level for both undoped and doped fullerenes. Since photoemission experiments are highly sensitive

to the first two or three nanometers of material near the surface, the intercalation of the fullerenes is normally done in the measurement apparatus, since cleavage techniques, which were successfully used in ultraviolet photoemission studies on graphite intercalation compounds, cannot be used for intercalated fullerene samples. This difficulty with sample preparation introduces uncertainties in specifying the exact stoichiometry and homogeneity of the near surface layers (<20 Å) that are probed in photoemission. Also of concern is, on the one hand, verification of the similarity between the near surface layers and the bulk material with regard to structure and composition, and, on the other hand, the formation of spatially separated phases (such as K_3C_{60} and K_6C_{60}), upon addition of K, that are inhomogeneously distributed throughout the sample (see Fig. 12).

Typical photoemission spectra (PES) ($E < E_F$, where E_F is the Fermi energy) and inverse photoemission[202] spectra (IPES) ($E > E_F$) are shown in Fig. 30 for C_{60} and K_xC_{60} ($0 \leqslant x \leqslant 6$),[44] where the intensity maxima correspond to peaks in the density of states on the basis of a one-electron picture and a constant matrix element approximation, after corrections are made for the screening or correlation energy (~2 eV) of the Hubbard model. In the photoemission experiments, the density of states for the occupied levels is probed, while in the inverse photoemission experiments the density of unoccupied states is probed. Because of these screening and correlation effects, it may be difficult to obtain quantitative information about the magnitude of the HOMO–LUMO gap in fullerenes by the photoemission technique. Photoemission data do provide, however, convincing evidence for charge transfer and for band filling as x in K_xC_{60} increases. Referring to Fig. 30, we can see the density of states peak, associated with the F_{1u}-derived band just above the Fermi level E_F in the C_{60} trace. As K is added to C_{60}, this peak moves closer to E_F, as some K_3C_{60} phase is introduced. Upon further addition of potassium, the F_{1u}-related peak crosses the Fermi level and eventually for $5.8 \leqslant x \leqslant 6.0$, the F_{1u}-derived peak falls below E_F, indicating complete filling of the F_{1u}-derived level; the data for this composition further show a small bandgap to the next higher lying F_{1g}-derived level (see Fig. 21). The width of the peaks in the photoemission spectra, such as in Fig. 30, has been identified with the bandwidth of the HOMO and LUMO-derived bands, again in good agreement with band calculations.[152] While band calculations of the density of states provide a good fit to the observed photoemission and inverse photoemission spectra,[152] a more molecular approach to the electronic structure of crystalline C_{60} and its related intercalation compounds may yield an equally good fit to the experimental
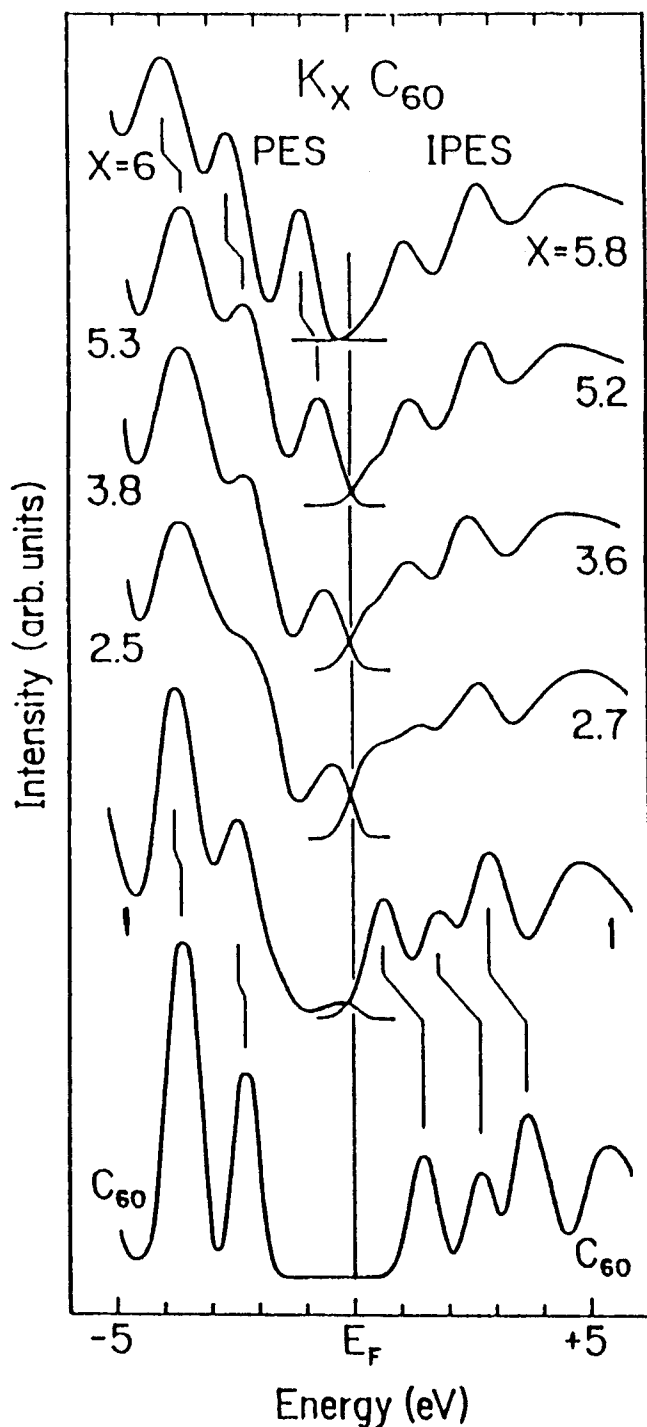
FIG. 30. Photoemission (PES) and inverse photoemission (IPES) spectra of K_3C_{60}.[199] The spectra show the effects of K incorporation in C_{60} films. The $x = 1$ spectra show emission at E_F from grains of K_3C_{60}. Adding more K results in an increase of emission below E_F and a decrease in intensity above E_F. The top spectra show that E_F shifts into the gap when the LUMO bands of C_{60} are filled by charge transfer.[199]

photoemission observations over the range of x where the doped C_{60} is not metallic (see Sec. VIII).

In this vein, photoemission and inverse photo-emission[202] studies have confirmed strong similarities between the electronic structure of K_xC_{60} and both Rb_xC_{60} and Cs_xC_{60}. However, differences have also been clearly demonstrated between the density of states for K_xC_{60} and for both Na_xC_{60} and Ca_xC_{60}, for which multiple metal ions can be accommodated in the octahedral sites (see Sec. V. C).

XII. SUPERCONDUCTIVITY

Perhaps the most striking property of the C_{60}-related materials is the observation of high temperature super-conductivity $(T_c \sim 33 \text{ K})$. The first observation of superconductivity in an alkali-metal-doped carbon material goes back to 1965 when superconductivity was observed in the first stage alkali metal graphite intercalation compound (GIC) C_8K.[203] Except for the novelty of observing superconductivity in a compound having no superconducting constituents, this observation did not attract a great deal of attention, since the T_c was very low $(\sim 140 \text{ mK})$.[203,204] Later, higher T_c's were observed in GIC's using superconducting intercalants (e.g., $KHgC_8$, for which $T_c = 1.9 \text{ K}$[205]), and in subjecting the alkali metal GIC's to pressure to increase the alkali metal uptake (e.g., NaC_2, for which $T_c \sim 5 \text{ K}$).[206]

The early observation of superconductivity at 18 K in K_3C_{60}[19] was soon followed by observations of superconductivity at even higher temperatures: in Rb_3C_{60} $(T_c = 30 \text{ K})$[187,207] and $Rb_xCs_yC_{60}$ $(T_c = 33 \text{ K})$.[45] As the quality of the materials has improved, the reported transition temperatures have risen slightly, and the widths of the transition (ΔT_c) have decreased in some cases. A large increase in T_c is achieved in going to compounds with larger intercalate atoms resulting in unit cells of larger size and with larger lattice constants as seen in Table II.[42,90,105,200] As the lattice constant increases, the ball-ball coupling decreases, narrowing the bandwidth of the LUMO level, and thereby increasing the corresponding density of states at E_F. Several experiments[195] and calculations[108] provide supporting evidence for an increased density of states at the Fermi level resulting from an increase in lattice constant. Figure 31 shows an empirical, nearly linear, relation between T_c and the lattice constant a_0 for superconducting alkali-metal-doped samples with a_0 greater than that for undoped C_{60} (see Table II).[208] This correlation includes compounds derived from alkali-metal dopants, alloys of different alkali metals,[105] and samples under pressure.[209–211] Because of the close connection between the electronic density of states at the Fermi level $N(E_F)$ and the lattice constant a_0, plots of T_c versus $N(E_F)$ similar to Fig. 31 have been made.[108] Thus, the increase in T_c is consistent with the
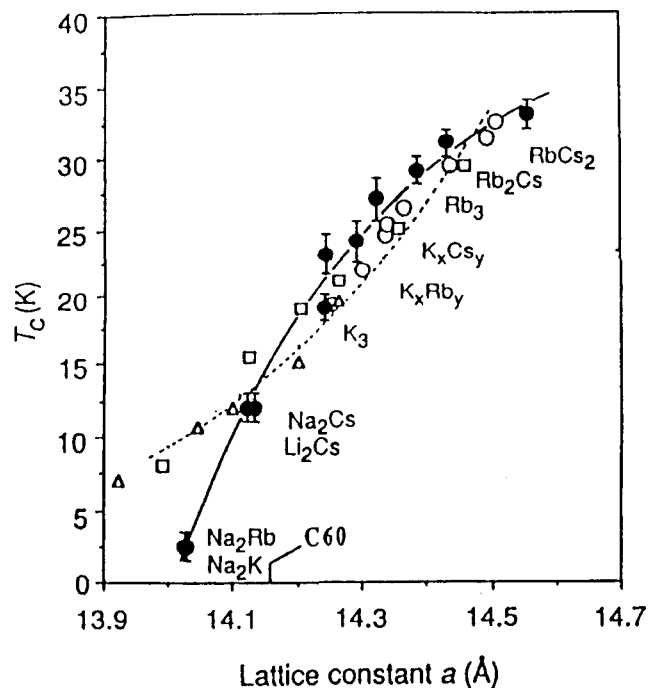

FIG. 31. Dependence of T_c on the lattice constant for various M_3C_{60} compounds.[90]

BCS expression relating the transition temperature to the density of states $N(E_F)$:

$$T_c \sim \omega_{ph} \exp[-1/VN(E_F)], \qquad (7)$$

where V is the electron-phonon coupling energy. For the donor C_{60} compounds intercalated with Li, Na, and Ca for which a_0 falls below that for C_{60} itself (see Table II), the correlation between T_c and a_0 breaks down,[42,105,106] because of the attractive electrostatic interaction introduced by the presence of the alkali metal ions in the lattice. The effect of pressure on K_3C_{60} and Rb_3C_{60}[209,210] reduces T_c in accordance with an approximately linear dependence of T_c on a_0, as shown by the open points in Fig. 31. It has also been noted that Li_3C_{60}, Na_3C_{60}, and Cs_3C_{60} do not show superconducting properties.[105] A suggested explanation for this effect is the absence of a stable cubic $Fm\bar{3}m$ or $Fm3$ structure for these stoichiometries.[105]

The reason why the T_c is so much higher in the M_3C_{60} materials relative to other carbon-based materials appears to be closely related to the high density of states that can be achieved at the Fermi level when the t_{1u} (or f_{1u}) LUMO molecular level is half-filled with carriers. However, several authors have found an enhancement in the electron-phonon coupling in C_{60}-related materials.[212–215] If the electron-phonon interaction provides the pairing mechanism for superconductivity in C_{60}-based materials, it is believed[212,214] that it is the H_g-derived phonons that play the dominant role in the

coupling. The observation of broad H_g-derived Raman lines[113,120] in M_3C_{60} is consistent with a strong electron-phonon coupling. Calculations of the contributions of the various phonon modes to the electron-phonon interaction strength[213] show that the high frequency intraball phonons may be able to account for the high T_c values that are observed experimentally.

Using scanning tunneling microscopy, the temperature dependence of the bandgap has been investigated for both K_3C_{60} and Rb_3C_{60}.[200,201] The results show a good fit of the (dI/dV) data for the superconducting state normalized to that in the normal state to the function,

$$[(dI/dV)_S/(dI/dV)_N] = \mathcal{R}e\left[\frac{|E - i\Gamma|}{[(E - i\Gamma)^2 - \Delta^2]^{1/2}}\right],$$
(8)

where E is the energy of the tunneling electrons and Γ is a broadening function. A good fit for the temperature dependence of the bandgap to BCS theory was also obtained (see Fig. 32),[201] although the zero temperature bandgap value $[2\Delta(0)/kT_c]$ was found to be 5.3 for K_3C_{60} and 5.2 for Rb_3C_{60}, well above 3.5 for the case of a BCS superconductor. These results imply that the M_3C_{60} compounds are strong coupling superconductors.[201] Further experiments relevant to the superconducting band gap are needed to establish the value of $[2\Delta(0)/kT_c]$ on firmer grounds.

There have been several measurements of the isotope effect in superconducting M_3C_{60} to provide insight into whether or not the mechanism responsible for superconductivity in the doped fullerenes involves the coupling between electrons and phonons. In the experiments reported to date, the isotopic enrichment has involved ^{13}C.[216–218] The experiments all suggest that $T_c \propto M^{-\alpha}$ where the observed α values are compared with the BCS prediction of $\alpha = 0.5$. Magnetization experiments using a SQUID magnetometer on Rb_3C_{60} where up to 75% of the carbon was the ^{13}C isotope gave $\alpha = 0.37 \pm 0.05$.[218] The result of Chen and Lieber[216] on K_3C_{60} prepared from 99% ^{13}C powder shows a value for $\alpha = 0.30 \pm 0.06$ which is consistent with a somewhat smaller α value than for the BCS theory. Similar experiments on samples with only a 33% enrichment of ^{13}C gave a much larger value of $\alpha = 1.4 \pm 0.5$.[217,219] On the basis of the superconducting gap Eq. (7), all of the reported values of the exponent α suggest that phonons are involved in the pairing mechanism for superconductivity and that the electron-phonon coupling constant is relatively large.[217,218] Future work is needed to clarify the experimental picture of the isotope effect in the M_3C_{60} compounds. Also of significance to the pairing mechanism for superconductivity in the doped fullerenes is the muon spin resonance (μSR) experiment which shows an isotropic superconducting gap,[220] as is also found in BCS superconductors.

Of interest also is the dependence of the superconducting parameters on pressure and magnetic field. Closely related to the high compressibility of C_{60}[33] and M_3C_{60} (M = K, Rb)[210] is the large linear decrease in T_c with pressure observed in K_3C_{60} and Rb_3C_{60} (see Table IV) for measurements up to a pressure of 1.9 GPa.[210] By attributing the smaller size of the K^+ ion relative to Rb^+ (0.186 Å) to an effective "chemical pressure" of 1.06 GPa, the pressure dependence of T_c for both K_3C_{60} and Rb_3C_{60} can be made to coincide,
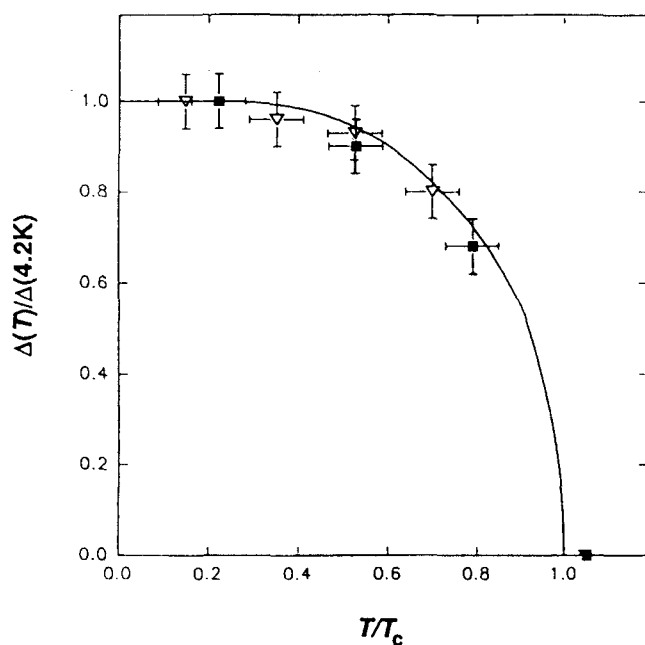

FIG. 32. Summary of the temperature-dependent energy gap results for K_3C_{60} (■) and Rb_3C_{60} (▽). For comparison the values of the gap Δ have been normalized by the respective low temperature (4.2 K) values, and the temperature has been scaled by T_c. The solid line corresponds to the temperature dependence of $\Delta(T)/\Delta(0)$ calculated by BCS theory.[201]

TABLE IV. Superconductivity parameters in M_3C_{60} (M = K, Rb).

Parameter	K_3C_{60}	Rb_3C_{60}	Reference
fcc a_0 (Å)	14.253	14.436	50
T_c (K)	19.3	29.6	19
$2\Delta(0)/kT_c$	5.2	5.3	200, 201
$(dT_c/dP)_{p=0}$ (K/GPa)	−7.8	−9.7	210
$H_{c1}(0)$ (mT)	13	12	210
$H_{c2}(0)$ (T)	49	78	210
$H_c(0)$ (T)	0.38	0.44	210
ξ_0 (nm)	2.6 ± 0.3	2.0 ± 0.25	210
λ_L (nm)	240 ± 15[a]	247 ± 15	210
$\kappa = (\lambda_L/\xi_0)$	92	124	210

[a] $\lambda_L = 480$ nm from μSR measurements.[220]

and the results can be fit to the same functional form,[210]

$$T_c(P) = T_c(0) \exp(-\gamma P), \qquad (9)$$

with the same value of $\gamma = 0.44 \pm 0.03$ GPa^{-1}.

Also listed in Table IV are values for characteristic superconducting parameters relevant to their magnetic field behavior.[209,210,221] Based on measurements of the linear temperature dependence of the upper critical field H_{c2} near T_c, the high value for the zero temperature $H_{c2}(0)$ has been estimated[209,210,222] using the Werthamer−Helfand−Hohenberg (WHH) formula[223]:

$$H_{c2}(0) = 0.69 \left[\frac{\partial H_{c2}}{\partial T} \right]_{T_c} T_c, \qquad (10)$$

and high values of $H_{c2}(0)$, exceeding the Pauli-limiting field of 35 T, have been obtained for both K_3C_{60} and Rb_3C_{60} (see Table IV). Measurements of the lower critical field H_{c1}, where the magnetic flux penetration initially occurs,[210] show that $H_{c1}(0)$ is very low and that $H_{c1}(T)$ follows the simple empirical formula,

$$[H_{c1}(T)/H_{c1}(0)] = 1 - (T/T_c)^2. \qquad (11)$$

Values for $H_{c1}(0)$ are also given in Table IV. Based on the relations,

$$H_{c2}(0) = \frac{\phi_0}{2\pi\xi_0^2}, \qquad (12)$$

where ϕ_0 is the magnetic flux quantum, and

$$H_{c1}(0) = \frac{\phi_0}{4\pi\lambda_L^2} \ln(\lambda_L/\xi_0), \qquad (13)$$

the zero temperature superconducting coherence length ξ_0 and the London penetration depth λ_L have been estimated (see Table IV),[210] showing values of ξ_0 only slightly larger than a lattice constant for the fcc unit cell. The thermodynamic critical field listed in Table IV is found from the relation,

$$H_c^2(0) = H_{c1}(0)H_{c2}(0)/\ln \kappa, \qquad (14)$$

where $\kappa = \lambda_L/\xi_0$.[210] The large values of κ listed in Table IV further imply that the M_3C_{60} compounds are strongly type II superconductors.

XIII. MAGNETIC PROPERTIES

Materials with closed shell configurations are diamagnetic. Thus, C_{60} itself is expected to be diamagnetic, since by Hund's rule the ground state for the C_{60} molecule is a nondegenerate $J = 0$ state.[154] Under certain doping conditions, fullerene-derived materials that result in a delocalized metallic state should show Pauli paramagnetism. Other dopants with unfilled d- or f-shells are expected to be paramagnetic. Thus, endohedral dopants could be one route for the preparation of magnetic fullerenes.

Interestingly, the three ions that have been most commonly used as endohedral dopants (La^{3+}, Y^{3+}, and Sc^{3+}) all have $J = 0$ (nondegenerate) ground states by Hund's rule (see Sec. VIII). Therefore, no Jahn−Teller distortion of a single endohedral ion of La^{3+}, Y^{3+}, or Sc^{3+} at the center of a C_{60} molecule is expected beyond the distortion imposed by the icosahedral symmetry of the C_{60} molecule itself. In the case of fullerenes, unusual magnetic behavior, associated with unfilled carbon p-levels, has been observed. Two examples of this unusual phenomenon have been reported.

Recent measurements of the magnetic properties of Cs-doped C_{60}[224] show unexpected behavior in the susceptibility, which implies that the molecular ions have magnetic dipole moments. For the negatively charged fullerene ions C_{60}^{n-}, the maximum magnetic moment in Cs_xC_{60} is observed experimentally at C_{60}^{4-} ($x = 4$ for Cs_4C_{60}), which is consistent with a Hund's rule prediction for the various molecular ion ground states, showing that a maximum J value ($J = 2$) for the C_{60}^{n-} ions ($0 \le n \le 6$) occurs at C_{60}^{4-}.[154] For acceptor-doped C_{60}, the maximum J value is predicted[154] to occur for the $+3$ ion, though this effect has not yet been confirmed experimentally. Although the maximum magnetic moment occurs for the C_{60}^{4-} ion, the measured effective Bohr magneton[224] is much smaller than the theoretical effective Bohr magneton given by $g[J(J + 1)]^{1/2} \simeq 2\sqrt{6}$. The large discrepancy between the observed and expected Bohr magneton may arise from a thermal averaging of J (since the spin-orbit interaction for fullerenes is so small), and from an itinerant character of the electron wave functions between the balls in the fcc lattice.

Another example of a magnetic system with only s- and p-orbitals is the organic donor TDAE (tetrakisdimethyl-aminoethylene) complex to C_{60}.[76] At low temperature, this complex exhibits ferromagnetic behavior. However, this complex shows no Curie−Weiss behavior in the temperature dependence of the susceptibility for the temperature range above the ferromagnetic ordering temperature.

XIV. C_{60}-RELATED TUBULES AND ONIONS

In addition to ball-like fullerenes, it is possible to synthesize tubular fullerenes. In analogy to the C_{60} balls, we can define C_{60}-derived tubules by bisecting a C_{60} molecule at the equator and joining the two resulting hemispheres with a cylindrical tube one monolayer thick and with the same diameter as C_{60}. If the C_{60} molecule is bisected normal to a fivefold axis, the armchair fiber shown in Fig. 33(a) is formed, and if the C_{60} molecule is bisected normal to a threefold axis, the zigzag fiber in Fig. 33(b) is formed.[225]
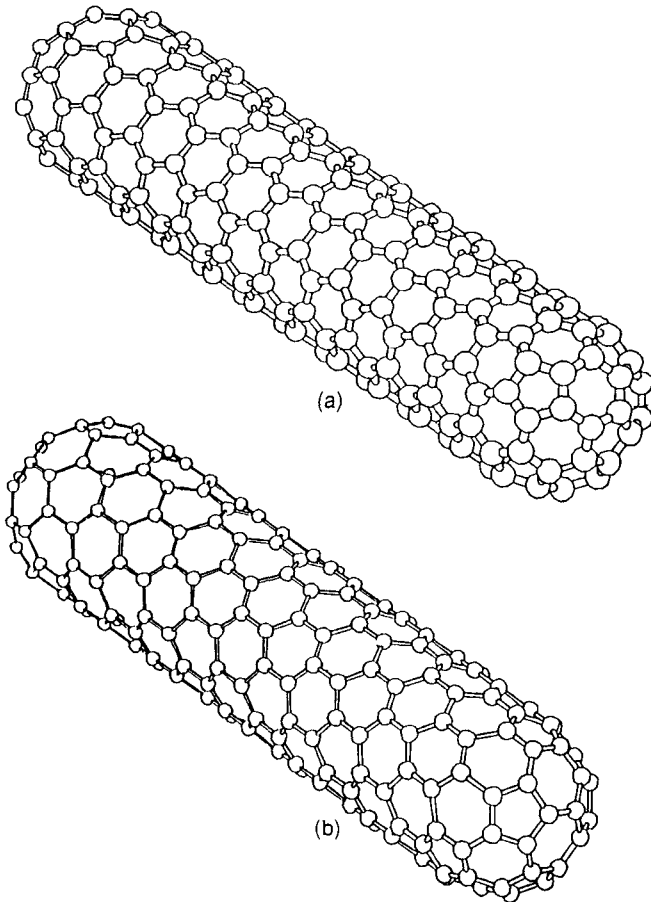
(a)

(b)

FIG. 33. By rolling up a graphene sheet (a single layer from a 3D graphite crystal) as a cylinder and capping each end of the cylinder with half of a C_{60} molecule, a "C_{60}-derived tubule" one layer in thickness is formed. Shown here is a schematic model for a tubule arising from (a) an armchair cap with a fivefold axis and (b) a zigzag cap with a threefold axis.[225]
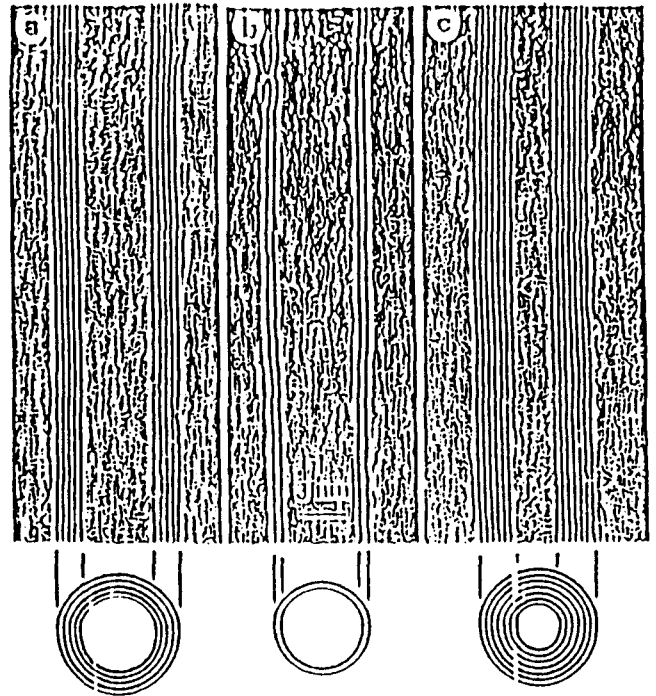

FIG. 34. The observation of N concentric carbon tubules with various inner diameters d_i and outer diameters d_o reported by Iijima using TEM.[226] (a) $N = 5$, $d_o = 67$ Å, (b) $N = 2$, $d_o = 55$ Å, and (c) $N = 7$, $d_i = 23$ Å, and $d_o = 65$ Å.

The earliest observations of carbon tubules of very small (nanometer) dimensions[226-228] were based on high resolution transmission electron microscopy (TEM) measurements (see Fig. 34), suggesting the existence of micron-long tubules that have cross sections consisting of several concentric coaxial tubes and a hollow core. In Fig. 34(b), we see one tubule with only two coaxial carbon cylinders, and another (c) with an inner diameter of only 23 Å.[226] Carbon tubules have been nucleated either on vapor grown carbon fibers[227,228] or on the surface of the negative carbon electrode in an arc discharge.[226] Recent reports of conditions for the synthesis of copious amounts of fullerene tubules by the arc discharge method have greatly stimulated activity in this field.[229,230] The assembly of the tubules into tows consisting of large numbers of tubules with similarly oriented axes has also been reported.[231] The growth of carbon tubules appears to be unfavorable under the conditions normally used to synthesize fullerene balls.[232] These fullerene tubules differ in a fundamental way from the scroll-like graphite

whiskers, synthesized by Bacon many years ago in a dc carbon arc discharge.[233] Highly elongated fullerenes with shapes between the traditional icosahedral fullerenes and the graphene tubules have also been observed by high resolution transmission electron microscopy.[234]

The growth mechanism for these cylindrical fullerene tubules is especially interesting. The nucleation of a C_{60} tubule instead of a C_{60} ball is believed by some authors to be stabilized by a defect in the cap region.[235] In one proposed growth process, the pentagonal faces in the cap region act like catalytic particles to promote tubule growth.[235] Saito et al.[236] have suggested a series of steps that incorporate a C_2 cluster through the motion of two pentagonal faces on a hemispherical fullerene-derived cap and promote tubule growth. Other authors believe that the tubules grow from open ends of the tubules.[237,238]

Iijima reports[226] that the majority of the carbon tubules, that he has observed, have screw axes and chirality. Using Fig. 35 we can specify the chirality and the tubule diameter of any graphene tubule in terms of the chiral vector $c_h = n\hat{a}_1 + m\hat{a}_2$ which connects two crystallographically equivalent sites on a 2D graphene sheet[225] where a graphene sheet denotes a single layer of the 3D graphite lattice. The construction in Fig. 35 shows the chiral angle θ with respect to the zigzag direction ($\theta = 0$) and the unit vectors $\hat{a}_1$ and $\hat{a}_2$ of
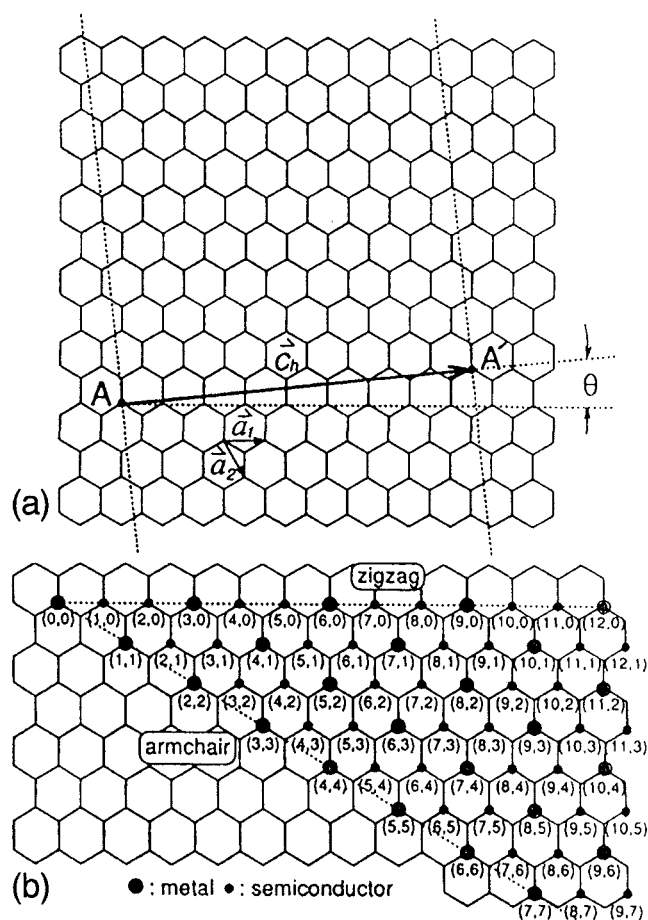
FIG. 35. (a) The vector $\mathbf{AA'}$ or $\mathbf{c}_h = n\hat{a}_1 + m\hat{a}_2$ on the honeycomb lattice defined by unit vectors, $\hat{a}_1$ and $\hat{a}_2$, and the chiral angle θ with respect to the zigzag axis. (b) Possible vectors for general tubules, including zigzag, armchair, and chiral tubules. The large dots and small bullets, respectively, denote metallic and semiconducting behavior for each of the possible tubules.[225]

the hexagonal honeycomb lattice. The armchair tubule [Fig. 33(a)] corresponds to $\theta = 30°$ on this construction. An ensemble of possible vectors specified by pairs of integers (n, m) denoting the vector $\mathbf{c}_h = n\hat{a}_1 + m\hat{a}_2$ is given in Fig. 35(b).[239]

The cylinder connecting the two hemispherical caps is formed by superimposing the two ends of the vector $\mathbf{c}_h$, and the cylinder joint is made by superimposing the two lightly dotted parallel lines in Fig. 35 which are perpendicular to the vector $\mathbf{c}_h$ at each end.[225] The chiral tubule thus generated has no distortion of bond angles other than distortions caused by the cylindrical curvature of the tubule. Differences in chiral angle θ and in the tubule diameter d give rise to differences in the properties of the various graphene tubules. In the (n, m) notation for $\mathbf{c}_h = n\hat{a}_1 + m\hat{a}_2$, the vectors $(n, 0)$ denote zigzag tubules and the vectors (n, n) denote armchair tubules. All other vectors (n, m) correspond to chiral tubules.[239] Of course, both right- and left-handed

chirality is possible for chiral tubules. Therefore, it is expected that chiral tubules are optically active to either right- or left-circularly polarized light, depending on their chirality. In terms of the integers (n, m), the tubule diameter d is given by

$$d = \sqrt{3}\, a_{C-C}(m^2 + mn + n^2)^{1/2}/\pi, \qquad (15)$$

and the chiral angle θ is given by

$$\theta = \tan^{-1}\left[\sqrt{3}\, n/(2m + n)\right]. \qquad (16)$$

For example, a zigzag tubule $(\theta = 0°)$ with $(m, 0) = (9, 0)$ has a tubule diameter of 7.05 Å, while an armchair tubule $(5, 5)$ has $d = 6.83$ Å, corresponding to the C_{60} hemispherical caps discussed above.

The basis for a projection mapping of a chiral tubule $(n, m) = (10, 5)$ is shown in Fig. 36[86] for a hemispherical cap formed from a C_{140} fullerene (diameter 10.36 Å). By adding many rows of hexagons parallel to AB and CD, a properly capped chiral graphene tubule is obtained,[86] as shown in Fig. 36(c). The projection concept illustrated in Fig. 36 can be extended to generate all possible chiral tubules specified in Fig. 35(b). Many of these chiral tubules can in fact have a multiplicity of caps, each generating the same vector $\mathbf{c}_h = n\hat{a}_1 + m\hat{a}_2$ and, hence, the same chiral tubule.[239]

Because of the special atomic arrangement of the carbon atoms in a C_{60} tubule, substitutional impurities are inhibited by the small size of the carbon atoms. Furthermore, the screw axis dislocation, the most common defect found in bulk graphite, is inhibited by the monolayer structure of the C_{60} tubule. The special geometry of C_{60} and C_{60}-related tubules should make these structures relatively incompressible to hydrostatic stress, when compared to other materials.[240]

From a theoretical standpoint, fullerene tubules are interesting as examples of a one-dimensional periodic structure along the tubule axis. Confinement in the radial direction is provided by the monolayer thickness of the tubule. In the circumferential direction, periodic boundary conditions apply to the enlarged unit cell that is formed in real space and the subsequent zone folding that occurs in reciprocal space. We can then expect to observe 1D dispersion relations for electrons and phonons in C_{60}-derived tubules.

A number of methods have been used to calculate the 1D electronic energy bands for fullerene tubules[236,241–244] and all relate to the 2D graphene honeycomb sheet used to form the tubule. The unit cells in real and reciprocal space used to calculate the energy bands for armchair and zigzag tubules are shown in Fig. 37. These calculated results for the 1D electronic structure show that for small diameter graphene tubules, about 1/3 of the tubules are metallic and 2/3 are semiconducting, depending on the tubule diameter d
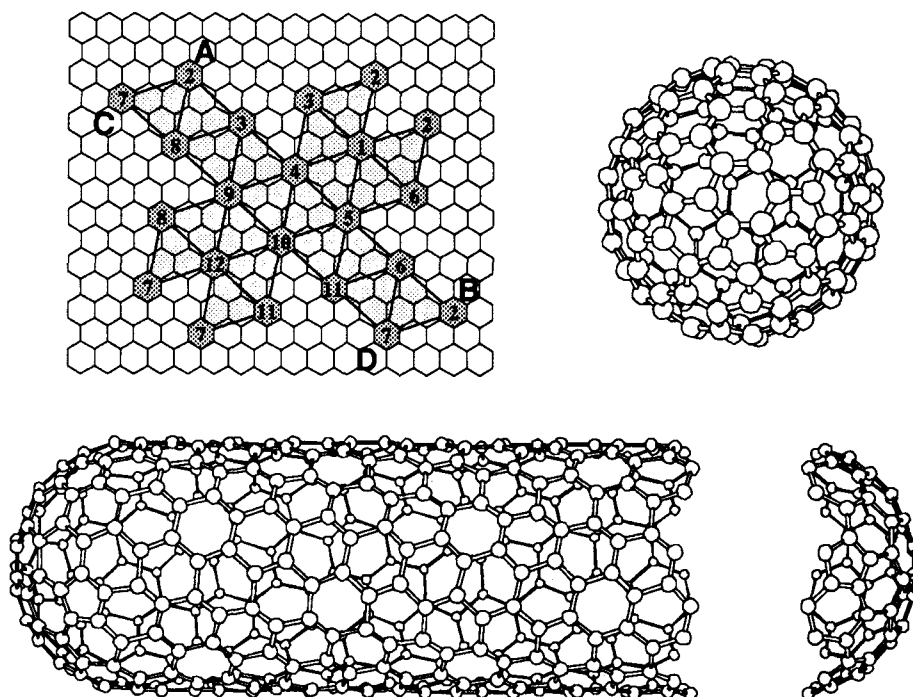
FIG. 36. (a) The projection of an icosahedral C_{140} fullerene onto a honeycomb lattice where each of the twelve numbered hexagons denotes the location of a pentagonal defect in the honeycomb lattice. (b) By bringing the pentagonal defects with the same numbers into coincidence, the C_{140} fullerene with icosahedral I symmetry (lacking inversion symmetry) is formed. (c) A graphene tubule generated from two hemispherical $C_{140/2}$ caps obtained by bisecting the C_{140} fullerene normal to a fivefold axis and adding many rows of hexagons parallel to AB and CD.[86]

and chiral angle θ. Metallic conduction in a fullerene tubule is achieved when

$$2n + m = 3q, \tag{17}$$

where n and m are integers specifying the tubule diameter and chiral angle in Eqs. (15) and (16) and q is an integer. Tubules satisfying Eq. (17) are indicated in Fig. 35(b) as large circles, and these are the metallic tubules. The small circles in this figure correspond to semiconducting tubules.

Dispersion relations are shown for metallic tubules $(m, n) = (5, 5)$ and $(9, 0)$ in Figs. 38(a) and 38(b), respectively, and for a semiconducting tubule $(m, n) = (10, 0)$ in Fig. 38(c).[245] Figure 35(b) shows that all armchair tubules are metallic, but only $1/3$ of the possible zigzag tubules are metallic.[239] Also of interest in this connection is the density of states for metallic and semiconducting tubules, as is illustrated in Fig. 39[239] for the $(9, 0)$ and $(10, 0)$ tubules, respectively.[239] Here we see a finite density of states at the Fermi level for the $(9, 0)$ tubules, and a vanishing density of states for the $(10, 0)$ tubules, consistent with the metallic nature of the $(9, 0)$ tubules and the semiconducting nature of the $(10, 0)$ zigzag tubules. It may seem surprising that the calculated electronic structure can be either metallic or semiconducting depending on the choice

of (n, m), although there is no difference in the local chemical bonding between the carbon atoms in the tubules, and no doping impurities are present.[239] These surprising results can be understood on the basis of the electronic structure of 2D graphite which is a zero gap semiconductor[247] with bonding and antibonding π bands, degenerate at the K-point (zone corner) of the 2D hexagonal Brillouin zone. The periodic boundary conditions for the 1D tubules permit only a few wave vectors to exist in the circumferential direction. If one of these passes through the K-point in the Brillouin zone, then metallic conduction results.

Metallic 1D energy bands are generally unstable under a Peierls distortion. However, the Peierls energy gap obtained for the metallic tubules is found to be greatly suppressed by increasing the tubule diameter, so that the Peierls gap quickly approaches the zero-energy gap of 2D graphite.[241,246] Thus, if we consider finite temperatures or fluctuation effects, such a small Peierls gap can be neglected. It is also of interest to note that as the tubule diameter increases, more wave vectors become allowed for the circumferential direction, the tubules become more two-dimensional, and the semiconducting band gap disappears, as is illustrated in Fig. 39(c) which shows the diameter dependence of the semiconducting band gap. Calculation of the electronic structure for
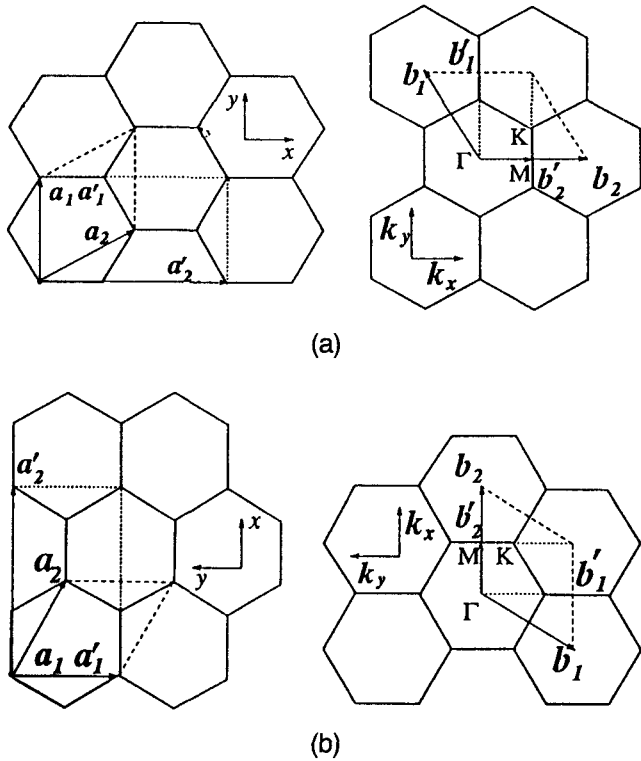
(a)

(b)

FIG. 37. Unit cell in real space and the Brillouin zone for (a) armchair and (b) zigzag tubules ($\cdots\cdots$). Those for a 2D graphene sheet (- - -) are shown for comparison.[239] The unit vectors of the honeycomb lattice in real and reciprocal space are denoted by the a_i and b_i vectors, respectively. The corresponding unit vectors for the tubule unit cells are indicated by primes.

two concentric tubules shows that pairs of concentric metal-semiconductor or semiconductor-metal tubules are stable.[248]

From these results one could imagine designing a minimum-size conductive wire consisting of two concen-

tric graphene tubules with a metallic inner tubule covered by a semiconducting (or insulating) outer tubule. This concept could be extended to the design of tubular metal-semiconductor devices without introducing any doping impurities.[239] There are many possibilities for arranging arrays of metallic and semiconducting graphene tubules from a conceptual standpoint. It will be interesting to see what kinds of tubules and tubule arrays can be synthesized from a practical standpoint.

The elastic properties of fullerene tubules have also been considered by carrying out lattice mode calculations of long fullerene tubules based on 30 carbon atom hemispherical caps from C_{60} and consisting of 100, 200, and 400 carbon atoms.[240] These calculations show that the lowest bending mode decreases as the length of the fullerene tube increases, saturating at a cluster size of about 200 carbon atoms. The magnitude of the beam rigidity of these tubules is found to exceed that of presently available materials,[240] so that graphene tubules are expected to offer outstanding mechanical properties. Kosakovskaya et al. have also reported extreme hardness for tows of carbon tubules, exceeding that of the toughest alloys which they used as substrates.[231]

In the limit of large diameter, the coaxial tubules, discussed above, can be related to vapor grown carbon fibers[249] that possess a similar organizational pattern to the coaxial tubules.[250] Also known in the realm of carbon-based materials are hollow carbon spherules ranging from 100 Å to 1 μm outer diameter which consist of concentric spherical graphitic shells and are classified under the heading of carbon blacks.[251–253] Ugarte has recently reported[254] the formation of hollow concentric carbon spheres upon intense electron beam irradiation of soot. Of particular interest in the recent concentric carbon sphere studies is the observa-
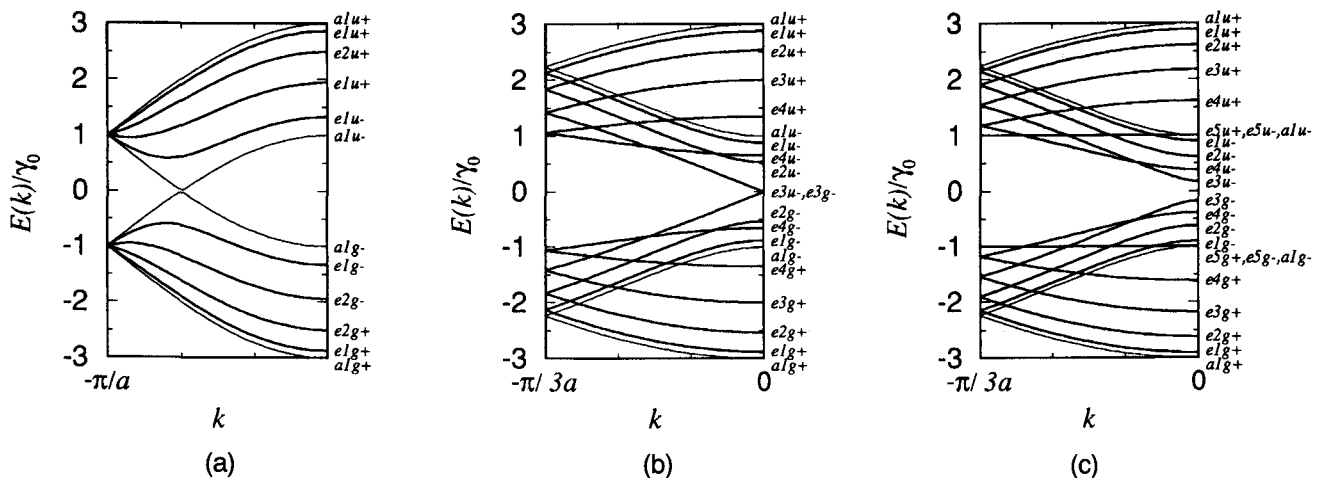

FIG. 38. One-dimensional energy dispersion relations for an (a) armchair (5, 5) tubule, (b) zigzag (9, 0) tubule, and (c) zigzag (10, 0) tubule labeled by the irreducible representations of the point group $D_{(2n+1)d}$ at $k = 0$. The A-bands are nondegenerate, and the E-bands are doubly degenerate at a general k-point.[239,245,246]
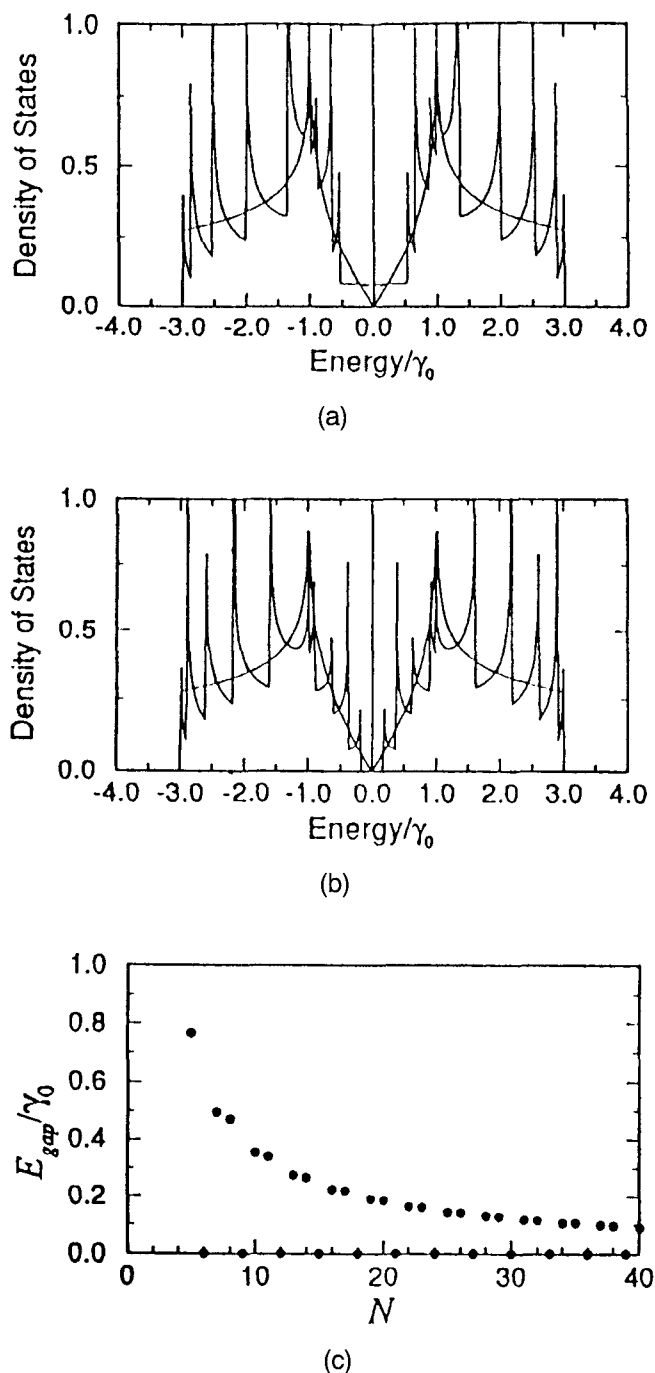
(a)

(b)

(c)

FIG. 39. Electronic 1D density of states for two (n, m) zigzag tubules: (a) the $(9, 0)$ tubule which has metallic behavior, (b) the $(10, 0)$ tubule which has semiconducting behavior, and (c) the dependence of the energy gap (normalized to the nearest neighbor overlap energy) on tubule diameter (expressed as the number of carbon atoms N along the circumference) is presented for the zigzag tubules.[248]

tion of an inner diameter of 7.1 Å, corresponding to the diameter of the C_{60} molecule. It is found that if enough energy is provided to form concentric spherical shell structures, their formation is favored over the coaxial tubule structures.[254] In this work, spheri-

cal shells up to diameter dimensions of 100 Å have been synthesized, similar to the dimensions reported for spherical shells of carbon blacks. Though containing a large amount of strain energy, the spherical shells contain no dangling bonds, making the spheres more stable than graphite sheets under some circumstances.[255] Ugarte has speculated that the spherical shells (or "onions" as he calls them) constitute another form of carbon, consisting of a fullerene at the center and an epitaxial, concentric growth of layers about the central core.[254]

XV. APPLICATIONS

Because graphite is a material of extreme properties (high modulus, high strength, high thermal conductivity, high anisotropy, high melting point, etc.), and because of the similarities between the bonding in graphite and C_{60}, we might also expect fullerenes to exhibit extreme properties. In contrast to graphite where the planes are weakly van der Waals bonded, solid C_{60} has weak van der Waals interball bonding and strong intraball bonds. Although research on solid C_{60} and related materials is still at an early stage, these materials are already beginning to show many exceptional properties, some of which may lead to practical applications.

One promising application for C_{60} is as an optical limiter. Optical limiters are used to protect materials from damage by high light intensities via a saturation of the transmitted light intensity with increasing incident intensity. Outstanding performance for C_{60} relative to presently used optical limiting materials has been observed at 5320 Å for 8 ns pulses using solutions of C_{60} in toluene and in chloroform (CH_3Cl).[178] Although C_{70} in similar solutions also showed optical limiting action, the performance of C_{60} was found to be superior. The proposed mechanism for the optical limiting is that C_{60} and C_{70} are more absorptive at the triplet excited state than for the ground state (see Sec. IX). In this process, the initial absorption of a photon (which takes a molecule from a singlet S_0 state to an excited singlet state) is followed by an intersystem crossing from the singlet to a triplet state. Because of the higher excitation cross section for molecules in a triplet state (in comparison to a singlet state), the population of the metastable triplet state promotes further stronger absorption of photons (see Sec. IX).[178]

The possible use of C_{60} for the fabrication of industrial diamonds offers another area for possible applications. It is found that when rapid nonhydrostatic pressures (in the range of 20 GPa) are applied at room temperature to C_{60}, the material is transformed instantaneously into bulk polycrystalline diamond at high efficiency.[256] It is believed that the presence of pentagons in the C_{60} structure promotes the formation of sp^3 bonds during the application of high anisotropic stress.

2092

J. Mater. Res., Vol. 8, No. 8, Aug 1993

Enhanced nucleation of diamond crystallites on a Si substrate has been achieved through the deposition of a 500–1000 Å C_{70} film, activation of the film by positive ion bombardment, and followed by CVD growth in a microwave plasma reactor. A base layer of ion-activated C_{70} was found to be more effective in promoting sp^3 bonding[257] than a similarly treated C_{60} buffer layer. Normally, for diamond films to grow from a mixture of gaseous CH_3 and H_2, the substrate surface (usually Si) must be pretreated with diamond grit polish or must contain small diamond seeds.

Another interesting application is the photoconducting device that can be fabricated using fullerene-doped polymers. Polyvinylcarbazole (PVK) doped with a mixture of C_{60} and C_{70} has been reported to exhibit exceptionally good photoconductive properties[258] which may lead to the development of future polymeric photoconductive materials. The effects of the fullerenes (~2.7% by weight) on the charge generation and transport still need to be understood.

Ever since C_{60} was discovered,[5] the possibility of using fluorinated derivatives such as $C_{60}F_{60}$ as lubricants was considered. It has, however, recently been shown that highly fluorinated C_{60} is unstable in the presence of trace amounts of H_2O[259] and therefore is probably unsuitable for application as a lubricant.

As further research on these materials is carried out, it is expected, because of the extreme properties exhibited by carbon-based materials generally, that other interesting physics and chemistry will be discovered, and promising applications will be found for C_{60} and C_{60}-related materials.

ACKNOWLEDGMENTS

REFERENCES

1. L. Tisza, Z. Phys. **82**, 48 (1933).
2. E. Osawa, Kagaku (Kyoto) **25**, 854–863 (1970, in Japanese).
3. D. A. Bochvar and E. G. Gal'pern, Dok. Akad. Nauk SSSR **209**, 610–615 (1973). English translation: Proc. Acad. Sci. USSR **209**, 239–244 (1973).
4. I. V. Stankevich, M. V. Nikerov, and D. A. Bochvar, Russ. Chem. Rev. **53**, 640 (1984).
5. H. W. Kroto, J. R. Heath, S. C. O'Brien, R. F. Curl, and R. E. Smalley, Nature **318**, 162 (1985).
6. E. Herbig, Astrophys. J. **196**, 129 (1975).
7. A. Leger and J. L. Puget, Astr. Astrophys. Lett. **137**, L5 (1984).
8. A. Leger, L. d'Hendecourt, L. Verstraete, and W. Schmidt, Astr. Astrophys. **203**, 145 (1987).
9. J. P. Hare and H. W. Kroto, Accounts Chem. Res. **25**, 106 (1992).
10. R. Buckminster Fuller and E. J. Applewhite, in *Synergetics: Explorations in the Geometry of Thinking* (Garland Publishing, New York, 1975).
11. R. Buckminster Fuller, in *The Artifacts of R. Buckminster Fuller: A Comprehensive Collection of His Designs and Drawings*, edited by W. Marlin (Garland Publishing, New York, 1984).
12. E. A. Rohlfing, D. M. Cox, and A. Kaldor, J. Chem. Phys. **81**, 3322 (1984).
13. R. Taylor, J. P. Hare, A. K. Abdul-Sada, and H. W. Kroto, J. Chem. Soc., Chem. Commun. **20**, 1423 (1990).
14. R. D. Johnson, G. Meijer, and D. S. Bethune, J. Am. Chem. Soc. **112**, 8983 (1990).
15. R. Tycko, R. C. Haddon, G. Dabbagh, S. H. Glarum, D. C. Douglass, and A. M. Mujsce, J. Phys. Chem. **95**, 518 (1991).
16. R. D. Johnson, D. S. Bethune, and C. S. Yannoni, Accounts Chem. Res. **25**, 169 (1992).
17. W. Krätschmer, L. D. Lamb, K. Fostiropoulos, and D. R. Huffman, Nature **347**, 354 (1990).
18. R. F. Curl and R. E. Smalley, Science **242**, 1017 (1988).
19. R. C. Haddon, A. F. Hebard, M. J. Rosseinsky, D. W. Murphy, S. J. Duclos, K. B. Lyons, B. Miller, J. M. Rosamilia, R. H. Fleming, A. R. Kortan, S. H. Glarum, A. V. Makhija, A. J. Muller, R. H. Eick, S. M. Zahurak, R. Tycko, G. Dabbah, and F. A. Thiel, Nature **350**, 320 (1991).
20. A. F. Hebard, M. J. Rosseinsky, R. C. Haddon, D. W. Murphy, S. H. Glarum, T. T. M. Palstra, A. P. Ramirez, and A. R. Kortan, Nature **350**, 600 (1991).
21. A. F. Hebard, Phys. Today **45** (Nov.), 26 (1992).
22. P. R. Buseck, S. J. Tsipursky, and R. Hettich, Science **257**, 215 (1992); Science **257**, 167 (1992).
23. F. Diederich, R. Ettl, Y. Rubin, R. L. Whetten, R. Beck, M. Alvarez, S. Anz, D. Sensharma, F. Wudl, K. C. Khemani, and A. Koch, Science **252**, 548 (1991).
24. C-C. Chen, S. P. Kelty, and C. M. Lieber, Science **253**, 886 (1991).
25. M. S. Meier and J. P. Selegue, J. Org. Chem. **57**, 1925 (1992).
26. F. Diederich and R. L. Whetten, Accounts Chem. Res. **25**, 119 (1992).
27. G. Smart, B. Eldridge, W. Reuter, J. A. Zimmerman, W. R. Creasy, N. Rivera, and R. S. Ruoff, Chem. Phys. Lett. **188**, 171 (1992).
28. S. L. Ren, Y. Wang, A. M. Rao, E. McRae, G. T. Hager, K. A. Wang, W. T. Lee, H. F. Ni, J. Selegue, and P. C. Eklund, Appl. Phys. Lett. **59**, 2678 (1991).
29. R. L. Meng, D. Ramirez, X. Jiang, P. C. Chow, C. Diaz, K. Matsuishi, S. C. Moss, P. H. Hor, and C. W. Chu, Appl. Phys. Lett. **59**, 3402 (1991).
30. R. E. Smalley, in *Large Carbon Clusters*, edited by G. S. Hammond and V. J. Kuck (American Chemical Society, Washington, DC, 1991), p. 199.
31. R. E. Smalley, Accounts Chem. Res. **25**, 98 (1992).
32. W. I. F. David, R. M. Ibberson, J. C. Matthewman, K. Prassides, T. J. S. Dennis, J. P. Hare, H. W. Kroto, R. Taylor, and D. R. M. Walton, Nature **353**, 147 (1991).
33. J. E. Fischer, P. A. Heiney, A. R. McGhie, W. J. Romanow, A. M. Denenstein, J. P. McCauley, Jr., and A. B. Smith III, Science **252**, 1288 (1991).
34. R. M. Fleming, T. Siegrist, P. M. March, B. Hessen, A. R. Kortan, D. W. Murphy, R. C. Haddon, R. Tycko, G. Dabbagh, A. M. Mujsce, M. L. Kaplan, and S. M. Zahurak, in *Clusters and Cluster-Assembled Materials*, edited by R. S. Averback, J. Bernholc, and D. L. Nelson (Mater. Res. Soc. Symp. Proc. **206**, Pittsburgh, PA, 1991), p. 691.
35. W. I. F. David, R. M. Ibberson, T. J. S. Dennis, J. P. Hare, and K. Prassides, Europhys. Lett. **18**, 219 (1992); Europhys. Lett. **18**, 735 (1992).

36. J. E. Field, in *Properties of Diamond,* edited by J. E. Field (Academic Press, London, 1979), p. 281.

37. H. Selig, C. Lifshitz, T. Peres, J. E. Fischer, A. R. McGhie, W. J. Romanow, J. P. McCauley, Jr., and A. B. Smith III, J. Am. Chem. Soc. **113**, 5475 (1991).

38. J. H. Holloway, E. G. Hope, R. Taylor, G. J. Langley, A. G. Avent, T. J. Dennis, J. P. Hare, H. W. Kroto, and D. R. M. Walton, J. Chem. Soc., Chem. Commun. 966 (1991).

39. R. E. Haufler, J. J. Conceicao, L. P. F. Chibante, Y. Chai, N. E. Byrne, S. Flanagan, M. M. Haley, S. C. O'Brien, C. Pan, Z. Xiao, W. E. Billups, M. A. Ciufolini, R. H. Hauge, J. L. Margrave, L. J. Wilson, R. F. Curl, and R. E. Smalley, J. Phys. Chem. **94**, 8634 (1990).

40. P. R. Birkett, P. B. Hitchcock, H. W. Kroto, R. Taylor, and D. R. M. Walton, Nature **357**, 479 (1992).

41. M. S. Dresselhaus and G. Dresselhaus, Adv. Phys. **30**, 139 (1981).

42. M. J. Rosseinsky, D. W. Murphy, R. M. Fleming, R. Tycko, A. P. Ramirez, T. Siegrist, G. Dabbagh, and S. E. Barrett, Nature **356**, 416 (1992).

43. C. Gu, F. Stepniak, D. M. Poirier, M. B. Jost, P. J. Benning, Y. Chen, T. R. Ohno, J. L. Martins, J. H. Weaver, J. Fure, and R. E. Smalley, Phys. Rev. B **45**, 6348 (1992).

44. P. J. Benning, D. M. Poirier, T. R. Ohno, Y. Chen, M. B. Jost, F. Stepniak, G. H. Kroll, and J. H. Weaver, Phys. Rev. B **45**, 6899 (1992).

45. K. Tanigaki, T. W. Ebbesen, S. Saito, J. Mizuki, J. S. Tsai, Y. Kubo, and S. Kuroshima, Nature **352**, 222 (1991).

46. A. Hérold, in *Physics and Chemistry of Materials with Layered Structures,* edited by F. Lévy (Dordrecht Reidel, New York, 1979), p. 323.

47. X. D. Xiang, W. A. Vareka, A. Zettl, J. L. Corkill, T. W. Barbee III, M. L. Cohen, N. Kijima, and R. Gronsky, Science **254**, 1487 (1991).

48. X. D. Xiang, A. Zettl, W. A. Vareka, J. L. Corkill, T. W. Barbee III, and M. L. Cohen, Phys. Rev. B **43**, 11496 (1991).

49. X-D. Xiang, J. G. Hou, G. Briceno, W. A. Vareka, R. Mostovoy, A. Zettl, V. H. Crespi, and M. L. Cohen, Science **256**, 1190 (1992).

50. A. R. Kortan, N. Kopylov, S. Glarum, E. M. Gyorgy, A. P. Ramirez, R. M. Fleming, F. A. Thiel, and R. C. Haddon, Nature **355**, 529 (1992).

51. Y. Chen, F. Stepniak, J. H. Weaver, L. P. F. Chibante, and R. E. Smalley, Phys. Rev. B **45**, 8845 (1992).

52. P. W. Stephens, L. Mihaly, P. L. Lee, R. L. Whetten, S. M. Huang, R. Kaner, F. Diederich, and K. Holczer, Nature **351**, 632 (1991).

53. S. J. Woo, S. H. Lee, E. Kim, K. H. Lee, Y. H. Lee, S. Y. Hwang, and I. C. Jeon, Phys. Lett. A **162**, 501 (1992).

54. J. E. Fischer, P. A. Heiney, and A. B. Smith III, Accounts Chem. Res. **25**, 112 (1992).

55. S. Saito and A. Oshiyama, Phys. Rev. B **44**, 11532 (1991).

56. L. S. Wang, J. Conceicao, C. Jim, and R. E. Smalley, Chem. Phys. Lett. **182**, 5 (1991).

57. J. de Vries, H. Steger, B. Kamke, C. Menzel, B. Weisser, W. Kamke, and I. V. Hertel, Chem. Phys. Lett. **188**, 159 (1992).

58. H. Steger, J. de Vries, B. Kamke, W. Kamke, and T. Drewello, Chem. Phys. Lett. **194**, 452 (1992).

59. P. A. Heiney, G. B. M. Vaughan, J. E. Fischer, N. Coustel, D. E. Cox, J. R. D. Copley, D. A. Neumann, W. A. Kamitakahara, K. M. Creegan, D. M. Cox, J. P. McCauley, Jr., and A. B. Smith III, Phys. Rev. B **45**, 4544 (1992).

60. A. M. Rao, P. Zhou, K-A. Wang, G. T. Hager, J. M. Holden, Y. Wang, W. T. Lee, X. X. Bi, P. C. Eklund, D. S. Cornett, M. A. Duncan, and I. J. Amster, Science **259**, 955 (1993).

61. G. Dresselhaus, M. S. Dresselhaus, and J. G. Mavroides, Carbon **4**, 433 (1966).

62. X. D. Shi, A. R. Kortan, J. M. Williams, A. M. Kini, B. M. Saval, and P. M. Chaikin, Phys. Rev. Lett. **68**, 827 (1992).

63. E. Grivei, B. Nysten, M. Cassart, J. P. Issi, C. Fabre, and A. Rassat, Phys. Rev. B **47**, 1705 (1993).

64. E. Grivei, B. Nysten, M. Cassart, A. Demain, and J. P. Issi, Solid State Commun. **85**, 73 (1993).

65. E. Grivei, M. Cassart, J. P. Issi, L. Langer, B. Nysten, J. P. Michenaud, C. Fabre, and A. Rassat, unpublished.

66. R. C. Yu, N. Tea, M. B. Salamon, D. Lorens, and R. Malhotra, Phys. Rev. Lett. **68**, 2050 (1992).

67. Y. Wang, J. M. Holden, A. M. Rao, W-T. Lee, G. T. Hager, X. X. Bi, S. L. Ren, G. W. Lehman, and P. C. Eklund, Phys. Rev. B **45**, 14396 (1992).

68. Q. Zhu, D. E. Cox, J. E. Fischer, K. Kniaz, A. R. McGhie, and O. Zhou, Nature **355**, 712 (1992).

69. T. R. Ohno, G. H. Kroll, J. H. Weaver, L. P. F. Chibante, and R. E. Smalley, Nature **350**, 401 (1992).

70. S. Saito, in *Clusters and Cluster-Assembled Materials,* edited by R. S. Averback, J. Bernholc, and D. L. Nelson (Mater. Res. Soc. Symp. Proc. **206**, Pittsburgh, PA, 1991), p. 115.

71. F. Wudl, Accounts Chem. Res. **25**, 157 (1992).

72. P. J. Fagan, J. C. Calabrese, and B. Malone, Accounts Chem. Res. **25**, 134 (1992).

73. J. M. Hawkins, Accounts Chem. Res. **25**, 150 (1992).

74. J. M. Hawkins, A. Meyer, T. Lewis, and S. Loren, in *Fullerenes,* edited by G. S. Hammond and V. J. Kuck, ACS Symposium Series, 481, Chap. 6 (American Chemical Society, Washington, DC, 1992), p. 91.

75. A. L. Balch, V. J. Catalano, J. W. Lee, M. M. Olmstead, and S. R. Parkin, J. Chem. Soc., Chem. Commun. 113 (1991).

76. P-M. Allemand, K. C. Khemani, A. Koch, F. Wudl, K. Holczer, S. Donovan, G. Grüner, and J. D. Thompson, Science **253**, 301 (1991).

77. G. Dresselhaus, M. S. Dresselhaus, and P. C. Eklund, Phys. Rev. B **45**, 6923 (1992).

78. C. S. Yannoni, R. D. Johnson, G. Meijer, D. S. Bethune, and J. R. Salem, J. Phys. Chem. **95**, 9 (1991).

79. H. Ajie, M. M. Alvarez, S. J. Anz, R. D. Beck, F. Diederich, K. Fostiropoulos, D. R. Huffman, W. Krätschmer, Y. Rubin, K. E. Schriver, D. Sensharma, and R. L. Whetten, J. Phys. Chem. **94**, 8630 (1990).

80. P. W. Fowler and J. Woolrich, Chem. Phys. Lett. **127**, 78 (1986).

81. D. J. Klein, W. A. Seitz, and T. G. Schmalz, Nature **323**, 703 (1986).

82. S. Maruyama, L. R. Anderson, and R. E. Smalley, Rev. Sci. Instrum. **61**, 3686 (1990).

83. Y. Maruyama, T. Inabe, H. Ogata, Y. Achiba, S. Suzuki, K. Kikuchi, and I. Ikemoto, Chem. Lett. 1849 (1991). The Chemical Society of Japan.

84. K. Kikuchi, N. Nakahara, T. Wakabayashi, S. Suzuki, H. Shiramaru, Y. Miyake, K. Saito, I. Ikemoto, M. Kainosho, and Y. Achiba, Nature **357**, 142 (1992).

85. D. E. Manolopoulos and P. W. Fowler, Chem. Phys. Lett. **187**, 1 (1991).

86. M. Fujita, R. Saito, G. Dresselhaus, and M. S. Dresselhaus, Phys. Rev. B **45**, 13834 (1992).

87. G. B. Vaughan, P. A. Heiney, J. E. Fischer, D. E. Luzzi, D. A. Ricketts-Foot, A. R. McGhie, Y. W. Hui, A. L. Smith, D. E. Cox, W. J. Romanow, B. H. Allen, N. Coustel, J. P. McCauley, Jr., and A. B. Smith III, Science **254**, 1350 (1991).

88. M. A. Verheijen, H. Meekes, G. Meijer, P. Bennema, J. L. de Boer, S. van Smaalen, G. van Tendeloo, S. Amelinckx, S. Muto, and J. van Landuyt, Chem. Phys. **166**, 287 (1992).

89. R. M. Fleming, M. J. Rosseinsky, A. P. Ramirez, D. W. Murphy, J. C. Tully, R. C. Haddon, T. Siegrist, R. Tycko, S. H. Glarum, P. Marsh, G. Dabbagh, S. M. Zahurak, A. V. Makhija, and C. Hampton, Nature **352**, 701 (1991).

90. R. M. Fleming, A. P. Ramirez, M. J. Rosseinsky, D. W. Murphy, R. C. Haddon, S. M. Zahurak, and A. V. Makhija, Nature **352**, 787 (1991).

91. P. A. Heiney, J. E. Fischer, A. R. McGhie, W. J. Romanow, A. M. Denenstein, J. P. McCauley, Jr., A. B. Smith III, and D. E. Cox, Phys. Rev. Lett. **67**, 1468 (1991).

92. A. Dworkin, H. Szwarc, S. Leach, J. P. Hare, T. J. Dennis, H. W. Kroto, R. Taylor, and D. R. M. Walton, C.R. Acad. Sci., Paris Serie II **312**, 979 (1991).

93. T. Atake, T. Tanaka, R. Kawaji, K. Kikuchi, K. Saito, S. Suzuki, I. Ikemoto, and Y. Achiba, Phys. C **185–189**, 427 (1991).

94. T. Matsuo. H. Suga, W. I. F. David, R. M. Ibberson, P. Bernier, A. Zahab, C. Fabre, A. Rassat, and A. Dworkin, Solid State Commun. **83**, 711 (1992).

95. R. Tycko, G. Dabbagh, R. M. Fleming, R. C. Haddon, A. V. Makhiji, and S. M. Zahurak, Phys. Rev. Lett. **67**, 1886 (1991).

96. A. Dworkin, C. Fabre, D. Schutz, G. Kriza, R. Ceolin, H. Szwarc, P. Bernier, D. Jerome, S. Leach, A. Rassat, J. P. Hare, T. J. Dennis, H. W. Kroto, R. Taylor, and D. R. M. Walton, C.R. Acad. Sci., Paris Serie II **313**, 1017 (1991).

97. P. H. M. van Loosdrecht, P. J. M. van Bentum, and G. Meijer, Phys. Rev. Lett. **68**, 1176 (1992).

98. A. B. Harris and R. Sachidanandam, Phys. Rev. B **46**, 4944 (1992).

99. W. P. Beyermann, M. F. Hundley, J. D. Thompson, F. N. Diederich, and G. Grüner, Phys. Rev. Lett. **68**, 2046 (1992).

100. G. B. Alers, B. Golding, A. R. Kortan, R. C. Haddon, and F. A. Thiel, Science **257**, 511 (1992).

101. G. van Tendeloo, S. Amelinckx, M. A. Verheijen, P. H. M. van Loosdrecht, and G. Meijer, Phys. Rev. Lett. **69**, 1065 (1992).

102. R. D. Johnson, C. S. Yannoni, H. C. Dorn, J. R. Salem, and D. S. Bethune, Science **255**, 1235 (1992).

103. Q. Zhu, O. Zhou, N. Coustel, G. B. M. Vaughan, J. P. McCauley, Jr., W. J. Romanow, J. E. Fischer, and A. B. Smith III, Science **254**, 545 (1992).

104. D. W. Murphy, M. J. Rosseinsky, R. M. Fleming, R. Tycko, A. P. Ramirez, R. C. Haddon, T. Siegrist, G. Dabbagh, J. C. Tully, and R. E. Walstedt, J. Phys. Chem. Solids **53**, 1321 (1992).

105. K. Tanigaki, I. Hirosawa, T. W. Ebbesen, J. Mizuki, Y. Shimakawa, Y. Kubo, J. S. Tsai, and S. Kuroshima, Nature **356**, 419 (1992).

106. P. W. Stephens, Nature **356**, 383 (1992).

107. A. R. Kortan, N. Kopylov, R. M. Fleming, O. Zhou, F. A. Thiel, R. C. Haddon, and K. M. Rabe, Phys. Rev. B **47**, 13070 (1993).

108. A. Oshiyama, S. Saito, N. Hamada, and Y. Miyamoto, J. Phys. Chem. Solids **53**, 1457 (1992).

109. F. N. Tebbe, R. L. Harlow, D. B. Chase, D. L. Thorn, G. C. Campbell, Jr., J. C. Calabrese, N. Herron, R. J. Young, Jr., and E. Wasserman, Science **256**, 822 (1992).

110. Y. Miyamoto, A. Oshiyama, and S. Saito, Solid State Commun. **82**, 437 (1992).

111. Y. Wang, D. Tomanek, and G. F. Bertsch, Phys. Rev. B **44**, 6562 (1991).

112. D. S. Bethune, G. Meijer, W. C. Tang, and H. J. Rosen, Chem. Phys. Lett. **174**, 219 (1990).

113. P. C. Eklund, P. Zhou, K-A. Wang, G. Dresselhaus, and M. S. Dresselhaus, J. Phys. Chem. Solids **53**, 1391 (1992).

114. A. M. Vassallo, L. S. Pang, P. A. Cole-Clark, and M. A. Wilson, J. Am. Chem. Soc. **113**, 7820 (1991).

115. B. Chase, N. Herron, and E. Holler, J. Phys. Chem. **96**, 4262 (1992).

116. K. A. Wang, Y. Wang, P. Zhou, J. M. Holden, S. L. Ren, G. T. Hager, H. F. Ni, P. C. Eklund, G. Dresselhaus, and M. S. Dresselhaus, Phys. Rev. B **45**, 1955 (1992).

117. P. Zhou, K-A. Wang,, Y. Wang, P. C. Eklund, M. S. Dresselhaus, G. Dresselhaus, and R. A. Jishi, Phys. Rev. B **46**, 2595 (1992).

118. D. S. Bethune, G. Meijer, W. C. Tang, H. J. Rosen, W. G. Golden, H. Seki, C. A. Brown, and M. S. Derries, Chem. Phys. Lett. **179**, 181 (1991).

119. G. Meijer, D. S. Bethune, W. C. Tang, H. J. Rosen, R. D. Johnson, R. J. Wilson, D. D. Chambliss, W. G. Golden, H. Seki, M. S. DeVries, C. A. Brown, J. R. Salem, H. E. Hunziker, and H. R. Wendt, in *Clusters and Cluster-Assembled Materials,* edited by R. S. Averback, J. Bernholc, and D. L. Nelson (Mater. Res. Soc. Symp. Proc. **206**, Pittsburgh, PA, 1991), p. 619.

120. S. J. Duclos, R. C. Haddon, S. H. Glarum, A. F. Hebard, and K. B. Lyons, Science **254**, 1625 (1991).

121. R. E. Stanton and M. D. Newton, J. Phys. Chem. **92**, 2141 (1988).

122. F. Negri, G. Orlandi, and F. Zerbetto, Chem. Phys. Lett. **144**, 31 (1988).

123. R. L. Disch and J. M. Schulmann, Chem. Phys. Lett. **125**, 465 (1986).

124. M. Häser, J. Almlöf, and G. E. Scuseria, Chem. Phys. Lett. **181**, 497 (1991).

125. G. B. Adams, J. B. Page, O. F. Sankey, K. Sinha, J. Menendez, and D. R. Huffman, Phys. Rev. B **44**, 4052 (1991).

126. B. P. Feuston, W. Andreoni, M. Parrinello, and E. Clementi, Phys. Rev. B **44**, 4056 (1991).

127. Z. C. Wu, D. A. Jelski, and T. F. George, Chem. Phys. Lett. **137**, 291 (1987).

128. S. J. Cyvin, E. Brendsdal, B. N. Cyvin, and J. Brunvoll, Chem. Phys. Lett. **143**, 377 (1988).

129. D. E. Weeks and W. G. Harter, J. Chem. Phys. **90**, 4744 (1989).

130. R. A. Jishi, R. M. Mirie, and M. S. Dresselhaus, Phys. Rev. B **45**, 13685 (1992).

131. P. Zhou, A. M. Rao, K-A. Wang, J. D. Robertson, C. C. Eloi, M. S. Meier, S. L. Ren, X. X. Bi, P. C. Eklund, and M. S. Dresselhaus, Appl. Phys. Lett. **60**, 2871 (1992).

132. Z-H. Dong, P. Zhou, J. M. Holden, P. C. Eklund, M. S. Dresselhaus, and G. Dresselhaus, Phys. Rev. B **48** (in press).

133. M. K. Nissen, S. M. Wilson, and M. L. W. Thewalt, Phys. Rev. Lett. **69**, 2423 (1992).

134. C. Coulombeau, H. Jobic, P. Bernier, C. Fabre, and A. Rassat, J. Phys. Chem. **96**, 22 (1992).

135. R. A. Jishi, M. S. Dresselhaus, G. Dresselhaus, K. A. Wang, P. Zhou, A. M. Rao, and P. C. Eklund, Chem. Phys. Lett. **206**, 187 (1993).

136. D. W. Snoke, Y. S. Raptis, and K. Syassen, Phys. Rev. B **45**, 14419 (1992).

137. R. A. Jishi, R. M. Mirie, M. S. Dresselhaus, G. Dresselhaus, and P. C. Eklund, Phys. Rev. B (in press).

138. P. Zhou, K. A. Wang, P. C. Eklund, G. Dresselhaus, M. S. Dresselhaus, Phys. Rev. B (in press).

139. T. Pichler, M. Matus, J. Kürti, and H. Kuzmany, Phys. Rev. B **45**, 13841 (1992).

140. S. H. Glarum, S. J. Duclos, and R. C. Haddon, J. Am. Chem. Soc. **114**, 1996 (1992).

141. P. Zhou, K. A. Wang, A. M. Rao, P. C. Eklund, G. Dresselhaus, and M. S. Dresselhaus, Phys. Rev. B **45**, 10838 (1992).

142. M. S. Dresselhaus and G. Dresselhaus, *Light Scattering in Solids III, Topics in Applied Physics,* edited by M. Cardona and G. Güntherodt (Springer-Verlag, Berlin, 1982), Vol. 51, p. 3.

143. R. A. Jishi and M. S. Dresselhaus, Phys. Rev. B **45**, 6914 (1992).

144. W. DeSorbo and W. W. Tyler, J. Chem. Phys. **21**, 1660 (1953).
145. P. H. Keesom and N. Pearlman, Phys. Rev. **99**, 1119 (1955).
146. S. Huant, G. Chouteau, J. B. Robert, P. Bernier, C. Fabre, A. Rassat, and E. Bustarret, C.R. Acad. Sci., Paris Serie II **314**, 1309 (1992).
147. G. Kriza, J. C. Ameline, J. Jerome, A. Dworkin, H. Szwarc, C. Fabre, D. Schutz, A. Rassat, and P. Bernier, J. Phys. I, France **1**, 1361 (1991).
148. T. Nihira and T. Iwata, J. Appl. Phys. **14**, 1099 (1975).
149. D. T. Morelli and C. Uher, Phys. Rev. B **31**, 6721 (1985).
150. R. Berman, P. R. W. Hudson, and M. Martinez, J. Phys. C: Solid State **8**, L430 (1975).
151. G. Herzberg, in *Molecular Spectra and Molecular Structure* (Van Nostrand, Princeton, NJ, 1945); icosahedral symmetry is not treated explicitly.
152. S. Saito and A. Oshiyama, Phys. Rev. Lett. **66**, 2637 (1991).
153. F. Negri, G. Orlandi, and F. Zerbetto, J. Am. Chem. Soc. **114**, 2910 (1992).
154. R. Saito, G. Dresselhaus, and M. S. Dresselhaus, Phys. Rev. B **46**, 9906 (1992).
155. F. Negri, G. Orlandi, and F. Zerbetto, Chem. Phys. Lett. **196**, 303 (1992).
156. R. Saito, G. Dresselhaus, and M. S. Dresselhaus, Chem. Phys. Lett. (in press).
157. C. T. Chen, L. H. Tjeng, P. Rudolf, G. Meigs, J. F. Rowe, J. Chen, J. P. McCauley, A. B. Smith, A. R. McGhie, W. J. Romanow, and C. Plummer, Nature **352**, 603 (1991).
158. R. C. Haddon, L. E. Brus, and K. Raghavachari, Chem. Phys. Lett. **125**, 459 (1986).
159. J. L. Martins, N. Troullier, and J. H. Weaver, Chem. Phys. Lett. **180**, 457 (1991).
160. O. Zhang, J. Y. Yi, and J. Bernholc, Phys. Rev. Lett. **66**, 2633 (1991).
161. J. H. Weaver, J. L. Martins, T. Komeda, Y. Chen, T. R. Ohno, G. H. Kroll, N. Troullier, R. E. Haufler, and R. E. Smalley, Phys. Rev. Lett. **66**, 1741 (1991).
162. S. C. Erwin and M. R. Pederson, Phys. Rev. Lett. **67**, 1610 (1991).
163. A. Oshiyama and S. Saito, Solid State Commun. **82**, 41 (1992).
164. R. Tycko, G. Dabbagh, M. J. Rosseinsky, D. W. Murphy, R. M. Fleming, A. P. Ramirez, and J. C. Tully, Science **253**, 1419 (1991).
165. T. Pichler, M. Matus, J. Kürti, and H. Kuzmany, Solid State Commun. **81**, 859 (1992).
166. S. P. Sibley, S. M. Argentine, and A. H. Francis, Chem. Phys. Lett. **188**, 187 (1992).
167. Y. Wang, J. M. Holden, A. M. Rao, P. C. Eklund, U. Venkateswaran, R. L. Lidberg, D. Eastwood, G. Dresselhaus, and M. S. Dresselhaus, unpublished.
168. M. Matus, H. Kuzmany, and E. Sohmen, Phys. Rev. Lett. **68**, 2822 (1992).
169. M. S. Dresselhaus, R. Saito, and G. Dresselhaus, Mater. Sci. Eng. **B19**, 192 (1993).
170. W. Y. Ching, M-Z. Huang, Y-N. Xu, W. G. Harter, and F. T. Chan, Phys. Rev. Lett. **67**, 2045 (1991).
171. B. Wastberg and A. Rosen, Phys. Scripta **44**, 276 (1991).
172. S. Larsson, A. Volosov, and A. Rosen, Chem. Phys. Lett. **137**, 501 (1987).
173. J. B. Birks, in *Photophysics of Aromatic Molecules* (John Wiley and Sons, London, 1970). A general review of the molecular spectroscopy of aromatic molecules.
174. R. R. Hung and J. J. Grabowski, J. Phys. Chem. **95**, 6075 (1991).
175. T. W. Ebbesen, K. Tanigaki, and S. Kuroshima, Chem. Phys. Lett. **181**, 501 (1991).
176. J. W. Arbogast, A. P. Darmanyan, C. S. Foote, R. Rubin, F. N. Diederich, M. M. Alvarez, S. J. Anz, and R. L. Whetten, J. Phys. Chem. **95**, 11 (1991).
177. M. R. Wasielewski, M. P. O'Neil, K. R. Lykke, M. J. Pellin, and D. M. Gruen, J. Am. Chem. Soc. **113**, 2774 (1991).
178. L. W. Tutt and A. Kost, Nature **356**, 225 (1992).
179. S. L. Ren, K. A. Wang, P. Zhou, Y. Wang, A. M. Rao, M. S. Meier, J. Selegue, and P. C. Eklund, Appl. Phys. Lett. **61**, 124 (1992).
180. A. M. Rao, S. L. Ren, G. W. Lehman, P. Zhou, K-A. Wang, and P. C. Eklund, unpublished.
181. A. F. Hebard, R. C. Haddon, R. M. Fleming, and A. R. Kortan, Appl. Phys. Lett. **59**, 2109 (1991).
182. Y-N. Xu, M-Z. Huang, and W. Y. Ching, Phys. Rev. B **44**, 13171 (1991).
183. C. Reber, L. Yee, J. McKiernan, J. I. Zink, R. S. Williams, W. M. Tong, D. A. A. Ohlberg, R. L. Whetten, and F. Diederich, J. Phys. Chem. **95**, 2127 (1991).
184. Z. H. Kafafi, J. R. Lindle, R. G. S. Pong, F. J. Bartoli, L. J. Lingg, and J. Milliken, Chem. Phys. Lett. **188**, 492 (1991).
185. H. Hoshi, N. Nakamura, Y. Maruyama, T. Nakagawa, S. Suzuki, H. Shiromaru, and Y. Achiba, Jpn. J. Appl. Phys. **30**, L1397 (1991).
186. P. Prasad, in *Nonlinear Optical Properties of Organic Materials* (Plenum Press, New York, 1991).
187. A. F. Hebard, in *Physics and Chemistry of Finite Systems: From Clusters to Crystals,* edited by P. Jena, S. N. Khanna, and B. K. Rao (Kluwer Academic Publishers, Dordrecht, The Netherlands, 1991), Vol. C 374, p. 1213.
188. G. P. Kochanski, A. F. Hebard, R. C. Haddon, and A. T. Fiory, Science **255**, 184 (1992).
189. Y. Iye, *Physical Properties of High Temperature Superconductors III,* edited by D. M. Ginsberg (1992), Chap. 4, p. 285.
190. O. Klein, G. Grüner, S. M. Huang, J. B. Wiley, and R. B. Kaner, Phys. Rev. B **46**, 11247 (1992).
191. H. Ogata, T. Inabe, H. Hoshi, Y. Maruyama, Y. Achiba, S. Suzuki, K. Kikuchi, and I. Ikemoto, Jpn. J. Appl. Phys. **31**, L166 (1992).
192. T. T. M. Palstra, R. C. Haddon, A. F. Hebard, and J. Zaanen, Phys. Rev. Lett. **68**, 1054 (1992).
193. Z. H. Wang, A. W. P. Fung, G. Dresselhaus, M. S. Dresselhaus, K. A. Wang, P. Zhou, and P. C. Eklund, Phys. Rev. B (in press).
194. M. Nuñez Regueiro, P. Monceau, A. Rassat, P. Bernier, and A. Zahab, Nature **354**, 289 (1991).
195. T. Inabe, H. Ogata, Y. Maruyama, Y. Achiba, S. Suzuki, K. Kikuchi, and I. Ikemoto, Phys. Rev. Lett. **69**, 3797 (1992).
196. R. Ettl, I. Chao, F. Diederich, and R. L. Whetten, Nature **353**, 443 (1991).
197. C. P. Slichter, in *Principles of Magnetic Resonance,* 3rd ed. (Springer-Verlag, Berlin, 1990).
198. R. Tycko, G. Dabbagh, M. J. Rosseinsky, D. W. Murphy, A. P. Ramirez, and R. M. Fleming, Phys. Rev. Lett. **68**, 1912 (1992).
199. J. H. Weaver, Accounts Chem. Res. **25**, 143 (1992).
200. Z. Zhang, C. C. Chen, S. P. Kelty, H. Dai, and C. M. Lieber, Nature **353**, 333 (1991).
201. Z. Zhang, C. C. Chen, and C. M. Lieber, Science **254**, 1619 (1991).
202. M. B. Jost, N. Troullier, D. M. Poirier, J. L. Martins, J. H. Weaver, L. P. F. Chibante, and R. E. Smalley, Phys. Rev. B **44**, 1966 (1991).
203. N. B. Hannay, T. H. Geballe, B. T. Matthias, K. Andres, P. Schmidt, and D. MacNair, Phys. Rev. Lett. **14**, 225 (1965).
204. Y. Koike, K. Higuchi, and S. Tanuma, Solid State Commun. **27**, 623 (1978).

205. A. Chaiken, M. S. Dresselhaus, T. P. Orlando, G. Dresselhaus, P. M. Tedrow, D. A. Neumann, and W. A. Kamitakahara, Phys. Rev. B **41**, 71 (1990).
206. I. T. Belash, A. D. Bronnikov, O. V. Zharikov, and A. V. Pal'nichenko, Synth. Metals **36**, 283 (1990).
207. K. Holczer, O. Klein, G. Grüner, S-M. Hwanf, R. B. Kaner, K-J. Fu, R. L. Whetten, and F. Diederich, Science **252**, 1154 (1991).
208. O. Zhou, G. Vaughan, B. M. Gavin, Q. Zhu, J. E. Fischer, P. A. Heiney, N. Coustel, J. P. McCauley, Jr., and A. B. Smith III, Science **255**, 833 (1992).
209. G. Sparn, J. D. Thompson, S-M. Huang, R. B. Kaner, F. Diederich, R. L. Whetten, G. Grüner, and K. Holczer, Science **252**, 1829 (1991).
210. G. Sparn, J. D. Thompson, R. L. Whetten, S-M. Huang, R. B. Kaner, F. Diederich, G. Grüner, and K. Holczer, Phys. Rev. Lett. **68**, 1228 (1992).
211. J. E. Schirber, D. L. Overmyer, H. H. Wang, J. M. Wang, K. D. Carlson, A. M. Kini, M. J. Pellin, U. Welp, and W-K. Kwok, Physica C **178**, 137 (1991).
212. C. M. Varma, J. Zaanen, and K. Raghavachari, Science **254**, 989 (1991).
213. M. A. Schlüter, M. Lannoo, M. Needels, G. A. Baraff, and D. Tománek, Phys. Rev. Lett. **68**, 526 (1992).
214. K. H. Johnson, M. E. McHenry, and D. P. Clougherty, Physica C **183**, 319 (1991).
215. R. A. Jishi and M. S. Dresselhaus, Phys. Rev. B **45**, 2597 (1992).
216. C-C. Chen and C. M. Lieber, J. Am. Chem. Soc. **114**, 3141 (1992).
217. T. W. Ebbesen, J. S. Tsai, K. Tanigaki, J. Tabuchi, Y. Shimakawa, Y. Kubo, I. Hirosawa, and J. Mizuki, Nature **355**, 620 (1992).
218. A. P. Ramirez, A. R. Kortan, M. J. Rosseinsky, S. J. Duclos, A. M. Mujsce, R. C. Haddon, D. W. Murphy, A. V. Makhija, S. M. Zahurak, and K. B. Lyons, Phys. Rev. Lett. **68**, 1058 (1992).
219. A. A. Zakhidov, K. Imaeda, D. M. Petty, K. Yakushi, H. Inokuchi, K. Kikuchi, I. Ikemoto, S. Suzuki, and Y. Achiba, Phys. Lett. A **164**, 355 (1992).
220. Y. J. Uemura, A. Keren, L. P. Le, G. M. Luke, B. J. Sternlieb, W. D. Wu, J. H. Brewer, R. L. Whetten, S. M. Huand, S. Lin, R. B. Kaner, F. Diederich, S. Donovan, and G. Grüner, Nature **352**, 605 (1991).
221. K. Holczer, O. Klein, G. Grüner, J. D. Thompson, F. Diederich, and R. L. Whetten, Phys. Rev. Lett. **67**, 271 (1991).
222. S. Foner, E. J. McNiff, Jr., D. Heiman, S. M. Huang, and R. B. Kaner, Phys. Rev. B **46**, 14 936 (1992).
223. N. R. Werthamer, E. Helfand, and P. C. Hohenberg, Phys. Rev. **147**, 295 (1966).
224. H. Suematsu, Y. Murakami, T. Arai, K. Kikuchi, Y. Achiba, and I. Ikemoto, Mater. Sci. Eng. **B19**, 141 (1993).
225. M. S. Dresselhaus, G. Dresselhaus, and R. Saito, Phys. Rev. B **45**, 6234 (1992).
226. S. Iijima, Nature **354**, 56 (1991).
227. M. Endo, H. Fujiwara, and E. Fukunaga, Meeting of Japanese Carbon Society, 34–35 (1991), unpublished.
228. M. Endo, H. Fujiwara, and E. Fukunaga, Second C$_{60}$ Symposium in Japan, 101–104 (1992), unpublished.
229. P. M. Ajayan and S. Iijima, Nature **358**, 23 (1992).
230. M. S. Dresselhaus, Nature **358**, 195 (1992).
231. Z. Ya. Kosakovskaya, L. A. Chernozatonskii, and E. A. Fedorov, JETP Lett. (Pis'ma Zh. Eksp. Teor.) **56**, 26 (1992).
232. L. D. Lamb, private communication (1992).
233. R. Bacon, J. Appl. Phys. **31**, 283 (1960).
234. S. Wang and P. R. Buseck, Chem. Phys. Lett. **182**, 1 (1991).
235. M. Endo and H. W. Kroto, J. Phys. Chem. **96**, 6941 (1992).
236. R. Saito, G. Dresselhaus, and M. S. Dresselhaus, Chem. Phys. Lett. **195**, 537 (1992).
237. S. Iijima, T. Ichihashi, and Y. Ando, Nature **356**, 776 (1992).
238. R. Smalley, Mater. Sci. Eng. B **B19**, 1 (1993).
239. R. Saito, M. Fujita, G. Dresselhaus, and M. S. Dresselhaus, Appl. Phys. Lett. **60**, 2204 (1992).
240. G. Overney, W. Zhong, and D. Tománek, Z. Phys. D **27**, 93 (1993).
241. J. W. Mintmire, B. I. Dunlap, and C. T. White, Phys. Rev. Lett. **68**, 631 (1992).
242. N. Hamada, S-I. Sawada, and A. Oshiyama, Phys. Rev. Lett. **68**, 1579 (1992).
243. K. Harigaya, Phys. Rev. B **45**, 4479 (1992).
244. K. Tanaka, K. Okahara, M. Okada, and T. Yamabe, Chem. Phys. Lett. **191**, 469 (1992).
245. R. Saito, M. Fujita, G. Dresselhaus, and M. S. Dresselhaus, in *Electrical, Optical, and Magnetic Properties of Organic Solid State Materials,* edited by L. Y. Chiang, A. F. Garito, and D. J. Sandman (Mater. Res. Soc. Symp. Proc. **247**, Pittsburgh, PA, 1992), p. 333.
246. R. Saito, M. Fujita, G. Dresselhaus, and M. S. Dresselhaus, Phys. Rev. B **46**, 1804 (1992).
247. G. S. Painter and D. E. Ellis, Phys. Rev. B **1**, 4747 (1970).
248. R. Saito, G. Dresselhaus, and M. S. Dresselhaus, J. Appl. Phys. **73**, 494 (1993).
249. M. Endo, CHEMTECH **18** (Sept.), 568 (1988).
250. M. S. Dresselhaus, G. Dresselhaus, K. Sugihara, I. L. Spain, and H. A. Goldberg, in *Graphite Fibers and Filaments* (Springer-Verlag, Berlin, 1988), Vol. 5 of *Springer Series in Materials Science.*
251. J. S. Speck, J. Appl. Phys. **67**, 495 (1990).
252. E. A. Kmetko, in *Proceedings of the First and Second Conference on Carbon,* edited by S. Mrozowski and L. W. Phillips (Waverly Press, Buffalo, NY, 1956), p. 21.
253. R. D. Heidenreich, J. Appl. Crystallogr. **1**, 1 (1968).
254. D. Ugarte, Nature **359**, 707 (1992); see also H. W. Kroto, Nature **359**, 670 (1992).
255. H. Kroto, Nature **359**, 670 (1992).
256. M. N. Regueiro, P. Monceau, and J-L. Hodeau, Nature **355**, 237 (1992).
257. R. Meilunas, R. P. H. Chang, S. Z. Lu, and M. M. Kappes, Appl. Phys. Lett. **59**, 3461 (1991).
258. Y. Wang, Nature **356**, 585 (1992).
259. R. Taylor, A. G. Avent, T. J. Dennis, J. P. Hare, H. W. Kroto, D. R. M. Walton, J. H. Holloway, E. G. Hope, and G. J. Langley, Nature **355**, 27 (1992).